Spring 4-25-2014

Electron Matter Interferometry and the Electron Double-Slit Experiment

Roger Bach
University of Nebraska-Lincoln, roger.bach@gmail.com

ELECTRON MATTER INTERFEROMETRY AND THE ELECTRON DOUBLE-SLIT EXPERIMENT

Roger Anthony Bach

A DISSERTATION

Presented to the Faculty of

The Graduate College at the University of Nebraska

In Partial Fulfillment of Requirements

For the Degree of Doctor of Philosophy

Major: Physics and Astronomy

Under the Supervision of Professor Herman Batelaan

Lincoln, Nebraska

May, 2014

ELECTRON MATTER INTERFEROMETRY AND THE ELECTRON DOUBLE-SLIT EXPERIMENT

Roger Anthony Bach, Ph.D.

University of Nebraska, 2014

Advisor: Herman Batelaan

Quantum mechanics has fundamentally changed the way scientists think about the world. Quantum mechanical theory has found it's way into our everyday lives through advances in technology. In this dissertation a fundamental quantum mechanical demonstration and the technological development of a new quantum mechanical device are presented.

Double-slit diffraction is a corner stone of quantum mechanics. It illustrates key features of quantum mechanics: interference and the particle-wave duality of matter. Here we demonstrate the full realization of Richard Feynman's famous thought experiment. By placing a movable mask in front of a double-slit to control the transmission through the individuals slits. Probability distributions for single- and double-slit arrangements were observed. Additionally, by recording single electron detection events diffracting through a double-slit, a diffraction pattern was built up from individual events.

Additionally, a demonstration of a three grating Talbot-Lau interferometer for electrons is presented. As a proof of principle the interferometer is used to measure magnetic fields. The possibility to extend this work to build a scaled-up electron interferometer for sensitive magnetic field sensing is discussed.

A theoretical model is presented to simulate the two experiments. This model is developed from Richard Feynman's path integral formalism, where a wave function is propagated through the elements of the system. The theoretical simulations reproduce the experimental data well, except for a large discrepancy of a factor of 5.5

between the experimental and theoretical sensitivity of the Talbot-Lau interferometer. The origin of the discrepancy is currently unknown. These experiments were built off of previous work done here at the University of Nebraska-Lincoln, and improvements to the preexisting system are discussed.

While these experiments likely did not demonstrate anything contrary to conventional quantum mechanics, it is important to continually probe these types of experiments to test the fundamental principles of quantum mechanics and explore it's technical applications.

Preface

The electron double-slit diffraction experiment is described in Chapter 4 and has been published in *New Journal of Physics*.[1]

The demonstration of a Talbot-Lau interferometer for electrons is described in Chapter 5 and has been published in *Applied Physics Letters*.[2]

A wide-angle electron grating biprism beam-splitter is mentioned in Chapter 2 and has been published in *Journal of Physics B: Atomic, Molecular & Optical Physics*.[3]

Additional work not mentioned in this dissertation include: work on a transverse quantum Stern-Gerlach magnets for electrons published in *New Journal of Physics*;[4] and a low-power optical electron switch published in *Journal of Physics D: Applied Physics*.[5]

We appreciate the support of the National Science Foundation and the Department of Education.

Table of Contents

List of Figures

List of Tables

Chapter 1

Introduction

1.1 Talbot-Lau Interferometer

Interferometry is a class of techniques in which waves, electromagnetic or matter, are superimposed in order to extract information about the waves.[6] Interferometry is an important investigative techniques in the fields of astronomy, fiber optics, engineering metrology, optical metrology, oceanography, seismology, spectroscopy, quantum mechanics, nuclear physics, particle physics, plasma physics, remote sensing, biomolecular interactions, surface profiling, microfuidics and velocimetry.[7]

Interferometers are widely used in science to measure small changes. The ultimate sensitivity of a interferometer is determined by the wavelength of the wave. The wavelength of visible light is less than 1 μm, while the wavelengths of electrons, atoms, and molecules can easily reach below 50 pm. This motivates scientists to develop interferometers utilizing these short wavelengths.

These interferometers can be utilized to measure different phenomena. For example, light interferometers are currently being used to search for gravitational waves with unprecedented sensitivity,[8] atom interferometers are currently testing general relativity,[9,10]and in this dissertation, electrons are used to sense magnetic

fields.

One motivation for building a sensitive magnetic field detector is the development of a magnetic anomaly detector (MAD). A MAD is an instrument used to detect small variations in the Earth's magnetic field.[11] This device can be used to search for minerals by detecting their disturbance of the normal magnetic field, most notable diamond bearing kimberlite pipes can be detected by airborn magnetic serveys.[12] Another use of MAD's is detecting submarines by military forces. A mass of ferromagnetic material (Iron) will create a detectable disturbance in the Earth's magnetic field. MAD detectors were employed to detect submarines during World War II[13] utilizing fluxgate magnetometers.[14] MAD detectors can also be used to detect mines, unexploded ordinance, buried drums, or any other iron-like material.

In their famous 1927 experiment, Davisson and Germer showed that electrons can behave like waves by observing diffraction from the periodic structure of a material crystal.[15] Soon after, Estermann and Stern reported diffraction of neutral helium atoms by lithium fluoride crystals in 1930.[16] An electron interferometer using crystals was then developed.[17,18] Solid crystals used in these interferometers absorb low energy electron. Low energy electrons are necessary to improve the sensitivity of an interferometer (see Equation 5.2). This is because the electrons stay in the magnetic field longer at lower velocity. Another alternative developed soon after, and was demonstrated by Möllenstedt and Düker in 1954, was the electron biprism interferometer.[19–21] An electron biprism is equivalent to a Fresnel biprism for light (see Section 2.5).[22] Electron biprism interferometer have been used for many tasks, such as: testing the Aharonov-Bohm effect,[23] viewing domain walls in type II superconductors,[24] and observing atomic steps in thin films.[25] The largest separation previously achieved between interferometer arms was about 120 μm.[26,27] A large separation is advantageous because the sensitivity of the interferometer scales with

arm separation (see Equation 5.4). The limitations of the current biprism interferometers may be due to dephasing or decoherence processes. Dephasing and decoherence are difficult to eliminate because the lightweight, charged electron interacts strongly with its environment.

To develop a useful large area electron interferometer nano-fabricated grating were adopted. These gratings had been successfully developed for atom interferometry and had been used for Na atom interferometry,[28] He_2 molecule diffraction,[29] and bucky ball diffraction.[30] The electron-grating interactions were determined to be minimal at moderate energies but still needed to be accounted for in simulations.[31–33] Gronniger et al. successfully demonstrated a three grating electron interferometer in 2006.[34]

The Talbot-Lau interferometer is an extension of the previous work done with nano-fabricated gratings and slits here at the University of Nebraska-Lincoln[3,33,34] and was motivated by a collaborative project with the company Honeywell. The original project was to characterizing the electromagnetic response of a three grating electron Mach-Zehnder interferometer.[34] Those results are not published and are not included in this dissertations. The last deliverable of the project, was to test the feasibility of a Moiré deflectometer. A Moiré deflectometer is a classical device analogous to a Talbot-Lau interferometer. Chapter 5 covers the results of the last deliverable of the collaborative project. An electron Talbot-Lau interferometer was realized and demonstrated to have a sensitivity of of 4.7 $\mathrm{nT\,Hz^{-1/2}}$,

1.2 Double-Slit Diffraction

In the fall of 2008 Damian Pope, the outreach director of the Perimeter Institute for Theoretical Physics in Waterloo, Ontario, contacted us about filming a short education movie intended for high school students. The movie would feature the

electron double-slit experiment. Pope was wanting to cover wave-particle duality to highlight the mystery of quantum mechanics.

Damian Pope had found a movie of the build-up of an electron diffraction pattern from a grating that was posted online. I made the video during the summer of 2006 completing a Research Experience for Undergraduates (REU) with Professor Batelaan. We approached Professor Sy-Hwang Liou to helped us with the manufacturing of a double-slit and we quickly put together an experiment to film.

The Perimeter Institute's film staff came and filmed for two days. The experiment is emphasized heavily and the script of the movie follows Feynman's thought experiment.[35] The movie is currently being used in high schools across Canada and is available on the Perimeter Institute's website.*

After some research, it was determined that no one had actually done an experiment showing the build-up from a double-slit. The famous build-up pattern from Akira Tonomura,[36] shown in some introductory classes and can be found in books[37] and online, is actually from a biprism wire. We decided to improve on the results and make a diffraction build-up pattern that would replace the one from a biprism. Several years later the results were published[1] in *New Journal of Physics* following Feynman's famous thought experiment.[35] Chapter 4 covers the results of the electron double-slit diffraction.

The double-slit diffraction is a corner stone of quantum mechanics. Even though most physicists "understand" how it works, quantum mechanics doesn't give a mechanistic explanation of what happens to the electron between the source, the double-slit, and the detector. Additionally the only experiments showing double-slit diffraction build-up are done with biprims, where electric fields are used to bring the separated beams back together. These facts can make understanding double-slit diffraction, especially for high-school or undergraduate audiences, problematic. This

*The Challenge of Quantum Reality; `https://www.perimeterinstitute.ca/store/perimeter-explorations/challenge-quantum-reality`

dissertation addresses the latter issue by demonstrating the double-slit diffraction experiment in it's cleanest form to date.

1.3 Summary of Chapters

Chapter 2 is a brief description of electron matter propagation. It covers Fraunhofer far field diffraction, an introduction to Feynman's path integral formalism, and some electron-slit interactions. This chapter covers in detail the theory and implementation of the quantum mechanical simulations used in Chapters 4 and 5. The first part of Chapter 3 gives a detailed description of the experimental setup used in the experiments discussed in this dissertation. The latter part of Chapter 3 covers the image analysis technique. Chapter 4 covers the double-slit electron diffraction experiment. Parts of this chapter were published in *New Journal of Physics*.[1] Experimental data and theory are compared. Chapter 5 contains the experimental data and theoretical simulations for the Talbot-Lau interferometer experiment. Parts of this chapter were published in *Applied Physics Letters*.[2] The experiment is compared to both a classical and quantum mechanical simulation. Some conclusions and a short discussion of future directions are given in Chapter 6.

Appendix A is the path integral calculation of the propagator for the harmonic oscillator. Appendix B gives a short description of the Labview image acquisition program. Appendix C is a description of the image analysis code and path integral simulation codes. Appendix D is multiple computer aided design drawings for different components manufactured in the machine shop at the University of Nebraska-Lincoln, Department of Physics. Appendix E is several online articles covering the release of the electron double-slit paper.[1]

Chapter 2

Electron Matter Propagation

2.1 Introduction

The propagation of an electron matter wave can behave completely differently than it's classical counterpart. The simplest example of this is when an electron propagates through a double-slit or grating. Classical mechanics predicts shadow like patterns in the far field while what is observe is diffraction patterns (see Chapter 4 for experimental diffraction patterns). To correctly propagate an electron matter wave, quantum mechanics must be used. To incorporate a full 4-dimensional* standard quantum mechanical propagation would be time consuming and non-practical. A 2-dimensional Feynman path integral calculation[38] and a matter wave analogy to Fraunhofer far field diffraction[22] were used to streamline simulations.

The first section of this chapter will give a brief overview of Fraunhofer far field diffraction for single-slit, double-slit, and gratings. The rest of this chapter will cover an introduction of Feynman's path integral formalism and it's application to different components used in experiments, i.e., slits, double-slits, gratings, etc.

*3 spatial dimensions + time

2.2 Fraunhofer Far Field Diffraction

One similarity between the propagation of light and matter is that both can be described by the Helmholtz equation ($(\nabla^2 + k^2)\Psi = 0$), but with different dispersion relations.[39] In free space the dispersion relation for matter waves is $k = \sqrt{\frac{2m\omega}{\hbar}}$, while for light waves it is $k = \frac{\omega}{c}$ (with $E = \hbar\omega$ for both). This fact can be used to form analogies between the two different propagations. Single-, double-, and multi-slit diffraction are well know in optics and the equations developed for them can be used in matter optics.

The simplest structure that exhibits diffraction is the single-slit. The far-field diffraction pattern's intensity can be represented by[40]

$$I = I_0 \left[\frac{\sin(\alpha)}{\alpha}\right]^2, \tag{2.1}$$

where $\alpha = \frac{\pi a}{\lambda}\sin(\theta)$ and I_0 is the intensity at the center. The width of the slit is a, λ is the wavelength, and θ represents the angle from the normal of the slit (see Figure 2.1 top). This distribution has a maximum at the center with minimums when $\alpha = \pi n$ ($n \neq 0$, $n \in \mathbb{Z}$). This is in contrast to classical mechanics, which only predicts a central maximum with a decreasing intensity as the magnitude of θ increases.

Diffraction can also be seen from the double-slit, see Figure 2.1 middle. In addition to each individual slit exhibiting single-slit diffraction, there is mutual interference between individual slits. The far-field diffraction pattern's distribution can be represented by[40]

$$I = 4I_0 \left[\frac{\sin(\alpha)}{\alpha}\right]^2 \cos^2\beta, \tag{2.2}$$

where $\beta = \frac{\pi d}{\lambda}\sin(\theta)$. The center-to-center separation between individual slits is

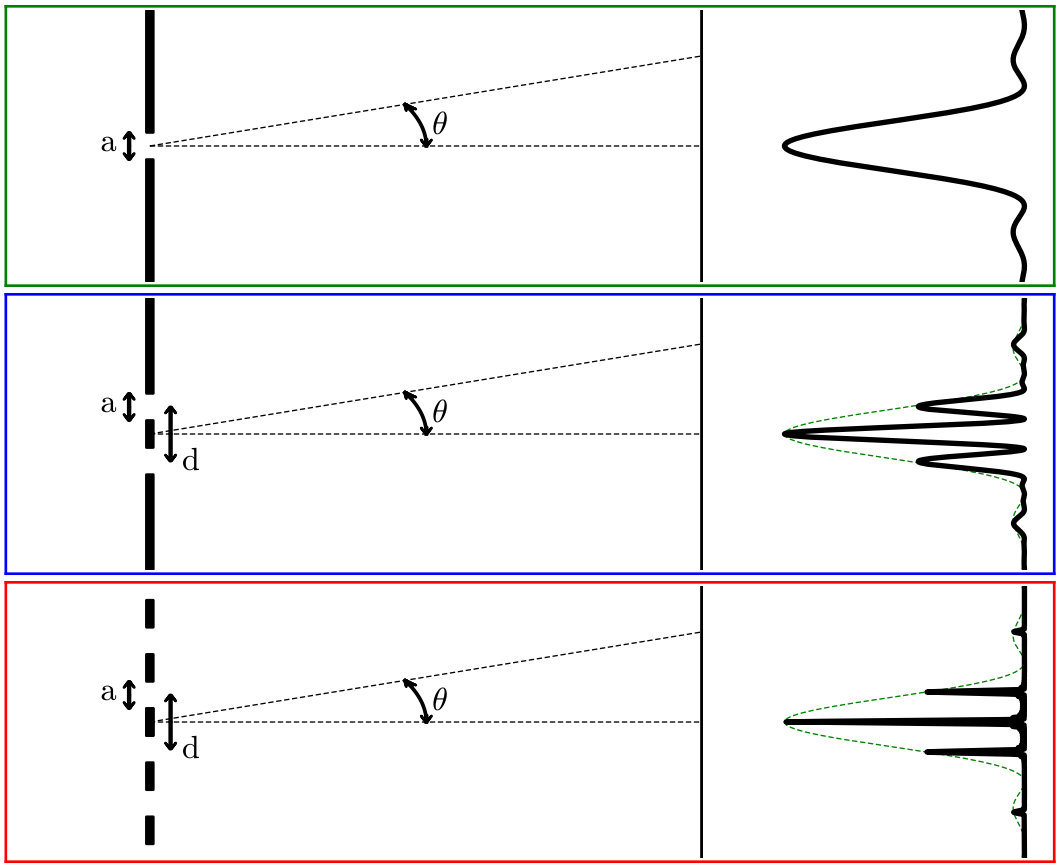

Figure 2.1. Illustration of single-, double-, and multi-slit diffraction (top to bottom). The width of the individual slits are a. The length d represents the center-to-center separation for the double-slit and the periodicity for the multi-slit. The corresponding intensity distribution is represented on the right. The single slit envelope is shown by a dashed (green) line for the double- and multi-slit. The same values for a and d were used for each distribution, with $d = 2a$.

d. This distribution is the single-slit distribution multiplied by a cosine function that depends on d. This is why the outline of the maximums is referred to as the single-slit envelope, illustrated by the dashed (green) line in Figure 2.1. There are additional minimums when $\beta = \pi(n - \frac{1}{2})$, $n \in \mathbb{Z}$.

A multi-slit or grating shows properties of diffraction as well. The far field diffraction pattern's distribution is represented by[40]

$$I = I_0 \left[\frac{\sin\alpha}{\alpha}\right]^2 \left[\frac{\sin(N\beta)}{\sin\beta}\right]^2, \tag{2.3}$$

where N is the number of slits. This distribution is shown in Figure 2.1 bottom and also has the single-slit envelope, shown by the dashed (green) line. The double-slit diffraction is a subset of the multi-slit diffraction, with $N = 2$,

$$\left[\frac{\sin(2\beta)}{\sin\beta}\right]^2 = \left[\frac{2\sin(\beta)\cos(\beta)}{\sin\beta}\right]^2 = 4\cos^2\beta. \tag{2.4}$$

This distribution has maximums near $\beta = m\pi$, $m \in \mathbb{Z}$, which leads to

$$m\lambda = d\sin(\theta). \tag{2.5}$$

Equation 2.5 is sometimes called the diffraction grating equation[41] and m is identified as the order of the diffraction.

Equations 2.1, 2.2, and 2.3 represent an ideal situation; a single frequency source producing plane waves. Real physical sources have finite frequency bandwidths and finite spatial distributions. The amplitude and phase at any point in the field will undergo fluctuations compared to constant amplitude and linear phase. This is due to the specifics of the source. The characteristic time in which the fluctuations are minimal is the coherence time.[22] The coherence length is the characteristic distance the correlations between the phase, still exist.

The source is not the only thing that can affect the coherence length. Interactions of the wave with the environment can effect the coherence length.[42–44] This is not always bad, it can be used as a tool to probe an interaction, e.g., the interaction between electrons and a double-slit (see Chapter 4). The transverse[†] coherence length can be measured by diffracting the wave through a single, double, or multi-slit. If the coherence length is much less than the slit width a, the diffraction will lose visibility and revert to a classical beam.[33] If a multi-slit is used, the pattern will be different depending on how many slit are illuminated coherently. Figure 2.1

[†]Perpendicular to the direction of propagation

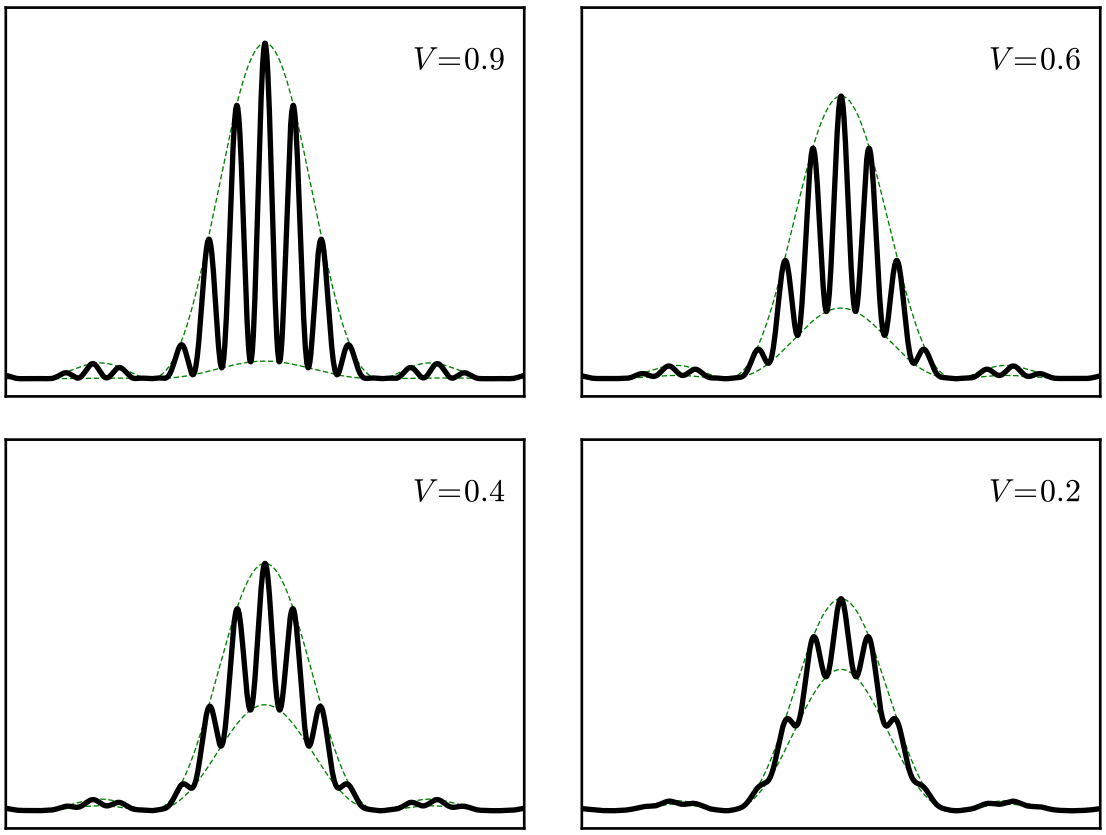

Figure 2.2. Illustration of partial coherence for the double-slit. The solid (black) line represents the far-field diffraction pattern's distribution for different visibility parameters. The dashed (green) line illustrated the maximum and minimum envelope. The visibility parameter used in the distribution is shown in the upper right. The same values for a and d were used for each distribution, with $d = 4a$.

illustrates this with 2 slits (center) and 10 slits (bottom) being illuminated fully coherently.

A double-slit can be used to measure the coherence between its two slits. Assuming the transverse coherence length to be larger than the width of the single slits, the far-field diffraction pattern's distribution can be represented by[22]

$$I = 2I_0 \left[\frac{\sin(\alpha)}{\alpha}\right]^2 [1 + V\cos(2\beta)]\,, \tag{2.6}$$

where V is a measure of the coherence between the slits. If V is 1 then the two slits are fully coherent with each other and Equation 2.6 will reduce to Equation 2.2 us-

ing a double angle formula. If V is 0 then the slits are fully incoherent and Equation 2.6 will reduce to twice Equation 2.1. V is also the visibility parameter or contrast, $V = (I_{\max} - I_{\min})/(I_{\max} + I_{\min})$ of the diffraction pattern. Figure 2.2 illustrates Equation 2.6 with different visibility parameters. The visibility parameter can be used to discern information about the initial wave or the interaction with its environment.

Because light waves interact differently with surfaces compared to with electron waves, the analogy between them is less obvious than the Helmholtz equation suggests. An example is the image charge potential when an electron is beside a grounded surface. To treat interaction between matter waves and surfaces or interfaces a Feynman's path integral[38] formalism was adopted to propagate the waves. This is covered in the next section.

2.3 Feynman's Path Integral Formalism

To overcome the shortcomings of the simple analogy between light and matter waves, a more in-depth model was developed. The model is based off of Feynman's path integral formulation.[38] Feynman's method utilizes classical trajectories to calculate the probability of finding a particle at a location. The contribution from a single path is an exponential whose phase is the classical action, in units of $\hbar$. This leads to a kernel or propagator which describes how the initial wave function moves through the system.

2.3.1 Propagation

The wave function $\Psi(\vec{x}, t)$ is propagated in time by

$$\Psi(\vec{x}, t) = \int d\vec{x}' \; K(\vec{x}, t; \vec{x}', t') \, \Psi(\vec{x}', t'), \tag{2.7}$$

where $t' < t$ and K is the kernel given by

$$K(\vec{x}, t; \vec{x}', t') = A(t; t') \exp\left[\frac{i}{\hbar} S(\vec{x}, t; \vec{x}', t')\right], \tag{2.8}$$

A is a normalization factor that only depends on time and S is the classical action of the path. The paths used are the classical paths that satisfy the principle of stationary action[45] ($\delta S = 0$). This propagator holds when the typical vales of the action are large compared to $\hbar$.[46]

2.3.2 Free Space

The simplest example is free space. The Lagrangian for the free particle in two dimensions is just the kinetic energy $L = \frac{m}{2}\dot{x}^2 + \frac{m}{2}\dot{y}^2$, where m is the mass of the particle. The classical path can be found by solving the Euler-Lagrange equations:

$$\frac{d}{dt}\frac{\partial L}{\partial \dot{x}} - \frac{\partial L}{\partial x} = 0, \tag{2.9}$$

and similarly for y. In free space the x and y coordinates are not coupled, so they can be solved separately. Solving Equation 2.9 results in $\dot{x} = C$, where C is a constant. The constant can be solved for by integration with an initial point of $\vec{x}' = (x_a, x_b)$, $t' = t_a$ and finial point of $\vec{x} = (x_b, y_b)$, $t = t_b$. The path and the velocity are:

$$\begin{aligned} x(t) &= x_a + \frac{(t - t_a)(x_b - x_a)}{t_b - t_a}, \\ \dot{x}(t) &= \frac{x_b - x_a}{t_b - t_a}. \end{aligned} \tag{2.10}$$

The solution for y is identically solved for. The action can be calculated along this path,

$$\begin{aligned} S(\vec{x}_b, t_b; \vec{x}_a, t_a) &= \int_{t_a}^{t_b} dt\ L(\vec{x}_b, t_b; \vec{x}_a, t_a) \\ &= \int_{t_a}^{t_b} dt\ \frac{m}{2}\left[\left(\frac{x_b - x_a}{t_b - t_a}\right)^2 + \left(\frac{y_b - y_a}{t_b - t_a}\right)^2\right] \\ &= \frac{m}{2}\left[\frac{(x_b - x_a)^2}{t_b - t_a} + \frac{(y_b - y_a)^2}{t_b - t_a}\right]. \end{aligned} \tag{2.11}$$

This can be put directly into Equation 2.8 to give the kernel,

$$K(\vec{x}_b, t_b; \vec{x}_a, t_a) = A(t; t') \exp\left\{\frac{i}{\hbar}\frac{m}{2}\left[\frac{(x_b - x_a)^2}{t_b - t_a} + \frac{(y_b - y_a)^2}{t_b - t_a}\right]\right\}. \tag{2.12}$$

The normalization factor can found by realizing that $A(t_b, t_a) = K(0, t_b, 0, t_a)$ and that for any time t_c between t_a and t_b,

$$K(0, t_b; 0, t_a) = \int_{-\infty}^{\infty} dx_c \int_{-\infty}^{\infty} dy_c\ K(0, t_b; \vec{x}_c, t_c)\, K(\vec{x}_c, t_c; 0, t_a). \tag{2.13}$$

Substituting Equation 2.12 into Equation 2.13 results in,

$$\begin{aligned} A(t_b; t_a) = A(t_b; t_c)\, A(t_c; t_a) \int_{-\infty}^{\infty} dx_c \int_{-\infty}^{\infty} dy_c \exp\left\{\frac{i}{\hbar}\frac{m}{2}\left[\frac{x_c^2}{t_b - t_c} + \frac{y_c^2}{t_b - t_c}\right]\right\} \\ \exp\left\{\frac{i}{\hbar}\frac{m}{2}\left[\frac{x_c^2}{t_c - t_a} + \frac{y_c^2}{t_c - t_a}\right]\right\} \\ = A(t_b; t_c)\, A(t_c; t_a) \times \\ \int_{-\infty}^{\infty} dx_c \int_{-\infty}^{\infty} dy_c \exp\left\{\frac{i}{\hbar}\frac{m}{2}(x_c^2 + y_c^2)\left(\frac{1}{t_b - t_c} + \frac{1}{t_c - t_a}\right)\right\} \\ = A(t_b; t_c)\, A(t_c; t_a) \frac{2\pi i\hbar}{m}\left(\frac{1}{t_b - t_c} + \frac{1}{t_c - t_a}\right)^{-1}. \end{aligned} \tag{2.14}$$

The previous equation can be rewritten as,

$$[(t_b - t_a)\, A(t_b; t_a)] = \frac{2\pi i\hbar}{m} \left[(t_b - t_c)\, A(t_b; t_c)\right] \left[(t_c - t_a)\, A(t_c; t_a)\right]. \tag{2.15}$$

One solution is

$$A(u + u_0; u_0) = \frac{m}{2\pi i\hbar u}, \tag{2.16}$$

This allows us to fully write down the kernel,

$$K(\vec{x}_b, t_b; \vec{x}_a, t_a) = \frac{m}{2\pi i\hbar(t_b - t_a)} \exp\left\{\frac{i}{\hbar}\frac{m}{2}\left[\frac{(x_b - x_a)^2}{t_b - t_a} + \frac{(y_b - y_a)^2}{t_b - t_a}\right]\right\}. \tag{2.17}$$

This kernel is only dependent on the time difference $T = t_b - t_a$ and not on the initial time t_a. This equation can be easily modified to include three-dimensions,

$$K(\vec{x}_b, t_b; \vec{x}_a, t_a) = \left[\frac{m}{2\pi i\hbar(t_b - t_a)}\right]^{3/2} \exp\left\{\frac{i}{\hbar}\frac{m}{2}\left[\frac{(x_b - x_a)^2}{t_b - t_a} + \frac{(y_b - y_a)^2}{t_b - t_a} + \frac{(z_b - z_a)^2}{t_b - t_a}\right]\right\}. \tag{2.18}$$

The extra prefactor is from the extra integration needed to be performed in the step at Equation 2.14. The propagator found from the Schrodinger equation ends up being identical to Equation 2.18.[47]

2.3.3 Harmonic Oscillator

The next step, after free space in typical quantum mechanical classes, is to cover the harmonic oscillator. In some books the propagator for the harmonic oscillator is not even explicitly calculated.[47,48] The path integral formalism end up being a much simpler method for calculating the propagator. The potential for with a one dimensional harmonic oscillator is $V = \frac{m\omega^2}{2}x^2$. This gives a Lagrangian of $L =$

$\frac{m}{2}\dot{x}^2 - \frac{m\omega^2}{2}\dot{x}^2$, where ω is the classical frequency of the oscillator. The calculations become quite lengthy and are put in Appendix A. The end result for the kernel is[47]

$$K(x_b, t_b; x_a, t_a) = \left(\frac{m\omega}{2\pi i\hbar \sin[\omega(t_b - t_a)]}\right)^{1/2} \times \exp\left\{\frac{im\omega}{\hbar}\left[\frac{(x_a^2 + x_b^2)\cos[\omega(t_b - t_a)] - 2x_a x_b}{2\sin[\omega(t_b - t_a)]}\right]\right\}. \quad (2.19)$$

The procedure to fine the kernel was identical to the one followed finding the free space kernel.

2.3.4 External Magnetic Field

A more complicated example is for a particle in a constant external magnetic field B, in the z direction. The Lagrangian is, $L = \frac{m}{2}(\dot{x}^2 + \dot{y}^2 + \dot{z}^2) + \frac{qB}{2}(x\dot{y} - y\dot{x})$, where q is charge of the particle. Following the same method outlined for the free particle the kernel can be found,

$$K(\vec{x}_b, t_b; \vec{x}_a, t_a) = \left(\frac{m}{2\pi i\hbar T}\right)^{3/2}\left(\frac{\omega T/2}{\sin(\omega T/2)}\right) \exp\left\{\frac{i}{\hbar}\frac{m}{2}\left[\frac{(z_b - z_a)^2}{T} + \left(\frac{\omega/2}{\tan(\omega T/2)}\right)\left[(x_b - x_a)^2 + (y_b - y_a)^2\right] + \omega\left(x_a y_b - x_b y_a\right)\right]\right\}, \quad (2.20)$$

where $\omega = \frac{qB}{m}$. Calculation of this kernel was begun but was instead found in *Quantum Mechanics and Path Integrals*, problem 3.10.[49] This kernel was never used because of the coupling between x and y. Using this kernel would require the addition of an extra dimension to our simulations. This would increase the computational time.

2.3.5 Free Space Simplifications

Propagating a wave function in four-space can prove computationally intensive for all but the most simplest initial wave-function. To remedy this it is assumed that the wave function can be separated, i.e., the wave function can be written as $\Psi(\vec{x},t) = \psi_x(x,t)\,\psi_y(y,t)\,\psi_z(z,t)$. Using this, Equation 2.7 can be simplified if the kernel can also be separated. Equation 2.18 can be separated in all dimensions while Equation 2.20 can only be separated in the z-dimension. The separated free space kernel in 1-dimension is

$$K_u(u_b,t_b;u_a,t_a) = \left(\frac{m}{2\pi i\hbar T}\right)^{1/2} \exp\left\{\frac{i}{\hbar}\frac{m}{2}\left[\frac{(u_b-u_a)^2}{T}\right]\right\}, \tag{2.21}$$

where u can represent x, y, or z and $T = t_b - t_a$. Equation 2.7 becomes,

$$\Psi(\vec{x},t) = \int dx'\; K_x(x,t;x',t')\,\psi_x(x',t') \int dy'\; K_y(y,t;y',t')\,\psi_y(y',t') \int dz'\; K_z(z,t;z',t')\,\psi_z(z',t'). \tag{2.22}$$

If the wave function is also only calculated along a line satisfying $y = 0$ and $z = vt$, Equation 2.22 can be simplified further while using Equation 2.21,

$$\begin{aligned}\Psi(x,y=0,z=vt,t) = &\left(\frac{m}{2\pi i\hbar T}\right)^{1/2} \int dx' \exp\left\{\frac{i}{\hbar}\frac{m}{2}\left[\frac{(x-x')^2}{T}\right]\right\}\psi_x(x',t') \\ &\left(\frac{m}{2\pi i\hbar T}\right)^{1/2} \int dy' \exp\left\{\frac{i}{\hbar}\frac{m}{2}\left[\frac{(y')^2}{T}\right]\right\}\psi_y(y',t') \\ &\left(\frac{m}{2\pi i\hbar T}\right)^{1/2} \int dz' \exp\left\{\frac{i}{\hbar}\frac{m}{2}\left[\frac{(vt-z')^2}{T}\right]\right\}\psi_z(z',t').\end{aligned} \tag{2.23}$$

Next it is assumed that the expectation value of y and z are zero and vt respectively. This is to say the particle has a velocity of v along the z-axis with while

no velocity along the y-axis. The probability distribution is the square of the wave function. The square of the 2nd and 3rd integrals will only produce a scaling factor that will change with time. If the initial probability distribution in the y and z are assumed to be a Gaussian and there is no interactions in that dimension, the probability distribution will stay a Gaussian shape in that dimension. Thus, at $y = 0$ and $z = vt$ the probability distribution will be the largest.

The probability distribution will then be proportional to the square of $\psi_x(x,t)$. At $t = z/v$, this can be calculated by

$$\psi_x(x, z/v) = \left[\frac{mv}{2\pi i\hbar(z-z')}\right]^{1/2} \int dx' \exp\left\{\frac{i}{\hbar}\frac{mv}{2}\left[\frac{(x-x')^2}{z-z'}\right]\right\} \psi_x(x', z'/v), \quad (2.24)$$

where z' is the center position of the initial wave function. Using the Taylor expansion

$$\begin{aligned}\left[(x-x')^2 + (z-z')^2\right]^{1/2} &= (z-z')\left[1 + \frac{1}{2}\left(\frac{x-x'}{z-z'}\right)^2 + O\left\{\left(\frac{x-x'}{y-y'}\right)^4\right\}\right] \\ &= (z-z') + \frac{1}{2}\frac{(x-x')^2}{z-z'}, \end{aligned} \quad (2.25)$$

The last equality holds under the assumption that $\left(\frac{x-x'}{z-z'}\right)^2 << 1$, Equation 2.24 can be rewritten as

$$\begin{aligned}\psi_x(x, z/v) = &\left[\frac{mv}{2\pi i\hbar(z-z')}\right]^{1/2} \exp\left\{\frac{i}{\hbar}\frac{mv}{2}\left[-(z-z')\right]\right\} \times \\ &\int dx' \exp\left\{\frac{i}{\hbar}mv\left[(x-x')^2 + (z-z')^2\right]^{1/2}\right\} \psi_x(x', z'/v). \end{aligned} \quad (2.26)$$

The first exponential does not depend on x' and was moved outside the integral. It is also a global phase factor that does not come into play when calculating the probability distribution, and is left out of further calculations for simplifications.

Using the fact that the de Brolie wavelength is $\lambda_{dB} = \frac{h}{mv}$ and the reduced Planck constant is $\hbar = \frac{h}{2\pi}$, Equation 2.26 can be written as

$$\psi_x(x, z/v) = \left[\frac{1}{i\lambda_{dB}(z - z')}\right]^{1/2} \times \int dx' \exp\left\{i\frac{2\pi}{\lambda_{dB}}\left[(x - x')^2 + (z - z')^2\right]^{1/2}\right\} \psi_x(x', z'/v). \quad (2.27)$$

This kernel has been used to model multiple different experiments[3,33,34,50,51] and was used to model the experiments described in Chapter 4 and Chapter 5, This version of Equation 2.21 was used because of it's simplicity and similarities to optical wave propagation ($\phi = \frac{2\pi L}{\lambda}$).[22]

The prefactor in Equation 2.27 is independent of x and is thus a scaling factor. Since it does not effect the shape of the probability distribution, it is left out of further calculations. Also, to prevent confusion between Equation 2.21 and this equation an alternative notation was adopted. The wave function $\Psi(x)$ was propagated from one "plane" to the next (in z). This was done by

$$\Psi_f(x) = \int dx' K_{i\to f}(x, x')\Psi_i(x'). \quad (2.28)$$

The kernel in Equation 2.28 is given by

$$K_{i\to f}(x, x') = \exp\left\{i\frac{2\pi}{\lambda_{dB}}\left[(x - x')^2 + (z - z')^2\right]^{1/2}\right\}, \quad (2.29)$$

where z' and z refers to the positions of the initial and finial planes respectively. This notation will be used throughout the rest of the dissertation.

2.4 Matter Wave Interactions

One of the reason for using Feynman's path integral formalism, is it enforces the idea of accumulating a phase along a path. This can be seen evidently in Equation 2.29. The phase is $\phi = 2\pi\frac{L}{\lambda}$, where L is the length the particle traveled from the initial point to the final. Another benefit of using path integrals, is the way physical structures can be dealt with. For example, if a wall exist where the path of the electrons are, then the electrons can not pass through and that path does not contribute to the finial probability distribution.

The following sections will utilize these facts to propagate a particle through different components used in the experiments discussed in Chapter 4 and Chapter 5. One important assumptions is made during the propagation. This is that the interactions occur at or near the components and the particle propagates in free space using Equation 2.28. Even under this assumption, experimental results can be accurately simulated.

2.4.1 Single-, Double-, and Mult-Slits

The simplest structure is a single-slit. This can be used a collimation slit or a mask. First the slit is idealized as a infinity thin sheet. The wave function is fists propagated up to the slit plane and then the wave function is modified by

$$\Psi_{out}(x) = A(x)\exp\left[i\phi(x)\right]\Phi_{in}(x), \tag{2.30}$$

where $A(x)$ describes the modification of the wave function by limiting the paths and $\phi(x)$ describes the phase accumulated by the path as it passes through the slit.

The function $A(x)$ is just a simple truncation representing the shape of the slits.

For a single-slit

$$A(x) = H\left(x + \frac{a}{2}\right)\, H\left(-x + \frac{a}{2}\right), \tag{2.31}$$

where H is the Heaviside function and a is the width of the slit. For a double-slit, it is just two single-slits separated center-to-center by d,

$$A(x) = H\left(x + \frac{d}{2} + \frac{a}{2}\right)\, H\left(-x - \frac{d}{2} + \frac{a}{2}\right) + H\left(x - \frac{d}{2} + \frac{a}{2}\right)\, H\left(-x + \frac{d}{2} + \frac{a}{2}\right). \tag{2.32}$$

For a multi-slit or a grating the function becomes a sum

$$A(x) = \sum_n H\left(x - nd + \frac{a}{2}\right)\, H\left(-x + nd + \frac{a}{2}\right), \tag{2.33}$$

where here d represents the periodicity and the ration a/d is the open fraction. The sum over n can be as small or as large as the number of slits.

2.4.2 Image Charge Effects

When a particle passes the walls of a slit, it interacts through its charge. If the walls are conductors, the surface charges will rearrange themselves to cancel the electric field inside the conductor. This leads to a additional phase or force on the particle. Treating the walls as infinite planes, the well known image charge solution to Laplace's equation can be used.[52] This method of using infinite planes to describe the interaction between the particle and the walls has been used before to describe van der Waals interactions between atoms (or molecules) and nano-fabricated gratings.[51,53,54]

This image charge will produce a potential that will effect the particle as it travels past the walls of the slit. The potential will produce a force that will pull

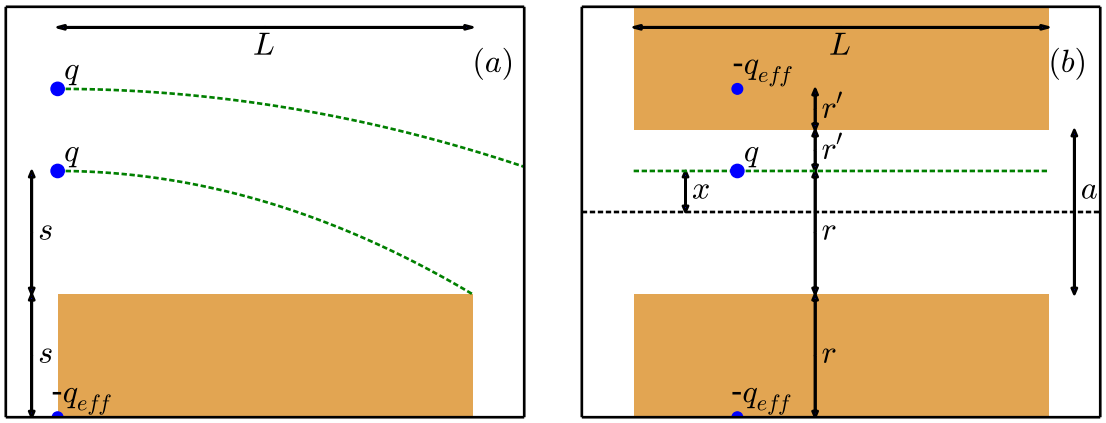

Figure 2.3. Illustration of the image charge effects. **(a)** The image charge potential has an attractive force on the particle. If the particle is within a distance s it will collide with the wall. **(b)** The particle will accumulate a phase shift from the image charge potential.

the particles closer to the wall. If a path was initially close enough to the walls it will be pulled into the walls. This has an effect of narrowing the slits by the distance s, see Figure 2.3(a). The paths not pulled into the walls will accumulate a phase shift as they pass through the potential. For these paths a straight line trajectory is assumed, and the path sees a potential from both walls, see Figure 2.3(b). The image charge potential for a single infinite wall is

$$V(r) = \frac{-kq_{\text{eff}}}{2r}, \tag{2.34}$$

where r is the distance away from the wall, k is Coulomb's constant, and q_{eff} is the effective image charge. This leads to an attractive force on a particle with charge q of

$$F(r) = \frac{kqq_{\text{eff}}}{4r^2}. \tag{2.35}$$

Calculating the maximum distance away that a classical particle can start while still hitting the slit wall, the distance the slits are narrowed on each wall can be

calculated. This distance is

$$s = \left[\frac{kqq_{\text{eff}}}{E} \left(\frac{L}{\pi} \right)^2 \right]^{1/3}, \tag{2.36}$$

where L is the length or thickness of the slit in the z-direction and E is the energy of the particle.

The accumulated phase proportional to the classical action. The path used is shown in Figure 2.3(b) by the dashed (green) line. The phase is given by

$$\phi(x) = \frac{1}{\hbar} \int dt\ L = \frac{1}{\hbar} \int dt\ \frac{m}{2} \left(\dot{x}^2 + \dot{z}^2 \right) - qV(x, z). \tag{2.37}$$

For straight line trajectories the first two terms are constant since there are no change in the velocities. Assuming identical initial velocities these terms are a common global phase that can be ignored. Putting in the potentials, Equation 2.34, from both walls, the leading image charge terms lead to a phase accumulation of

$$\phi(x) = \frac{kqq_{\text{eff}}L}{2\hbar v} \left[\frac{1}{r} + \frac{1}{r'} \right], \tag{2.38}$$

where the L/v comes from the time integration with v being the velocity of the particle. The r and r' variables are the distances from the two walls. Equation 2.38 can be simplified by using the width of the slit a and the distance from center line x,

$$\phi(x) = \frac{2kqq_{\text{eff}}L}{\hbar v a} \left[\frac{1}{1 - \left(\frac{x}{a} \right)^2} \right]. \tag{2.39}$$

The straight line approximation of the trajectories need to be justified. Figure 2.3 shows the trajectory that deviates most from a straight line. The scales in the figure mislead the amount of the curve. The largest value of s, for the experi-

ments presented here, is approximately 0.8 nm, while the value of L is 130 nm. Unfortunately the trajectory due to the image charge force is not analytically solvable,

$$-\sqrt{xx_0}\sqrt{x_0-x}+x_0^{3/2}\cot^{-1}\left[\sqrt{\frac{x_0-x}{x}}\right]=\left[\frac{kqq_{\text{eff}}}{2m}\right]^{1/2}t+\frac{\pi}{2}x_0^{3/2}, \tag{2.40}$$

where x_0 is the initial position of the particle at $t = 0$, with horizontal velocity v. Equation 2.40 can be expanded to find the next leading term of the trajectory. Taking the expansion of the left hand side about $x = x_0$,

$$\frac{\pi}{2}x_0^{3/2}+2x_0\left[x_0-x\right]^{1/2}-\frac{1}{3}\left[x_0-x\right]^{3/2}+O\left[(x_0-x)^{5/2}\right]=\left[\frac{kqq_{\text{eff}}}{2m}\right]^{1/2}t+\frac{\pi}{2}x_0^{3/2}. \tag{2.41}$$

Using only the terms with $O\left[(x_0-x)^{1/2}\right]$ or less, a trajectory can be solved for,

$$x=x_0-\frac{1}{4x_0^2}\left[\frac{kqq_{eff}}{2m}\right]t^2. \tag{2.42}$$

The phase can be found using Equation 2.37. The $\dot{z}$ term still remains constant, and is ignored like before. The phase now becomes,

$$\phi(x)=\frac{m}{24\hbar x_0^4}\left[\frac{kqq_{eff}}{2m}\right]\left(\frac{L}{v}\right)^3+\frac{kqq_{eff}}{2\hbar}\frac{\tanh^{-1}\left\{\left(\frac{1}{4x_0^3}\left[\frac{kqq_{\text{eff}}}{2m}\right]\right)^{1/2}\left(\frac{L}{v}\right)\right\}}{\left(\frac{1}{4x_0}\left[\frac{kqq_{\text{eff}}}{2m}\right]\right)^{1/2}}, \tag{2.43}$$

where the limits of integration were from $t = 0$ to $t = \frac{L}{v}$. The first term in Equation 2.43 will be referred to as $\phi_{\dot{x}}(x)$ and the second term will be referred to as $\phi_{q_{eff}}(x)$. After expanding the inverse hyperbolic tangent, $\phi_{q_{\text{eff}}}(x)$ becomes,

$$\phi_{q_{eff}}(x)=\frac{kqq_{\text{eff}}}{2\hbar}\frac{L}{x_0v}\left\{1+\frac{1}{3}\left(\frac{1}{4x_0^3}\left[\frac{kqq_{\text{eff}}}{2m}\right]\right)\left(\frac{L}{v}\right)^2\right\}. \tag{2.44}$$

The first term is the straight line trajectory and as long as the second term is small

compared to 1, then the straight line trajectory remains valid. The largest deflected trajectory that makes it through the grating and subsequently would cause the largest deviation from a straight line is when $x_0 = s$. Substituting $s = \left\{\frac{4}{\pi}\left[\frac{kqq_{\text{eff}}}{2m}\right]\left(\frac{L}{v}\right)^2\right\}^{1/3}$ into the second term in the braces of Equation 2.44 gives a value of $\pi/48 = 0.065$, which for the situation is much less than 1. Similarly, experimental values can be substituted into $\phi_{\dot{x}}(x)$ giving a value of approximately $\pi/200$. These values are a small contribution to the accumulated phase and thus justifies the straight line approximation to the trajectories.

2.4.3 Random Potentials

Previous experiments have had the need of additional interactions between a particle and a slit to get agreement for single- and multi-slit diffraction.[33] This interaction was modeled by a series of random static Gaussian potentials.

The physical system, that motivates the random potential model, is based on contact potential. the typical size of contact potentials is .1-1 eV. For example, the contact potential between different crystal faces of copper is about 0.4 eV.[55]

This model was adopted to help describe a particle traveling through a slit. In the model the potential had the form of

$$V_{\text{random}}(x) = \sum_i A_i \exp\left[-\frac{4\ln(2)(x - x_i)^2}{\sigma_i^2}\right]. \tag{2.45}$$

Here A_i is the amplitude, σ_i is the Full Width Half Max (FWHM) value, x_i is the center of the i^{th} potential, and the $4\ln(2)$ comes from relationship between the variance of a Gaussian and the FWHM, see Figure 2.4.

The values of σ_i and A_i are obtained from random number generators, while $x_i = \sigma_i + \sigma_{i-1}$. The random number generators are Gaussian distributions with means and FWHM values. The values used, in the Talbot-Lau experiment described

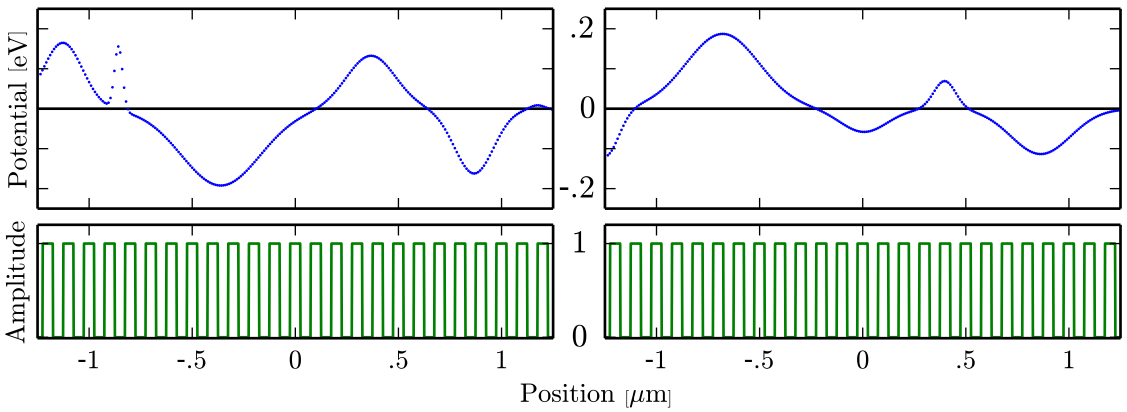

Figure 2.4. Illustration of random potentials. The upper graphs show two different random potentials generated from Equation 2.45. The bottoms graphs illustrates the dimensions typical grating. They were made using Equation 2.33, with $a = 50$nm and $d = 100$nm.

in Chapter 5 (and used in Figure 2.4) are means of 250 nm for σ_i and 0 eV for A_i and the FWHM is 250 nm and 0.35 eV respectively.

The phase accumulated was calculated identically to Equation 2.37. An amplitude of about 0.2 eV gives a phase shift on the order of π. Because the electrons go through different vertical (y) sections of the slit, the wave function was propagated through each slit multiple times with different random potentials. Then individual wave function are then incoherently added up, by first calculating the individual probability distributions then adding each together.

The image charge effects are symmetric about the center of individual slits and it has an identical shape between slits on the plane. This generally has the effect of broadening the single-slit envelope. It does not however effect the zeros of the double-slit or multi-slit, see Figure 2.1. The random potential caused the zeroes to come up and destroy some of the contrast, similar to Figure 2.2. Both effects were necessary to properly model the experimental double-slit diffraction data, see Chapter 4.

2.4.4 Implementation

The first collimation slits of the experiments were considered to be incoherent sources. To describe these incoherent sources the wave function was initialized as

$$\Psi_{\chi_i}(x) = \delta(x - \chi_i), \tag{2.46}$$

where χ_i is the center of the point source and located in the first collimation slit. Multiple point sources were propagated through the system. A final probability distribution was calculated for each initial points source. Then each probability distribution was added incoherently.

To accound for the image charge and random potential effects, a new effective width was calculated for the slits ($a' = a - 2s$), modifying Equation 2.33. Then Equation 2.30, with the two phases (the image charge phase from Equation 2.39 and the random potential phase calculated from Equation 2.45) along with the modified A, were applied to the wave function. Then the wave function was propagated to the next component.

2.5 Electron Biprism

An electron biprism is constructed of a fine metallic filament or wire placed between two parallel plate electrodes. A voltage V_{bp} is applied to the biprims wire causing a potential, which can be approximated as[27]

$$V(r) = V_{bp}\frac{\ln(r/R_{el})}{\ln(R_{bp}/R_{el})}, \tag{2.47}$$

where r is the radial distance from the wire, R_{bp} is the radius of the wire, and R_{el} is the distance from the wire to the grounded electrode. The potential given by Equation 2.47 results in a classical deflection to a particle traveling near the wire in the

plane whose normal is parallel to the wire, which for small angles (δ) is[27]

$$\delta = \frac{\pi q V_{bp})}{2E \ln(R_{bp}/R_{el})}. \tag{2.48}$$

As seen from Equation 2.48, the electron biprism is useful because it can cause a deflection that is independent of distance from the wire. This is analogous to the Fresnel double prism for light.

Recent attempts at making a large area interferometer[3] required the modeling of an electron biprism with Feynman's path integral formalism. The small deflection angles, where Equation 2.48 is valid, motivated a straight line trajectory approach. The wave function was propagated through the system with the free space propagator, as described above. At the plane of the biprism, Equation 2.30 was applied. The biprism is treated as a solid barrier that blocks a portion of the plane, effecting the amplitude of the wave function,

$$A_{bp}(x) = H(-x - R_{bp}) + H(x - R_{bp}). \tag{2.49}$$

The electrons that pass the biprism accumulate a phase shift. This phase shift is due to the biprism potential given by Equation 2.47.

The phase shift is calculated using Equation 2.37. The $\dot{x}$ and $\dot{z}$ terms are not calculated again because they are accounted for during the free space propagation. The phase is,

$$\phi_{bp}(x) = \frac{q}{\hbar} \int dt\ V_{bp}(r) = \frac{q}{\hbar v} \int_{-\infty}^{\infty} dz\ V_{bp}(r(x,z)), \tag{2.50}$$

where the last relation assumed a straight trajectory in z with a constant velocity v. This integral diverges; however only local phase differences accumulated for trajectories at different distances from the wire are relevant.

A phase difference between trajectories can be calculated. Two paths at x and x' have a phase difference of

$$\Delta\phi_{bp}(x,x') = \frac{q}{\hbar v}\frac{V_{bp}}{\ln(R_{bp}/R_{el})}\int_{-\infty}^{\infty} dz\ \ln\left(\frac{\left[x^2+z^2\right]^{1/2}}{R_{el}}\right) - \ln\left(\frac{\left[x'^2+z^2\right]^{1/2}}{R_{el}}\right)$$

$$= \frac{q}{\hbar v}\frac{V_{bp}}{\ln(R_{bp}/R_{el})}\frac{1}{2}\int_{-\infty}^{\infty} dz\ \ln\left(x^2+z^2\right) - \ln\left(x'^2+z^2\right). \tag{2.51}$$

Using the known integral[56]

$$\int_{-\infty}^{\infty} du\ \ln\left(x^2+u^2\right) = u\left[\ln(u^2+x^2)-2\right] + 2x\tan^{-1}\left(\frac{u}{x}\right), \tag{2.52}$$

Equation 2.51 can be evaluated,

$$\Delta\phi_{bp}(x,x') = \frac{q}{\hbar v}\frac{V_{bp}}{\ln(R_{bp}/R_{el})}\frac{1}{2}\left\{z\left[\ln(z^2+x^2)-\ln(z^2+x'^2)\right]\right.$$
$$\left. + 2x\tan^{-1}\left(\frac{z}{x}\right) - 2x'\tan^{-1}\left(\frac{z}{x'}\right)\right\}_{-\infty}^{\infty} \tag{2.53}$$

$$= \frac{q\pi}{\hbar v}\frac{V_{bp}}{\ln(R_{bp}/R_{el})}\left(x-x'\right). \tag{2.54}$$

The first terms in Equation 2.53 cancels out with the evaluation at the limits. The last two terms' arc-tangents evaluate to $\pm\pi/2$ at the limits, giving the π in Equation 2.54. The global phase can be ignored, which is when $x'=0$. The phase at the biprism plane can be simply written as

$$\phi_{bp}(x) = \frac{q\pi}{\hbar v}\frac{V_{bp}}{\ln(R_{bp}/R_{el})}x. \tag{2.55}$$

The straight line trajectory approach, while not mathematically justified here, accurately reproduced the results published by Caprez et al.[3] Equation 2.55 produces a linear phase shift along x, this causes a deflection of an electron beam that

is independent of the distance from the biprism wire. Similarly the derivative of Equation 2.55 in x, divided by mv, gives the deflection angle, Equation 2.48.

2.6 Path Integral Simulations

Two major simulation were developed and ran to model both the electron double-slit experiment, see Chapter 4, and the Talbot-Lau interferometer, see Chapter 5. The simulations utilized Feynman's path integral formalism outlined above. The simulations were written in FORTRAN and ran on the University of Nebraska-Lincoln Holland Computing Center's clusters. The code is too lengthy to go into detail here, see Appendix C.

Chapter 3

Experimental Setup and Image Analysis

3.1 Introduction

Both experiments discussed in Chapter 4 and Chapter 5 were completed on the same general electron beam system. For each experiment some of the componets were different. To prevent redundancy in the discription of the experimental setup the major components are listed in the next section. The third section contains an overview of the electron detection process and the last section covers the image analysis techniques employed.

3.2 System Components

The vacuum system is shown in Figure 3.1 with the main components identified. The compoenents are discussed in detail in the following subsections.

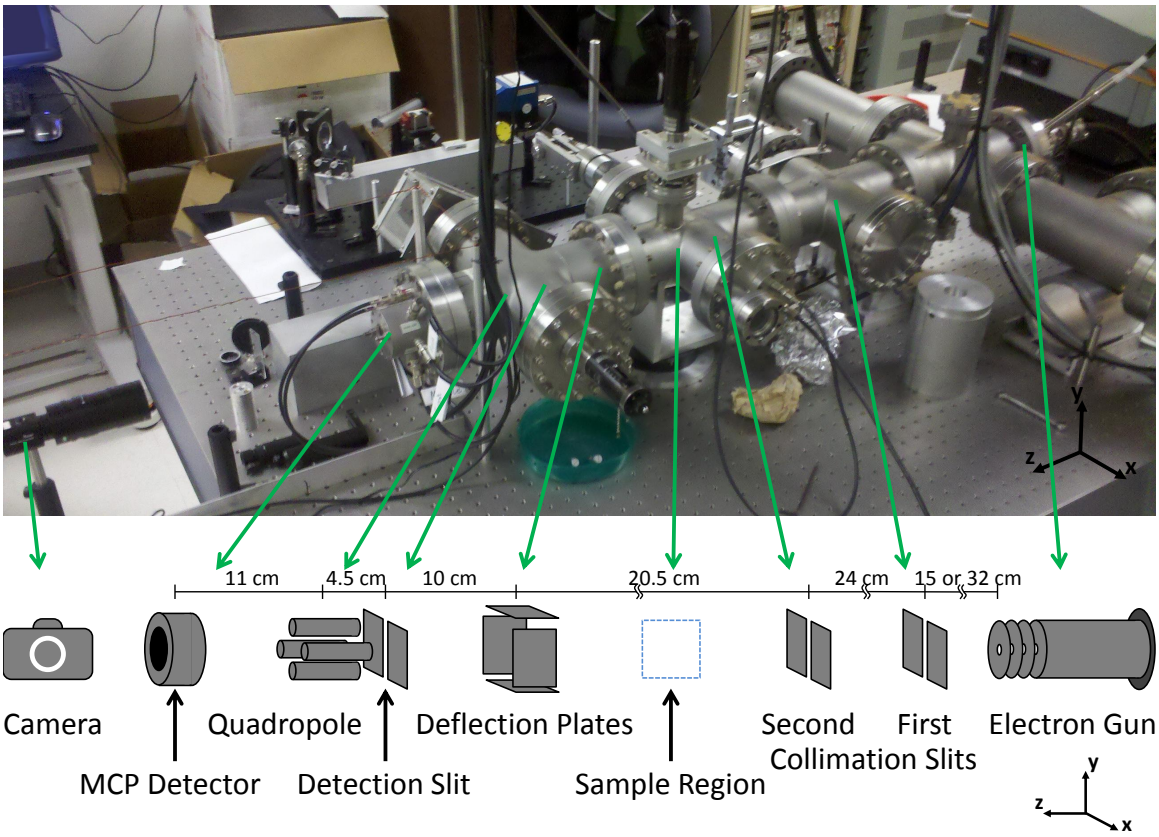

Figure 3.1. The vacuum system is shown in the picture above. The major components are indicated below the image with the spatial separations listed.

3.2.1 Electron Guns

A source of electrons were needed for the experiments. Depending on the requirements for the individual experiments, two different electron guns were used. The main consideration was the energy range of the gun and the ease of adjustment of the central energy.

The double-slit experiment (see Chapter 4) required lower energies to separate the diffraction orders to larger angles. The de Broglie wavelength (λ_{dB}) scales with the inverse of square root of energy (E),

$$\lambda_{dB} = \frac{h}{\sqrt{2mE}}, \tag{3.1}$$

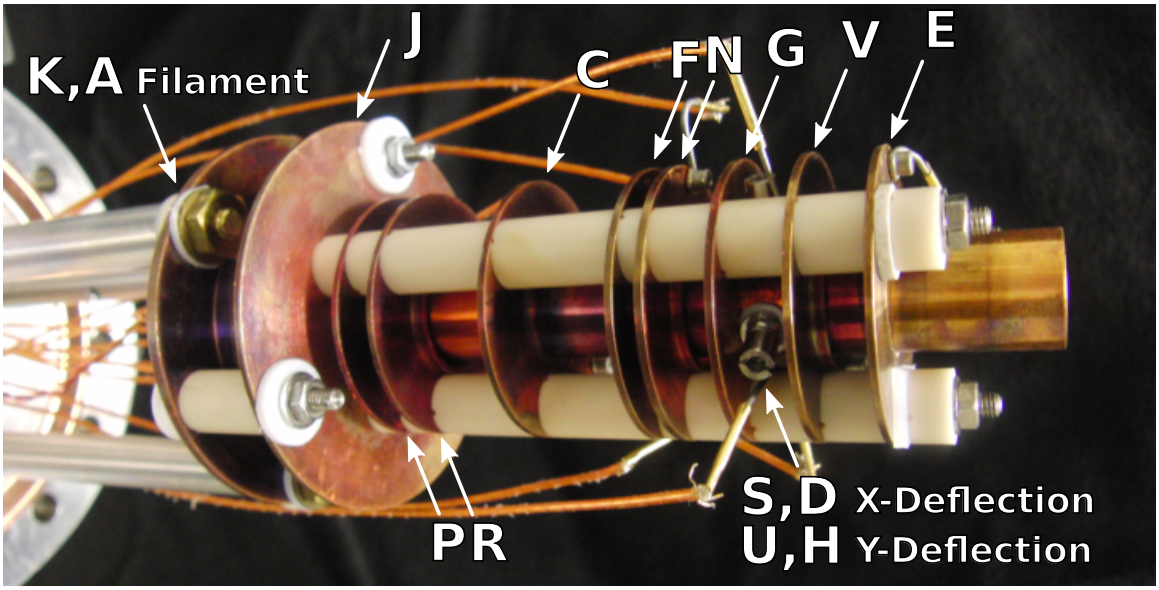

Figure 3.2. The lower energy electron gun was capable of energies ranging from 50 eV to 1 keV, The labels refer to the flanges pin letters.

where h is Planck's constant and m is the mass of the electron. Using Equation 3.1 and 2.5 the diffraction angle can be seen to be inversely proportional to the square root of energy. Hoping to see the diffraction pattern directly on the detector without any magnification, an electron gun was chosen that had a range of energy from 50 eV to 1 keV. This gun (donated by the University of Utrecht) produced electrons by thermionic emission from a tungsten wire with an energy spread of less than 3 eV, see Figure 3.2. It used 9 focusing elements and 4 individually addressable plates for deflection to produce a usable beam. A Topward 3003A power supply ran approximately 2 amps of current through the tungsten wire and was floated on a Ortec 556 high voltage power supply to provide the accelerating voltage for the electrons. The focusing elements were individually held a different potentials with multiple Agilent E3612A DC power supplies The opposing deflection plates could be held at a potential difference while floated at a specific center voltage using a combination of a potentiometer box and two Agilent power supplies. The multiple independent adjustments made changing the energy while keeping a well focused beam difficult.

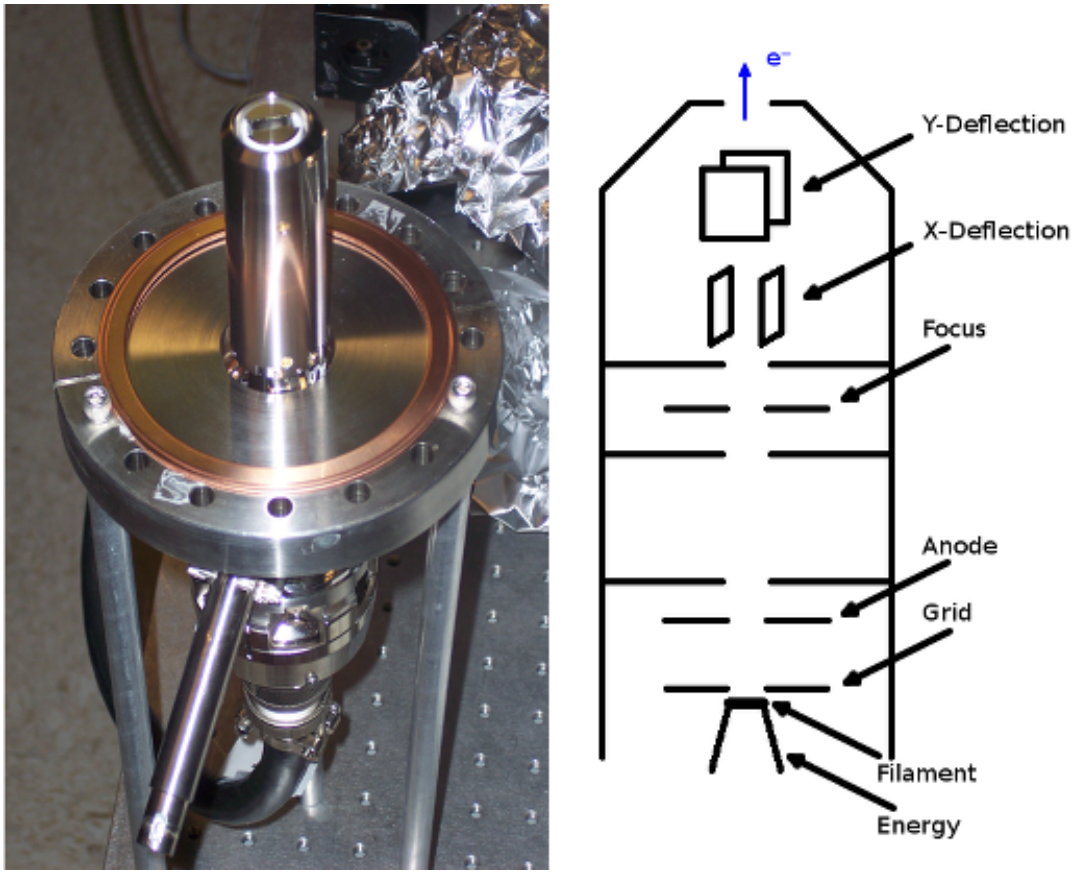

Figure 3.3. The higher energy electron gun was capable of energies ranging from 100 eV to 10 keV. The gun was a Kimball Physics Egg-3101

The Talbot-Lau experiment (see Chapter 5) needed larger energies and the capability to easily sweep the energy. Previous experiments with similar gratings demonstrated the need for energies of 500 eV or larger.[33,34] This energy was necessary to minimize unwanted interactions effects with the grating. To properly demonstrate a three grating Talbot-Lau interferometer, It was necessary to observe the maxima in contrast. These occur when the grating separation (L) is an integer multiples of half the Talbot length (L_T), which is $L_T = 2d^2/\lambda_{dB}$, where d is the grating period.[57] If the grating periods and separation distances are fixed, the only adjustable parameter is E. Using the above and Equation 3.1, the maxima occur at

energies of

$$E = \frac{1}{2m}\left(\frac{Lh}{nd^2}\right)^2, \tag{3.2}$$

where n in an integer and the n^{th} revival of the Fourier image of the first grating.[58]

The electron gun chosen for the Talbot-lau experiment was a Kimball Physics Egg-3101, see Figure 3.3. This gun had an energy range capability of 100 eV to 10 keV, with an estimated energy spread of 1 eV. The electrons were produced by thermionic emission from a lanthanium hexaboride cathode. A pair of deflection plates and a single focusing element allowed for for the production of a beam. Both the deflection plates and the focusing element were controlled by power supplies that would ramp proportionally to the electron energy. This allowed for, when properly aligned, the sweeping of energies with minimal adjustments, thus the covering of multiple contrast maxima. Using Equation 3.1, with a grating separation of 3 mm and a grating period of 100 nm, the $n = 4, 5, 6, ..., 37$ orders would be reachable.

The two electron guns were situated at different locations in the vacuum system. The lower energy electron gun's exit was located 15 cm from the first collimation slit, see Figure 3.1, while the higher energy electron gun's was located 32 cm from it.

3.2.2 Beam Collimation

Previous experiments with this electron beam system utilized different collimation slits.[33,34,59] Previously the electron beam was collimated with laser cut 5 μm wide by 3 mm tall metal slits. These collimation slits were manipulated externally from the vacuum chamber with horizontal linear feedthroughs. No vertical adjustment was necessary because of the tall height of the slits. During the double-slit exper-

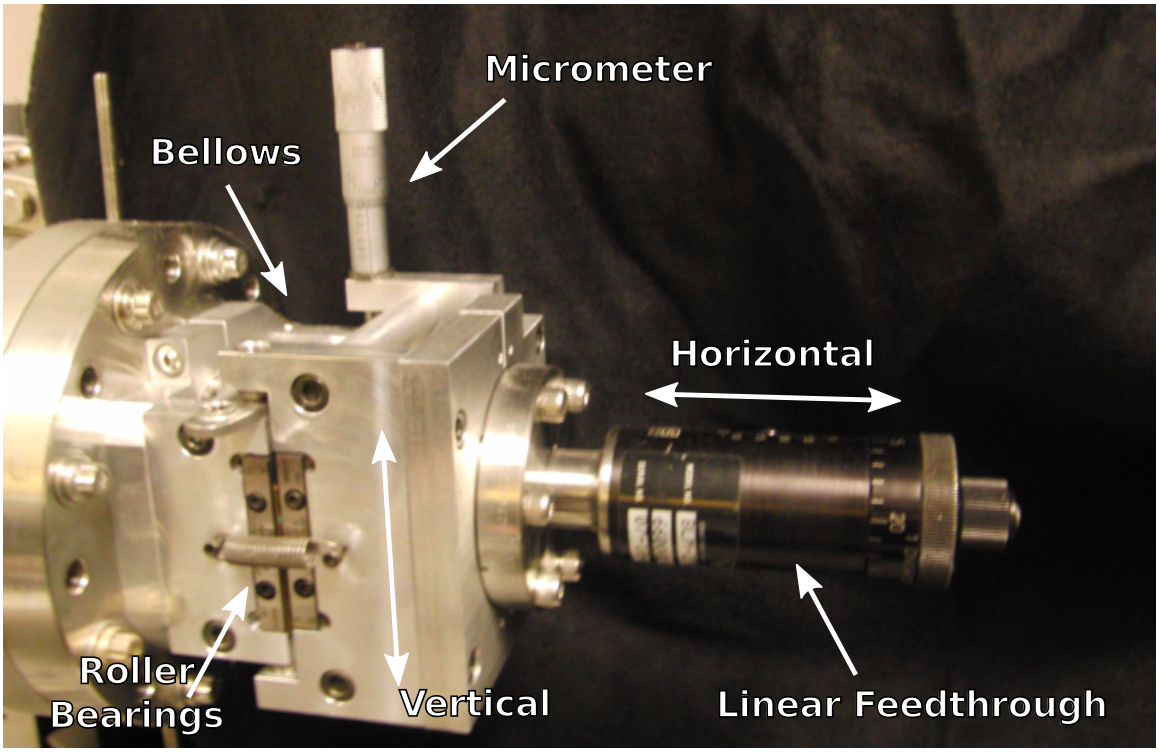

Figure 3.4. The vertical translation system allows for precise vertical control of the first collimation slit, while the linear feedthrough controls the horizontal adjustments

iment, the rough edges (approximately 500 nm roughness) caused the diffraction pattern to appear unsatisfactory for publication.

Focused ion beam (FIB) milled silicon-nitride membrane windows were chosen to replace the metal collimation slits. These slits had extremely smooth edges (less than 10 nm roughness). Due to the thickness of the membranes and the manufacturing process the aspect ratio of the slits could not be too large or the membranes would collapse. The slits now needed to be manipulated vertically as well as horizontally.

A vertical translation system was designed and built to manipulate the first collimation slit, see Figure 3.4. The translation system was built in the University of Nebraska-Lincoln, Department of Physics, student machine shop. The system translated on a pair of stock crossed roller bearings. The hydraulically formed bel-

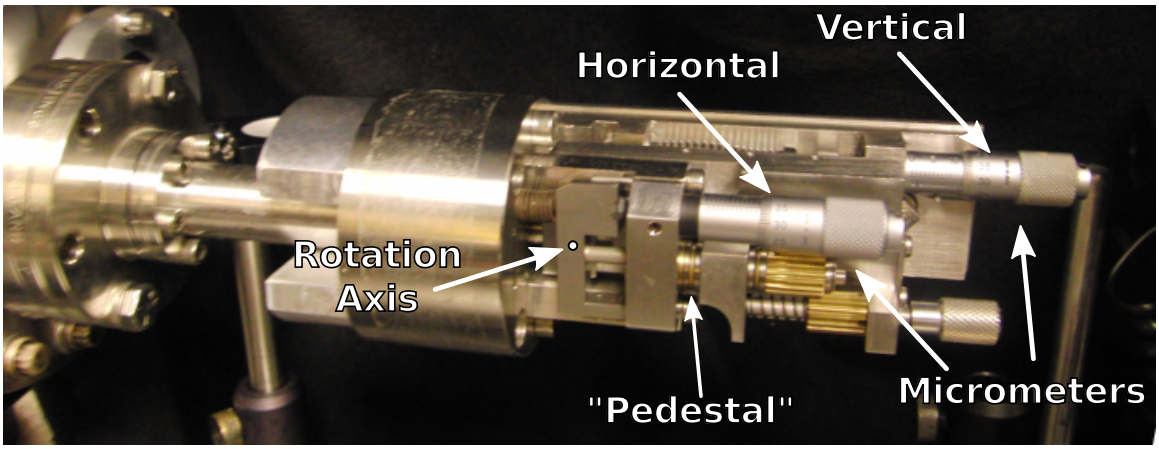

Figure 3.5. The second collimation slit manipulator is pictured above. The horizontal and vertical micrometers allow for precise manipulation of the collimation slit over smaller distances while the "pedestal's" steps cover a larger horizontal distance

lows allowed the system to translated while still maintaining vacuum. The micrometer screw enabled precise control of the vertical position of the collimation slit, while the linear feedthrough provided the horizontal adjustment.

To allow the second collimation slit to be adjusted vertically a different approach was used. A repurposed aperture manipulator, from a decommissioned electron microscope, was adapted to manipulate the second collimation slit, see Figure 3.5. The manipulator was designed to be able to select from 4 apertures, that were separated horizontally by approximately 2.85 mm, by the adjustment of a "pedestal". Then the micrometer screws were used to fine tune the position of the aperture. The horizontal micrometer's motion is limited to less than 1.5 mm, meaning that there are horizontal positions that the manipulator can not reach. A new "pedestal" was built to have smaller steps or approximately 1.25 mm. This allowed the different "pedestal" steps to overlap while still allowing the manipulator to cover a large range of travel. One drawback of this manipulator is that the vertical travel is coupled to a rotation of the collimation slit. This does not pose a problem for circular apertures, but for a slit, the rotation can be a hindrance, making a beam that is slanted. The rotation axis is at the front of the manipulator and ro-

tates in the xy-plane. For the current setup the rotation arm is approximately 32 cm long. This would cause a 3 mrad rotation for a 1 mm vertical travel. Currently this does not seem to hinder the beam collimation but in the future the rotation may need to be resolved.

Either one or two collimation slits were used to define the electron beam from the gun. The second collimation slit was located 24 cm from the first collimation slit, see Figure 3.1. In the double-slit diffraction experiment (see Chapter 4) only a single collimation slit was needed because the double-slit itself restricted the transverse momentum spread allowed. A 2 μm wide by 10 μm tall slit was used. The slit was FIB milled in a 100 nm thick silicon-nitride membrane. After milling the silicon-nitride was coated with approximately 5 nm of titanium and then approximately 10 nm of gold on both sides.

For the Talbot-Lau (see Chapter 5) experiment two collimation slits were needed to restrict the transverse momentum spread. The 2 μm wide slit was moved to the second collimation slit position and another slit was made to act as the first collimation slit. A 5 μm wide by 100 μm tall slit was milled in a 2 μm thick silicon-nitride membrane. Again after milling the membrane was coated with metal. The geometric angular spread of these two membranes is $\theta_{geom} = (5 + 2)\mu\text{m}/24\text{cm} = 29\mu\text{rad}$. This agrees with the observed beam width at the detection slit, located 30.5 cm from the second collimation slit, of 10 μm.

3.2.3 Deflection Plates and Detection Slit

To control the position of the beam or pattern after it passes through the sample region two pairs of deflection plates are used. The deflection plates were located 20.5 cm from the second collimation slit, see Figure 3.1 and Figure 3.6. The plates were used to position the resulting pattern on the two-dimensional detector or scan the pattern across the detection slit.

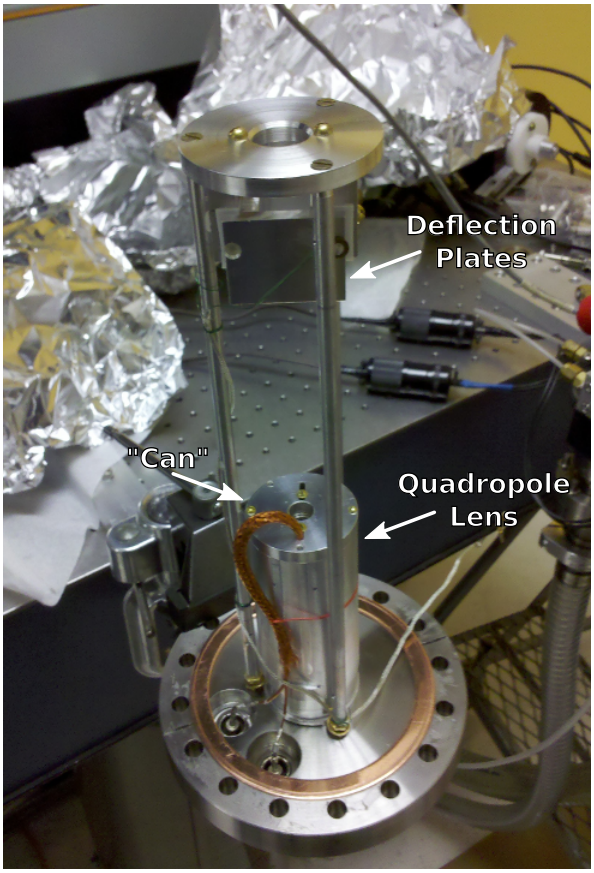

Figure 3.6. The electrons travel from the top where they pass through the deflection plates and travel on to the quadropole lens and then to the detector. The detection slit (not shown) would be in between the the "can" and the deflection plates.

The detection slit was located 30.5 cm from the second collimation slit, see Figure 3.1. The slit was a 5 μm wide by 3 mm tall molybdenum slit. The horizontal position of the detection slit was controlled by a linear feedthrough, which if needed could completely be remove from the beam path. The diffraction pattern could be sampled by either moving the linear feedthrough or by deflecting the pattern with the deflection plates. Both methods produced the same results, but the deflection plates had finer spatial control and could be scanned by a function generator if needed.

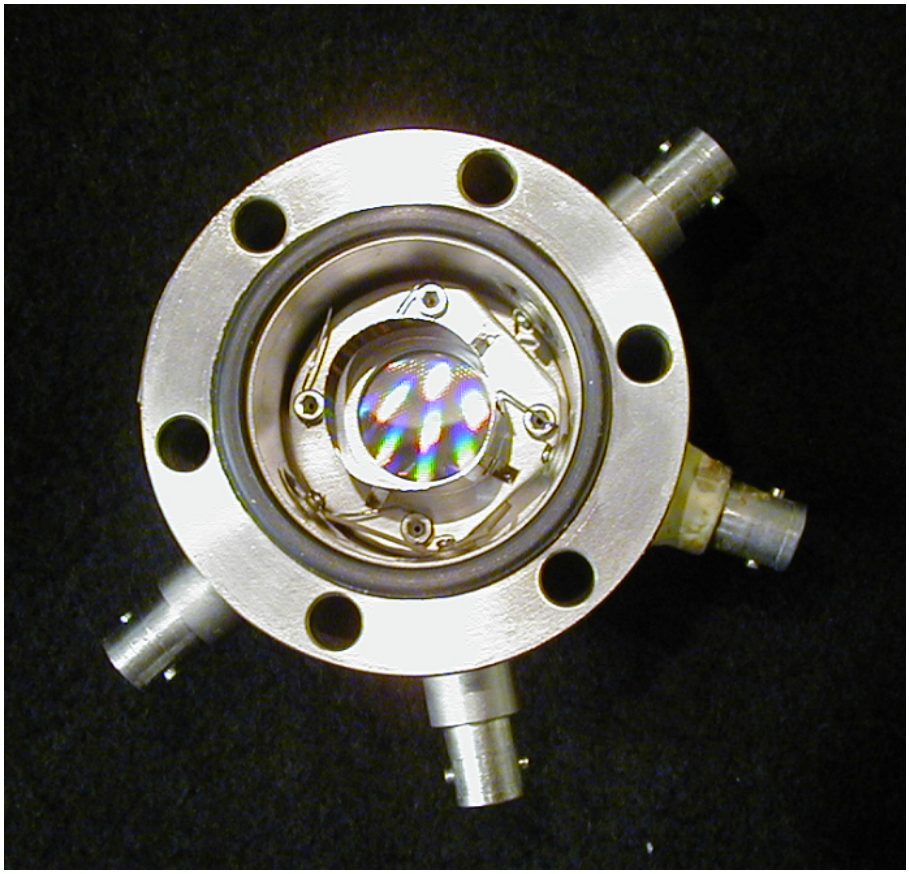

Figure 3.7. The electrons were detected by a Beam Imaging Systems model BOS-18 two chevron stack micro-channel plate phosphor screen detector

3.2.4 Detection

The electron detector used was a Beam Imaging Systems model BOS-18 two chevron stack micro-channel plate (MCP) and phosphor screen detector, see Figure 3.7. The MCP consists of an regular array of tubes made of highly resistive material. The tubes are approximately 10 μm in diameter with a center to center diameter of approximately 12 μm. The tubes are a a slight angle of approximately 5°. Each micro-channel act as an electron multiplier. A large potential is put across the ends of the tubes. A single electron entering the low potential end will starts a cascade effect. After hitting a wall the first electron will liberate multiple electrons. Then the liberated electrons will be accelerated down the tube towards the higher potential, hitting another wall, generating more electrons. An single initial electron

will end up with approximately 10^4 electrons. In this two stack model the electrons from the first MCP are sent into another MCP, where they will be amplified more. After the two MCP's the electrons are accelerated towards a phosphor screen. At the phosphor screen the electrons excite the phosphor and the result is a flash of light indicating an electron detection. The entire detector has a diameter of 18 mm.

The MCP detector allows for the viewing of a two-dimensional pattern, because of the array of holes. The finite size of the micro-channels, the blurring from multiple MCP's, and the phosphor screen all cause the MCP detector to have a finite resolution. To overcome this an electrostatic quadropole lens was employed. The lens was placed 11 cm before the detector, see Figure 3.1. The lens consists of four voltage addressable rods parallel to the beam arranged at 90° from each other. Each opposite pair is held at the same potential, with the horizontal pair being at $+V$ and the vertical pair being at $-V$. This allows expansion of the pattern in the horizontal direction but depending on the voltage either contraction or expansion in the vertical direction. The lens was necessary because the entire size of some non-magnified patterns would be comparable to the resolution of the MCP detector.

3.2.5 Vacuum Chamber

The experiments were performed in a stainless steel vacuum chamber shown in Figure 3.1. The pressure was held at or below 10^{-7} Torr. This was accomplished through the use of a turbo pump backed by a rotary vane pump (not shown in Figure 3.1).

The static external magnetic fields were shielded to better than 0.5 μT. A dual layer of high magnetic permeability mu-metal allowed for the attenuation of external field by a factor of 100.

To prevent stray electrons from bouncing around and getting to the detector multiple precaution were taken. Two electron beam blocks were placed along the

vacuum chamber. One between the electron gun and the first collimation slit and the other between the sample region and the deflection plates, see Figure 3.1. An electron beam block fills up a specific region of the vacuum chamber and only allows the line of sight through the center of the system, but still allowing for air to flow through the system to enable pumping. Another precaution was to place the "can" over the detector, shown in Figure 3.6. The small opening of the "can" prevents electrons from hitting the detector unless they travel straight down the system. If the detection slit is used the hole in the "can" is covered up allowing only the electrons traveling through the slit to reach the detector.

3.2.6 Sample Region

The sample region shown in Figure 3.1 has access from three sides. Initially, for the double-slit diffraction experiment, the double-slit mount was connected to a "wobble-flange" and linear feedthrough connected to the side of of the vacuum chamber. The horizontal motion was controlled by the feedthrough while the vertical motion was controlled by tightening an appropriate bolt on a special flange. The flange consisted of multiple viton o-rings that would be compressed non-uniformly causing the entire flange to tilt and vertically shift the double-slit. While the motion was not extremely accurate, care could be taken to prevent the vacuum seal from failing and the double-slit could be positioned correctly.

While the "wobble-flange" and linear feedthrough design worked, the motion was not repeatable or precise enough for the Talbot-Lau interferometer and other future experiments[5]. Using two commercially available translation stages and an edge welded bellows, a system was designed and constructed in the University of Nebraska-Lincoln, Department of Physics's student machine shop, see Figure 3.8. The two micrometers allowed for micron level positioning and repeatability, all while maintaining vacuum. The translation stages 25.4 mm of travel allowed the

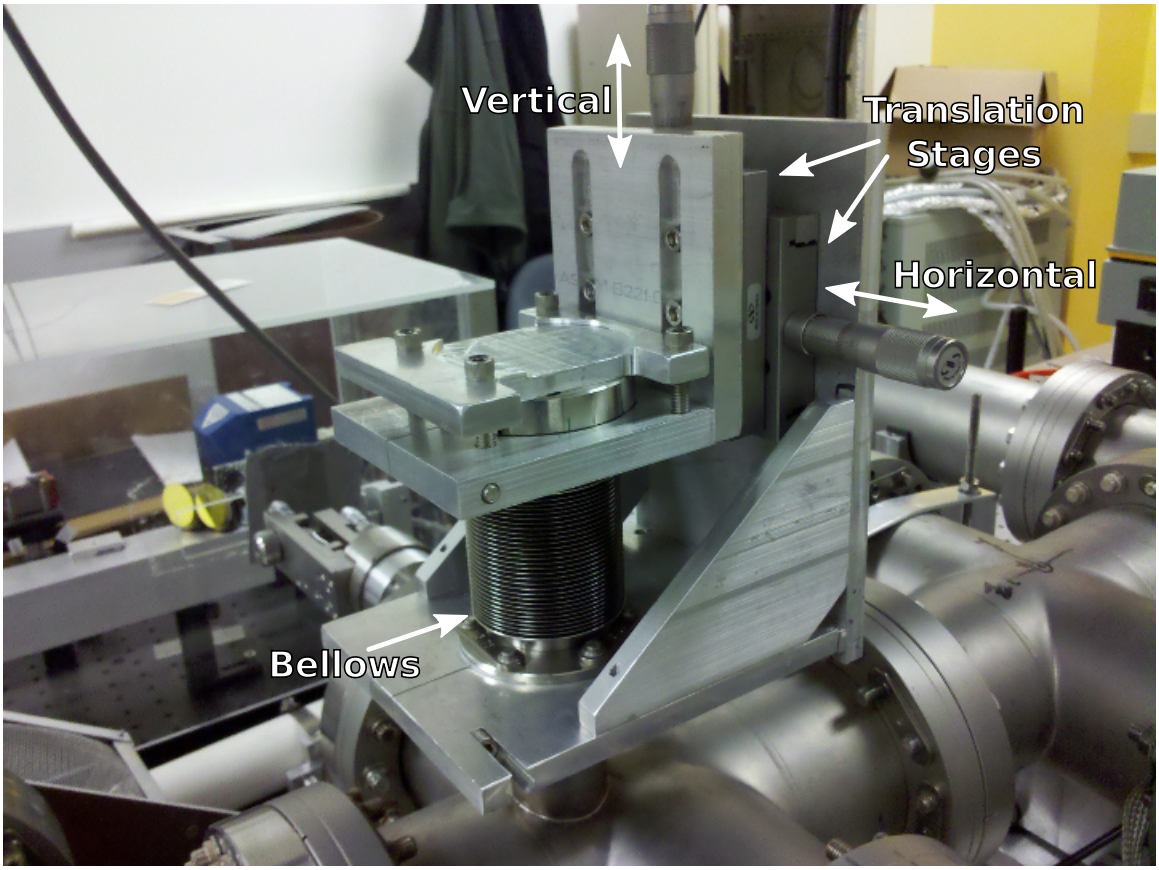

Figure 3.8. The two-dimensional sample manipulator can move the sample in and out of the beam, with micron level positioning and repeatablity

two-dimensional manipulator to move the Talbot-Lau interferometer out of the beam to allow for profiling of the beam.

3.3 Data Acquisition

Depending on the application, the electron events could be counted multiple ways. The next section covers the general methods used to collect data.

3.3.1 Electron Counting

Each individual electron event could be counted. After amplification by the MCP's each electron event would impart charge on the phosphor screen. With a simple cir-

cuit, the excess charge could be turned into a small voltage pulse. On average the pulses had about -5 mV in amplitude. These pulses where amplified by a factor of approximately 200 and then discriminated from the background. After discrimination the pulses where sent to multiple different counters.

The electron counts where sent to a general counter and a multichannel scaler (MCS). The general counter was a Stanford Research Systems SR400 dual gated photon counter. This counter was used to monitor the number of electrons hitting the detector to prevent saturation and damage. The MCS was an Ortec MCS-pci. The MCS allows for the recording of counts as a function of time. The MCS could be externally triggered from an external device. For example, for beam profiling the MCS was triggered by a function generator that would ramp the voltage on the deflection plates, see Section 3.2.3. The deflection plates would pass the beam over the detection slit sampling different portions of the beam. The time recorded by the MCS would be related to a voltage from the function generator which in turn would relate to a deflection position, thus allowing the MCS to record the profile of the beam. Multiple passes would be stacked on top of each other allowing for better statistics.

3.3.2 Camera

To record the position of the electron events on the phosphor screen a camera was utilized to record the events. A Watec WAT-902B black and white camera was used to capture images at 30 frames per second. The images were displayed on a monitor to help with beam and sample alignments. The images were also sent to a computer for recording and analysis.

The computer utilized a National Instruments PCI-1409 frame grabber card to convert the analog video signal to a digital format. A Labview software program was developed to be able to monitor and preform simple image analysis, see

Appendix B for the Labview code. The main features of this program are: image acquisition, cutoff filter, summing, projecting, and sequence saving. The program would utilize the frame grabber card to convert the analog images to 8 bit images. This means that each pixel could have a intensity ranging from 0-255. Because there is some intrinsic background noise associated with the camera a cutoff filter could be used to set low intensity pixels to zero. The summing feature allowed for multiple images to be stacked onto of one another while the intensity could be scaled to prevent saturation. The cutoff filter was useful to prevent the background noise from dominating the summed image. The summed image could be projected onto the horizontal axis to produce a one-dimensional image of the beam or pattern. The summed image and projection were especially useful in conjunction with the quadropole lens, see Section 3.2.4, to detect deflections in the beam or measure the beam width. The final feature of the Labview program was the sequence saving feature. This allowed for a set number of images to be saved to the hard drive in bitmap format. This feature was used extensively during the double-slit experiment, see Chapter 4, to save images for further analysis, which will be discussed in the next section.

3.4 Image Analysis

One of the goals of the the double-slit experiment was to see a build-up of a diffraction pattern from single electrons. The electron events from the MCP detector were captured by the camera and saved as images by the Labview program, see Figure 3.9. These images had several problems. First, the background from the camera (even when viewing nothing) would cause periodic stripes if the images were summed. Second, each electron event would only be shown on every other line in the image. This was caused by the interlaced pixel capture of the camera

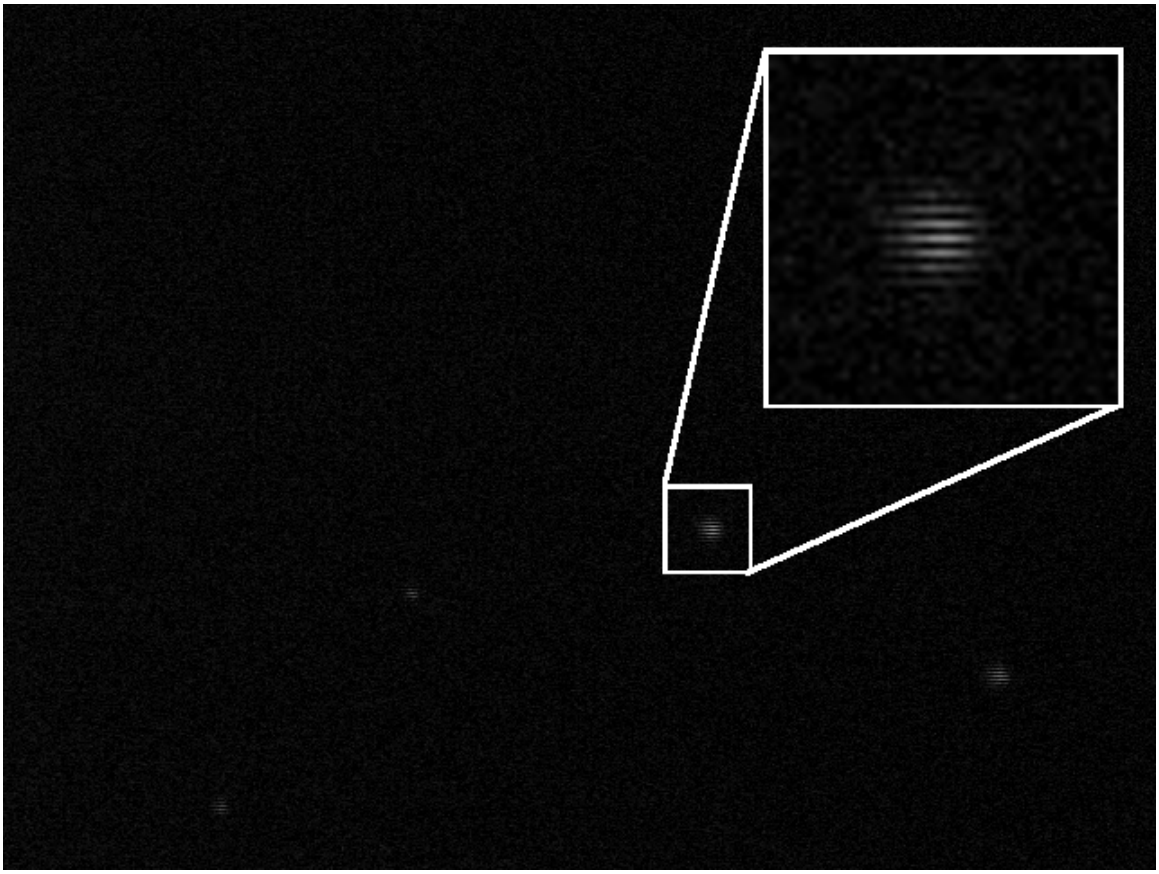

Figure 3.9. Several electron events from the MCP detector captured by the camera. The inset shows a blow up section of the image, showing a single electron event

and the fast decay time of the phosphor screen (about 1 ms). Third, the intensity of each electron event was not uniform. This is most likely due to variation in the MCP amplification. A progressive scan camera (acquires all pixel data at one time) would overcome the interlacing problem. The minimal amount of light coming from each electron event required a very sensitive low-light camera. All the reasonable progressive scan camera commercially available did not have enough sensitivity.

With the low count rates needed to build up a diffraction pattern from single electrons, these problems produced sub par patterns. To make a more uniform and background free build up a "blob" detection scheme[60,61] was utilized. The following sections will cover how this scheme was implemented.

3.4.1 Overview

The "blob" detection scheme is based off scale-space theory[62]. The image intensities can be represented by $f(x, y)$. First the image is represented in a scale space,

$$L(x, y, t) = \int_{-\infty}^{\infty} dx' \int_{-\infty}^{\infty} dy' \, f(x', y') g(x - x', y - y', t). \tag{3.3}$$

Which is taking the convolution of the data with a Gaussian kernel,

$$g(x, y, t) = \frac{1}{2\pi t} \exp\left[-\frac{x^2 + y^2}{2t}\right], \tag{3.4}$$

where t represents the length of the scale space. The next step is to determine the scale-normalized determinant of the Hessian matrix of Equation 3.3, ,

$$H(x, y, t) = t^2 \left(L_{xx} L_{yy} - L_{xy}^2\right), \tag{3.5}$$

where L_{xx} represent the second partial derivative in x and similarly for L_{yy} and L_{xy}. Finally, the local maxima are found in x, y, and t. These maxima are blob points with scales t.

For illustration an example is considered. Suppose the image consists of a single blob located at (x_0, y_0) and with amplitude A. Also this blobs is shaped like a Gaussian with width c. The image intensity would be

$$f(x, y) = A \exp\left[-\frac{(x - x_0)^2 + (y - y_0)^2}{2c}\right]. \tag{3.6}$$

The scale space representation would then be

$$L(x, y, t) = \frac{Ac}{t + c} \exp\left[-\frac{(x - x_0)^2 + (y - y_0)^2}{2(t + c)}\right]. \tag{3.7}$$

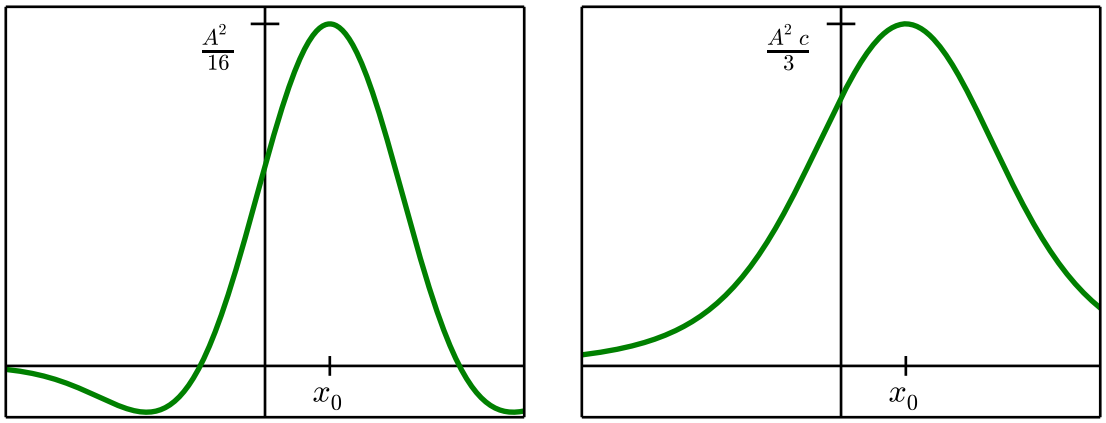

Figure 3.10. Shown above is a comparison of the scale-normalized determinant of the Hessian matrix of $L(x, y = y_0, t = c)$, shown left, and the integrated $H(x, y, t)$, shown right.

The scale-normalized determinant of the Hessian matrix of L can be calculated,

$$H(x, y, t) = \frac{t^2 c^2 A^2}{(t+c)^5}\left[t + c - (x - x_0)^2 - (y - y_0)^2\right] \exp\left[-\frac{(x - x_0)^2 + (y - y_0)^2}{2(t+c)}\right]. \tag{3.8}$$

It can be easily seen that Equation 3.8 is maximum when $x = x_0$ and $y = y_0$. The maximum in t can be determined by taking the partial derivative with respect to t at (x_0, y_0),

$$\frac{\partial H(x = x_0, y = y_0, t)}{\partial t} = 2tA^2c^2\frac{c - t}{(t+c)^5}. \tag{3.9}$$

The local maximum in $H(x = x_0, y = y_0, t)$ is when Equation 3.9 is zero. This occurs when $c = t$, and this matches with the intensity function, Equation 3.6.

In most of the applications the length of the scale space of the "blob" was not necessary to determine. To simplify the searching for local maxima and helping with the interlacing of the images, Equation 3.5 can be integrated to eliminate t,

$$\int_0^\infty dt\, H(x,y,t). \tag{3.10}$$

This reduces the comparing of $3^3 - 1 = 26$ neighboring points to just $3^2 - 1 = 8$, to determine the local maximum. In the example, the integration of Equation 3.8 results in,

$$\frac{2A^2c^3}{((x-x_0)^2+(y-y_0)^2)^3}\Big\{\big((x-x_0)^2+(y-y_0)^2-2c\big) + \big((x-x_0)^2+(y-y_0)^2+2c\big)\,\exp\left[-\frac{(x-x_0)^2+(y-y_0)^2}{c}\right]\Big\}. \tag{3.11}$$

This expression is hard to interpret but the maximum is when $x = x_0$ and $y = y_0$.

The integration of H was not in the initial "blob" detection scheme set out by Lindeberg.[61] For comparison, the values of Equation 3.8 and Equation 3.11 are shown in Figure 3.10.

3.4.2 Analysis Program

An extensive program was developed to analyze the large amount of images obtained from the double-slit build-up experiment. Overall there were 6 separate runs with each run having over 65,000 images each. The general scheme is outline in the previous section. The images were all in bitmap form, allowing relatively easy access to the raw image data. Figure 3.11 shows a general outline of the analysis scheme.

First the Bitmaps were loaded into memory. The leading header was stripped and the data was put into an array. A hard cutoff filter was applied to the data. Any pixel with a value of 40 or less was set to zero. This was used to eliminate most of the background noise from the camera. Next $L(x,y,t)$ was calculated, with

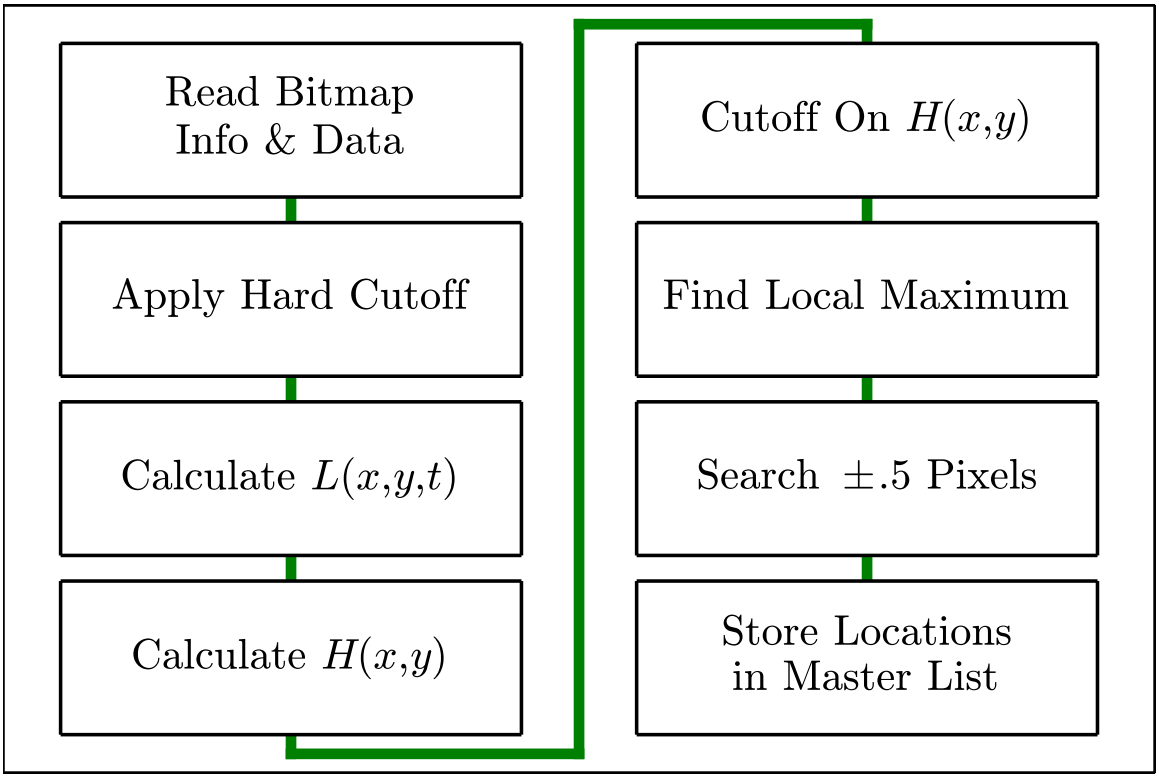

Figure 3.11. Shown above is general outline of the analysis program used to in the double-slit build-up experiment.

x and y centered on each pixel. The value of t ran from 4 to 10, with the limits of the integration in Equation 3.3 running from $x-t...x+t$ and $y-t..y+t$. These limits were chosen to help improve speed while still being able to locating the electron events.

The scale-normalized determinant of the Hessian matrix of $L(x,y,t)$ was then determined. The Bitmaps were 640 pixels wide by 480 pixels tall. To search the entire image, both $L(x,y,t)$ and $H(x,y,t)$ would have to be calculated over 2,150,000 times each. $H(x,y,t)$ was then integrated over t and a cutoff of 1750 was applied. This value was used to prevent a single bright pixel from triggering a "blob" detection. The value was determined by making a completely black bitmap and setting a single pixel to 50. The cutoff prevented the single pixel from being detected.

The value of $H(x,y)$ was then compared to the nearest 8 neighbors to determine if it was a local maximum or not. If it was, the location was saved to a list. After

the entire image was checked the program brought back the original data (before the hard cutoff) and searched $\pm.5$ pixels with a more smaller step size. The integral in Equation 3.3 was calculated again but with larger limits, $x - 2t...x + 2t$ and $y - 2t..y + 2t$, with t ranging from 4 to 10. Then like before $H(x, y, t)$ and $H(x, y)$ were calculated and a local maximum was found. The final locations were then stored in a master list for use later. This method allowed for sub-pixel accuracy to be obtained.

The master list was used by another program to generate images with the background noise eliminated and the electron events uniform. The intermediate images were used to make a movie of the build-up of the double-slit diffraction pattern one electron at a time.* These programs are lengthy and too extensive to explain in detail here, see Appendix C.

To determine the accuracy of the search algorithm, several test were used. First over 100 images were checked manually to ensure the correct location and number of electron events were detected. Next the program was ran on approximately 8300 images. The maximum intensity of the blobs were compared to the maximum intensity of the image itself, see Figure 3.12. The vast majority of the intensity around 41 was determined to be background noise. No electron events were found below the hard cutoff. Applying a larger cutoff, to filter out more of the background noise, would eliminate quite a few electrons events. Instead the cutoff on $H(x, y)$ prevented the large background noise from triggering a detection.

The images could also be used to analysis the resolution of the MCP detector and camera. Figure 3.13 shows a histogram of the electron detection events full width half maximum (FWHM). The detection program was ran on approximately 65,000 images and the electron events locations were recorded. Each image was then fit with a least-squares procedure using a two-dimensional Gaussian centered

*_New Journal of Physics'_ Website; `http://iopscience.iop.org/1367-2630/15/3/033018/media`

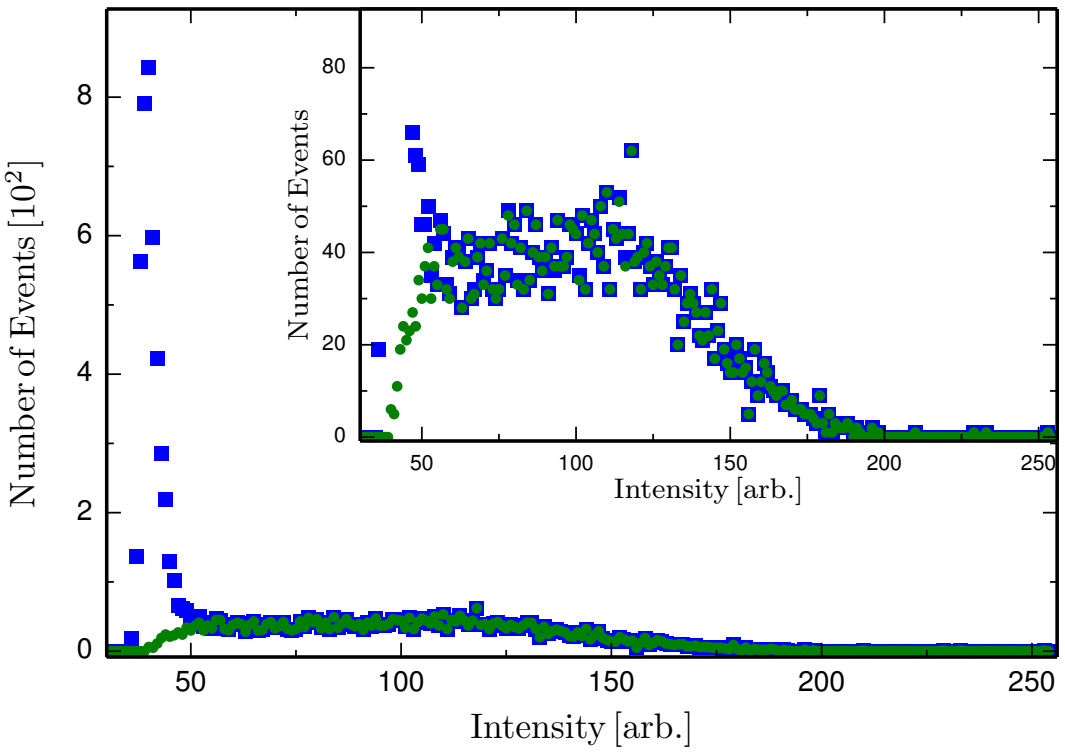

Figure 3.12. Shown above is histogram of the maximum pixel intensity, square (blue) points, for of a set of approximately 8300 images. The circles (green) points are the maximum intesity located at a "blob" detection. The inset shows a 10 times zoomed in section of the main graph. The detection program was able to discriminate the background noise, whose maximum values were centered around 41.

at the previously recorded electron event center. The amplitude of the Gaussian was set to the maximum intensity of the "blob".

From the distribution of the widths, a detector resolution can be calculated. Multiple Gaussian were added together. Each was centered at zero with an amplitude related to it's width. The relation was taken from the histogram shown in Figure 3.13. The resulting curve was then fit to another Gaussian, whose FWHM is the detector resolution. The MCP detector and camera had a resolution of 238.2 $\pm$ 6.6 μm.

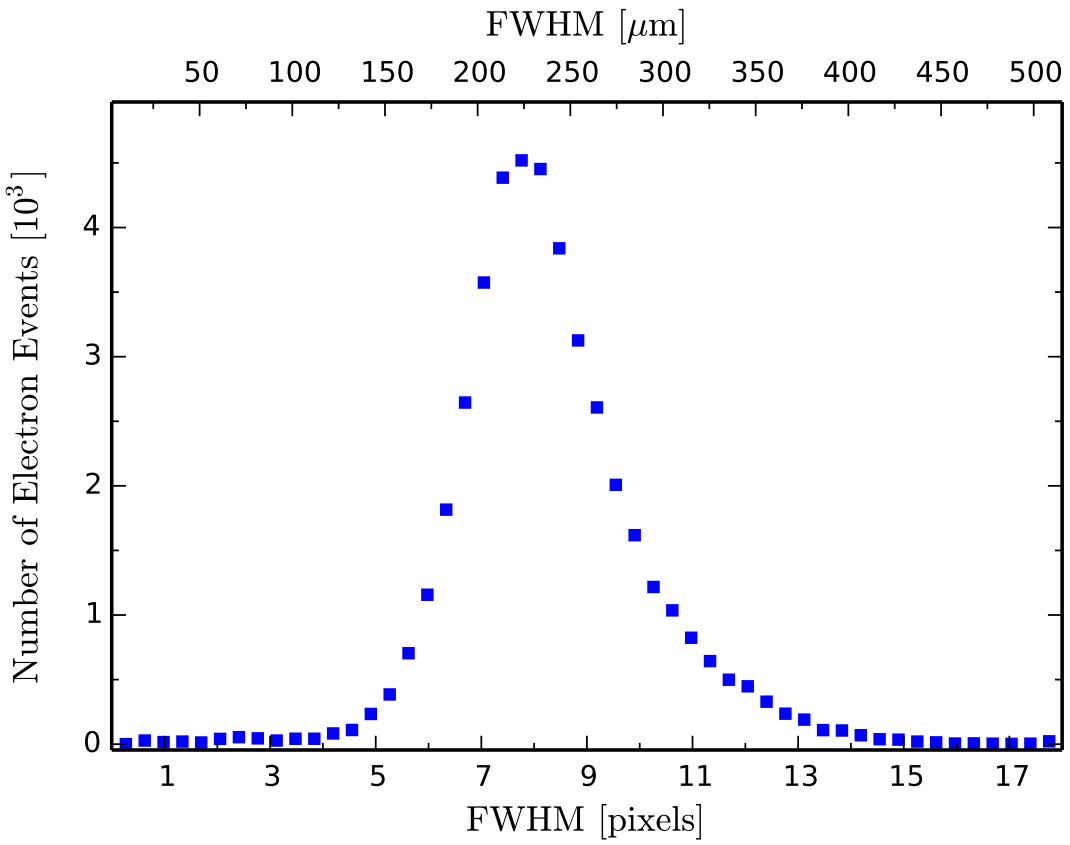

Figure 3.13. Shown above is histogram of the width of the electron events for of a set of approximately 65,000 images. The lower axis shows the FWHM in pixel units, while the upper axis is converted to μm

3.5 Big Move

During the summer of 2010 the University of Nebraska-Lincoln's Physics Department moved into a new building. While the facilities were an upgrade the move required the entire vacuum system to be disassembled and then reassembled at the new building. The timing was unfortunate because the double-slit experiment was only half-way through. The new lab had to be put together from essentially scratch. Figure 3.14 shows the lab after a few things have been moved into it (left) and the current state of the lab today (right). The setup of the new lab, set back the experiments almost a year.

Figure 3.14. Shown above left, is a picture of the lab a few days after moving in. The vacuum system had only been set on the optics table. The picture on the right, shows the current state of the lab

Chapter 4

Double-Slit Diffraction

4.1 Introduction

Richard Feynman described electron diffraction as a phenomenon "which has in it the heart of quantum mechanics. In reality, it contains the *only* mystery."[35] He went on to describe a thought experiment for which he stated "that you should not try to set up" because "the apparatus would have to be made on an impossibly small scale to show the effects we are interested in." He used these effects to help illustrate the phenomena of wave-particle duality, which is a postulate that all particles exhibit both wave and particle properties. The effects he described were: the relations between electron probability distributions from single- and double-slits, and the observation of single particle diffraction.

The general perception is that the electron double-slit experiment has already been performed. This is true in the sense that Jönsson demonstrated diffraction from single, double, and multiple (up to five) micro-slits,[63] but he could not observe single particle diffraction, nor close individual slits. In two separate landmark experiments, individual electron detection was used to produce interference patterns; however, biprisms were used instead of double-slits.[36,64] First, Pozzi recorded the

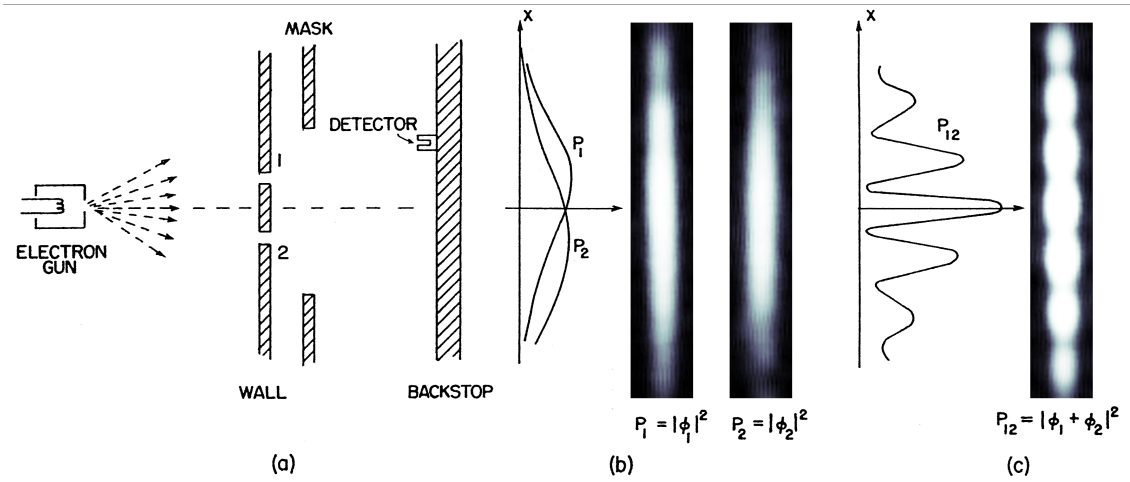

Figure 4.1. An illustration of Feynman's thought experiment is shown above. **(a)** An electron beam passes through a wall with two slits in it. A movable mask is positioned to block the electrons, only allowing the ones traversing through slit 1 (P_1), slit 2 (P_2), or both (P_{12}) to reach the backstop and detector. **(b)**,**(c)** Probability distributions are shown, (Experimental in false-colour intensity) for electrons that pass through a single slit (b), or the double-slit (c). This figure is an adaptation from *Feynman Lectures on Physics*, Volume III, Figure 1-3, with the mask and experimental data added. The experimental data is taken from Figure 4.4.

interference patterns at varying electron beam densities. Then, Tonomura recorded the positions of individual electron detection events and used them to produce the well known build-up of an interference pattern. It is interesting to point out that the build up of a double-slit diffraction pattern has been called "The most beautiful experiment in physics," [65,66] while the build-up for a true double-slit had never been reported.

More recently, electron diffraction was demonstrated with single- and double-slits using Focused Ion Beam (FIB) milled nano-slits.[33,67] In addition, one single slit in a double-slit was closed by FIB induced deposition.[68] This process is not reversible, so observation of the electron probability distribution through both single-slits could not be done. Also, using a fast-readout pixel detector, electrons were recorded one at a time and stacked into a final diffraction pattern,[69] but intermediate spatial patterns were not reported.

Feynman's thought experiment is summarized in Figure 4.1. The thought experiment contained two parts. The first involved observing probability distributions in three scenarios: electrons traveling through slit 1 with slit 2 closed (P_1); electrons traveling through slit 2 with slit 1 closed (P_2); and electrons traveling through both slits (P_{12}). These scenarios illustrate the quantum mechanical superposition principle, i.e., the wave properties, and can be demonstrated with control of the slits (Figure 4.4). The second part of the thought experiment was the observation of individual electrons associated with detection "clicks". This illustrates that a quantum mechanical electron wave can not be thought of as comprising multiple electrons, i.e., the particle properties, which can be demonstrated with the build-up of the diffraction pattern (Figure 4.5).

4.2 Setup

The experimental setup is explained in detail in Chapter 3 and illustrated in Figure 4.2. An electron beam with energy of 600 eV, which corresponds to a de Broglie wavelength of approximately 50 pm, was generated with a thermionic tungsten filament and several electrostatic lenses. The beam was collimated with a slit of 2 μm width and 10 μm height. The resulting patterns were magnified by an electrostatic quadrupole lens and imaged on a two-dimensional microchannel plate and phosphorus screen detector, then recorded with a camera.

Two methods were used to analyze the images taken by the camera, see Section 3.3.2. To investigate the probability distributions (part 1 of Feynman's thought experiment), the images were summed up by adding each images's intensity, then normalized. This resulted in a false colour probability distribution (Figure 4.4).
To study the build-up of the diffraction pattern (part 2 of Feynman's thought experiment), each electron was localized using the "blob" detection scheme laid out

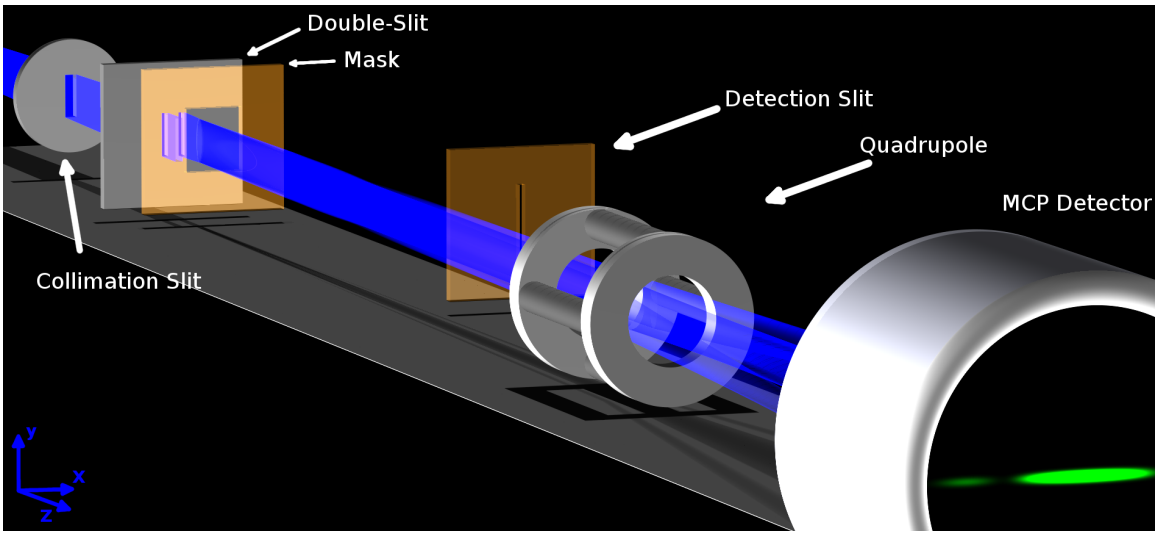

Figure 4.2. Illustration of the double-slit experiment. Electrons pass through a collimated slit. The resulting patterns from the double-slit and mask were either sampled be a movable detection slit, or magnified by an electrostatic quadropole lens and imaged on a two-dimensional microchannel plate and phosphorus screen detector. The mask was movable and was used to block none, one, or both of the slits of the double slit.

in detail in Section 3.4. The "blobs" were compiled together to form the electron diffraction patterns (Figure 4.5).

The double-slit consisted of two 62 nm-wide slits separated center-to-center by 272 nm. The individual slits where approximately 4 μm tall with a 150 nm support structure midway along it's height. Figure 4.3 inset (b) shows an electron micrograph of the double-slit.

A 4.5 μm wide by approximately 20 μm tall mask was placed 240 μm away from the double-slit, see Figure 4.3 inset (a). The mask was held securely in a frame that could slide back and forth and was controlled by a piezoelectric actuator (Thorlabs' AE0505D16F). The actuator allowed for nm precision movement but the exact position was only inferable from the voltage applied to it.

The double-slit and mask were made by FIB milling into 100 nm-thin silicon-nitride membrane windows. The FIB milling was performed on a 30 keV Ga^+ system (FEI Strata 200xp). After milling, each membrane was coated with approx-

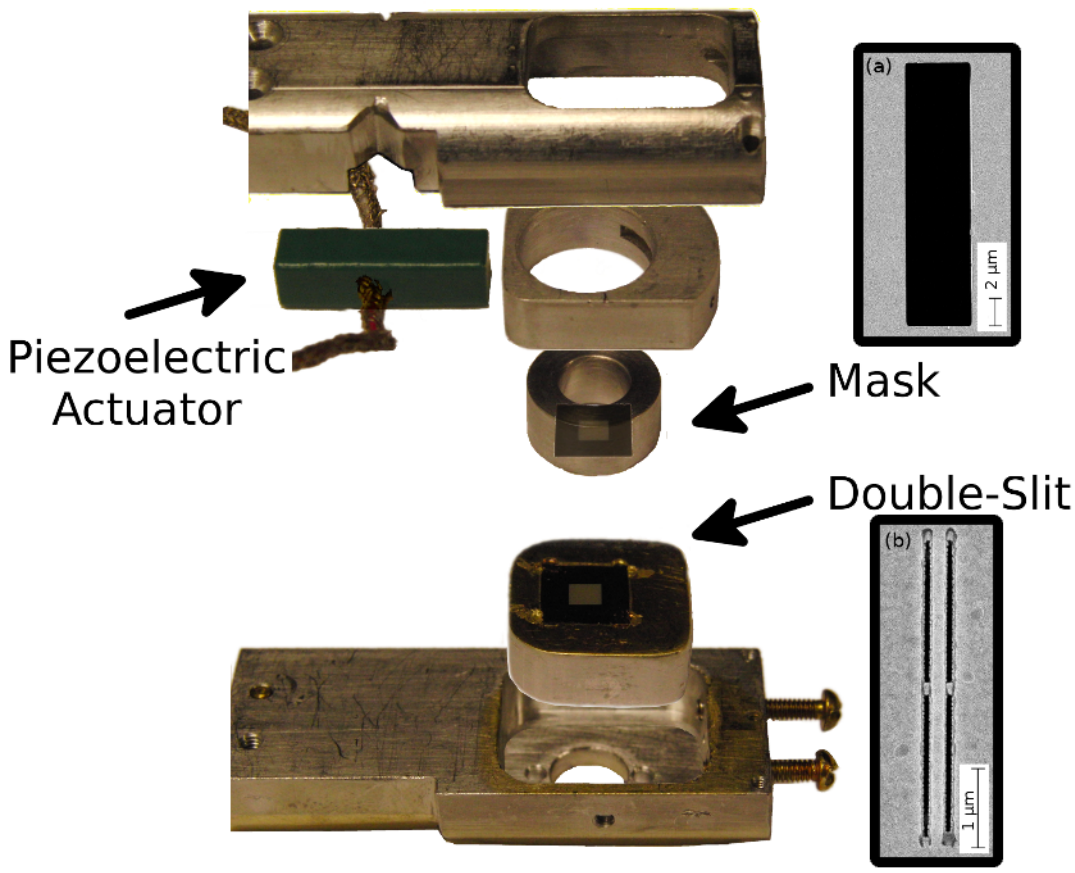

Figure 4.3. Shown above is an expanded view of the mount used to hold the double-slit and mask. The lower section allowed for motion of the double-slit, for initial alignment. The top section allowed the piezoelectric actuator to slid the mask from left to right. The insets show electron micrographs of the mask (a) and double-slit (b). The double-slit and mask are located in the center of the square transluent membrane.

imately 2 nm of gold. They were both held together (see Figure 4.3) in an aluminum mount that is attracted horizontally to the "wobble-flange" and linear feedthrough, see Section 3.2.6.

4.3 Results

The movable mask was placed behind the double-slit, see Figure 4.2. The mask was moved from one side to the other (Figure 4.4 top to bottom). Initially the majority of the electrons are blocked. As the mask is moved, slit 1 becomes partially, then

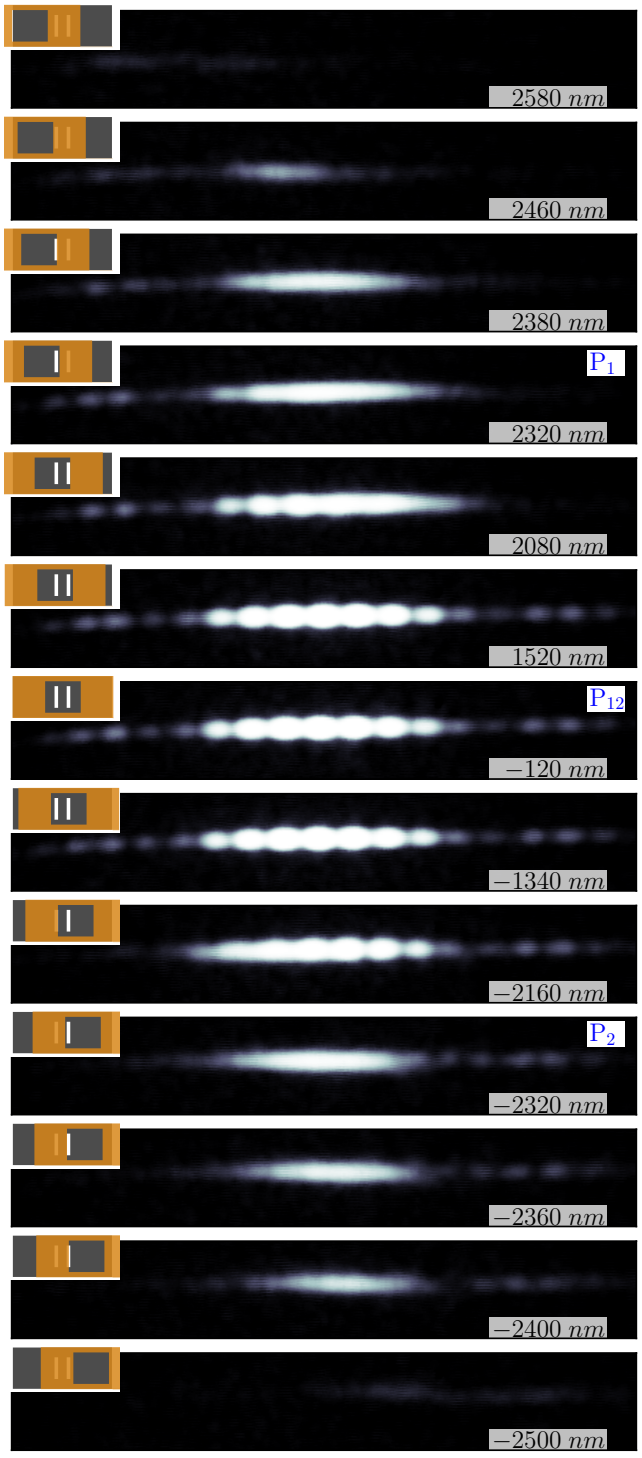

Figure 4.4. A mask is moved over a double-slit (inset) and the resulting probability distributions are shown. The mask allows the blocking of one slit, both slits, or neither slit. The labeled dimensions are the positions of the center of the mask. P_1, P_2, and P_{12} are the probability distributions shown in Figure 4.1.

fully open. When one slit is open, single-slit diffraction can be observed (P_1 in Figure 4.4). Feynman indicates this as the solid black curve P_1 in Figure 4.1(b), which is just the central order of the single-slit diffraction pattern. Because of the finite separation of the mask and double-slit, weak double-slit diffraction can be seen in the negative first order of the single-slit diffraction pattern (see left edge of P_1 in Fig. 4.4).

As the mask is moved further, more electrons can travel through both slits, changing the pattern from single-slit to double-slit diffraction. When the mask is centered on the double-slit, both slits are completely open and full double-slit diffraction can be observed (P_{12} in Fig. 4.4). In this position, interaction between the mask and the diffracting electrons is negligible. The edges of the mask are 2250 nm away from the center and would only affect diffraction orders greater than the 50^{th}. The mask is then moved further and the reverse happens; double-slit diffraction changes back to single-slit diffraction (P_2 in Figure 4.4). Now, the single-slit diffraction pattern has a weak contribution of double-slit diffraction in its positive first order (see right edge of P_2 in Fig. 4.4).

Electron build-up patterns were recorded with the mask centered on the double-slit. The electron source's intensity was reduced so that the electron detection rate in the pattern was about 1 Hz. At this rate and kinetic energy, the average distance between consecutive electrons was 2.3×10^6 meters. This ensures that only one electron is present in the 1 meter long system at any one time, thus eliminating electron-electron interactions. The electrostatic quadrupole lens was set to zoom in on the central five diffraction orders. In Figure 4.5 the build-up of the diffraction pattern is shown. In Figure 4.5(a)-(c), the electron hits appear to be completely random and only after many electrons are accumulated can a pattern be discerned, Figure 4.5(d). In Figure 4.5(e) the pattern is clearly visible. The final build-up of the pattern took about 2 hours. A complete build-up of the diffraction pattern

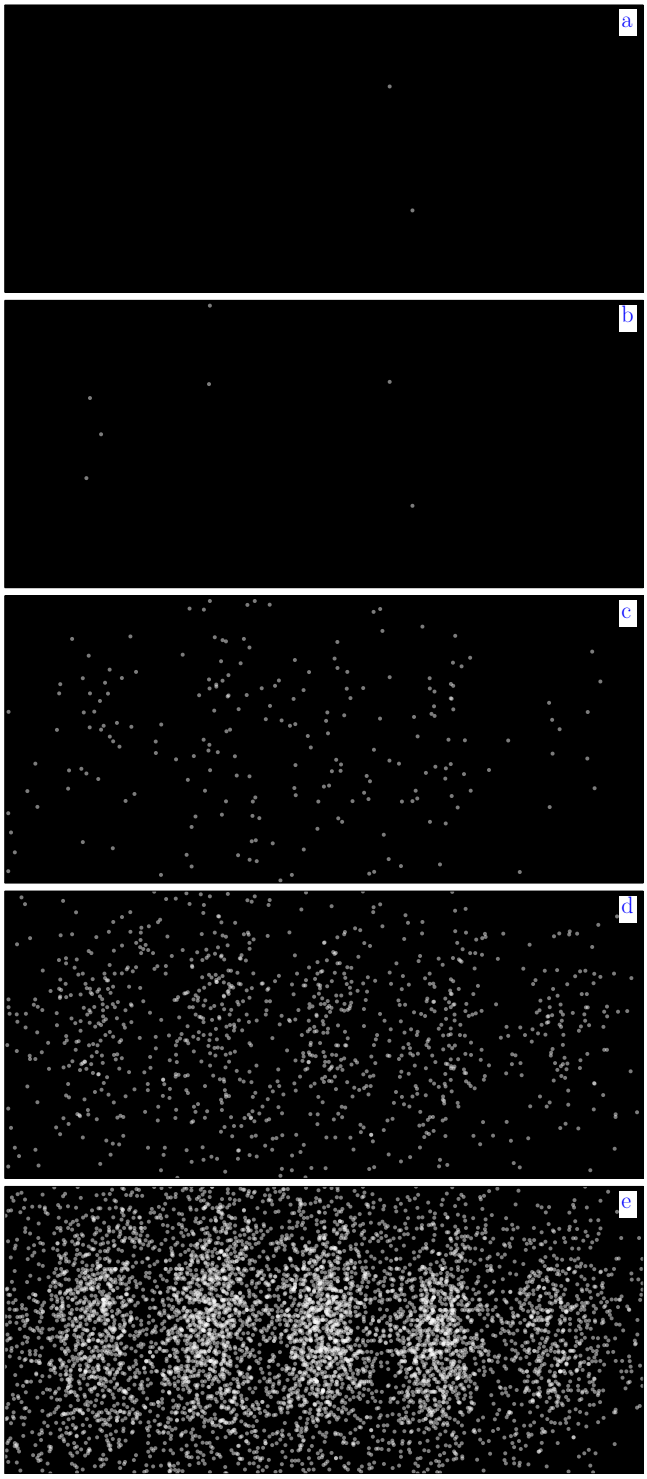

Figure 4.5. Buildup of electron diffraction. "Blobs" indicate the locations of detected electrons. Shown are intermediate build-up patterns from the central five orders of the diffraction pattern (P_{12}) magnified from Figure 4.4, with 2, 7, 209, 1004, and 6235 electrons (a-e).

was generated from all the intermediate images and is available at *New Journal of Physics'* website.*

4.4 Measurements and Fits

Scanning electron microscope (SEM) images were taken on an electron beam lithography system (Zeiss Supra 40). The images are shown in Figure 4.3 inset (a) and (b). The dimensions obtained using the SEM images are shown in Table 4.1

The detection slit (see Figure 4.2) allowed for the acquisition of diffraction patterns with resolution of approximately 5 μm, see Section 3.2.3. This data was fit with a least-squares procedure using a modified version of Equation 2.6,

$$I = A_0 + A\left[\frac{\sin(\alpha x)}{\alpha x}\right]^2 \left[1 + V\cos(2\beta x)\right], \tag{4.1}$$

where $\alpha = \frac{\pi a}{\lambda_{dB} D}$ and $\beta = \frac{\pi d}{\lambda_{dB} D}$. The de Broglie wavelength (λ_{dB}) was 50.07 $\pm$ 0.13 pm and the propagation distance (D) was 240 $\pm$ 5 mm. A_0, A, a, d, and V are fit parameters with a representing the slit width, d the center-to-center separation, and V the visibility parameter, $V = (I_{\max} - I_{\min})/(I_{\max} + I_{\min})$, of the diffraction pattern. A normalized fit of the data, along with the scaled data, is shown in figure 4.6(a). The width and separation dimensions found are listed in Table 4.1. The visibility parameter was 0.819 $\pm$ .032.

One drawback of using the detection slit was the low count rate. This caused long acquisition times (approximately 130 secconds per point, more than 3 hours total) and limited the spatial range of the diffraction pattern that was able to be sampled. Drifts in the electron emission current could change the relative count rate as the pattern was acquired (left to right). This could be an explanation why

**New Journal of Physics'* Website; `http://iopscience.iop.org/1367-2630/15/3/033018/media`

	a (nm)	d (nm)	$\frac{d}{a}$	Mask (nm)
SEM	64.6	282.7	4.38	4680
Detection Slit	69.9 ± 3.3	272.6 ± 11.3	$3.90 \pm .09$	_____
MCP Detector	62.3 ± 4.0	272.6 ± 17.6	$4.38 \pm .01$	_____
Simulation	62.3	272.6	4.38	4520

Table 4.1. Double slit specifications. The dimensions found using different measurement techniques and the dimensions used in the quantum mechanical simulation. The SEM dimensions were taken from the images shown in Figure 4.3 insets, while the Detection Slit's and MCP Detector's dimensions were taken from the fit of the date obtained from the respective detector. The width of each of the slits in the double-slit is a and d is the separation of the slits. The majority of the errors in the width and separation come from the uncertainty in the wavelength, propagation distance, and fitting. The error in the ratio is from the uncertainty in the fitting.

the diffraction pattern in Figure 4.6(a) shows an asymmetry between the left and right sides. These effects can cause the a parameter to be an overestimate of the actual slit width, but should not affect the d parameter because it is only dependent on the location of the peaks and not the heights.

The same fitting procedure, using Equation 4.1, was used on the data acquired from the MCP detector (see Figure 4.4). Since the quadropole only magnifies the horizontal dimension the vertical dimension was summed up to perform the fit in one dimension, see Figure 4.6(b). Now the fitting parameters a and d will consist of a magnification factor as well as the slit width and separation. To determine the magnification factor both d parameters (detection slit and MCP detector) were set equal to each other. For the voltages used during the acquisition of data in Figure 4.4 (and Figure 4.6(b)) the magnification factor was 16.58 ± 0.90. This allows the slit widths and separation to be determined, they are given in Table 4.1. The visibility parameter was $0.477 \pm .0034$.

The main reason for the drop in visibility between the detection slit and MCP detector (Figure 4.6(a) and b) was the increase in detection resolution. The MCP detector and camera setup had a resolution of 238.2 ± 6.6 μm, see Section 3.4.2.

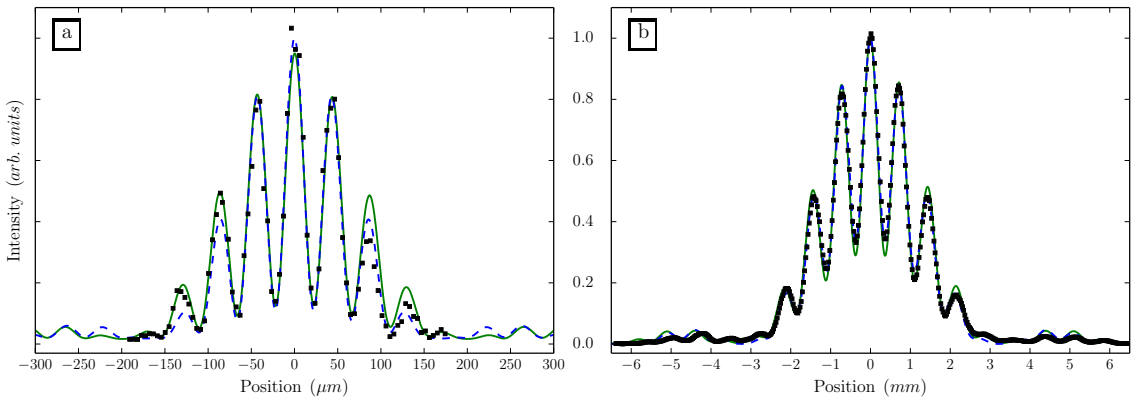

Figure 4.6. Diffraction recorded at the detection slit (a) and the MCP detector (b). The squares (black) represent the experimental data, the solid line (green) represent the results of the path integral model, and the dashed line (blue) represents the fit from Equation 4.1. The diffraction pattern was magnified by the electrostatic quadropole lens when it was recorded by the MCP detector.

All three methods of determining the double-slit dimensions gave slightly different values. One parameter that could be determined independently in each situation was the ratio of $\frac{d}{a}$ (see Table 4.1). This values is independent from the calibration of the SEM or the magnification factor. The SEM and MCP detector both obtained the same ratio. There is a only a 3.6% difference between the individual measurements.

4.5 Quantum Mechanical Simulation

To compare with experimental results, a quantum mechanical numerical simulation was produced. The theoretical description is discusses in detail in Section 2.3 and 2.4. The wave function was propagated from the plane of the collimation slit to the double-slit, mask and then to the detection plane. At the collimation slit multiple incoherent sources were propagated through the system. The resulting probability distribution at the detection plane represents what the detection slit samples.

At the collimation slit, double-slit, and mask an image charge potential was

	Image Charge	Random Potential			
		Width		Amplitude	
	q_{eff}	Mean	FWHM	Mean	FWHM
Barwick et al.[33]	$0.13e$	250 nm	250 nm	0 eV	0.350 eV
Current Simulation	$0.13e$	250 nm	250 nm	0 eV	0.225 eV

Table 4.2. Comparison of simulation parameters between current simulation and the simulation done by Barwick et al.[33]

added. Additionally at the double-slit a random potential was added. The values describing the interaction were identical to the ones used by Barwick et al. except the full width half max of the amplitude of the random potential.[33] The values are summarized in Table 4.2. The physical system that motivates the random potential was based on contact potentials. The metal coating that was used on the gratings by Barwick et al. was different than the coating used during this current experiment. This difference warranted small changes in the amplitude of the random potential to accurately model our experimental data. These values were not obtained through fitting, but merely changed until an acceptable agreement was obtained with the contrast of the experimental data, see Figure 4.6

The parameters for the double slit used in the simulations are listed in Table 4.1. The diffraction pattern calculated at the detection slit is shown in Figure 4.6(a) with an offset to account for background.

To simulate the pattern obtained at the MCP detector, the quadropole and detector needed to be accounted for. To do this the magnification factor, determined in section 4.4, was multiplied with the value of the x coordinate and then the probability distribution was convoluted with a Gaussian, with a width of the MCP detector's resolution, see Section 3.4.2. The probability distribution calculated at the MCP detector is shown in Figure 4.6(b). There is excellent agreement between the simulation and the experiment. The small asymmetry between the right and left

orders is gone because with this detection method the pattern is built up all at ounce and variation in the initial beam's intensity will not affect each side differently. There is a slight discrepancy on the positions of the leftmost orders. This is most likely due to the interaction of the quadropole. That section of the pattern was not magnified uniformly as the rest of the pattern was.

To represent the mask movement and fully reproduce the patterns on the MCP detector, the simulation was performed multiple times with the mask in a different position. Then the probability distribution was multiplied by a Gaussian in the y direction. The distribution was then made into a false colour plot in the exact same manner as the data was. A transformation function was used to highlight outer orders by over saturating the central orders

$$A_{out}(x, y) = 1 - \exp\left(-20 A_{in}(x, y)\right), \tag{4.2}$$

where A_{in} and A_{out} are the before and after probability distributions respectively and both have values between 0 and 1. The value of 20 was chosen for visual appearance.

The different positions of the mask are shown in Figure 4.7, experimental left and theory right. For comparison purposes the theoretical distributions were formatted identically to the experimental. The agreement between theory and experiment is excellent, with a few exceptions. As mentions before the left edge of the experimental data is moved inwards slightly. At 2080 nm the central 7 orders are almost fully visible in the simulation as compared to the experiment data showing only the left side. This is probably due to an inaccuracy in the mask position, which was inferred from the piezoelectric transducer voltage. The mask mount can stick until the piezoelectric transducer generates enough force to unstick it. This extra force causes the voltage reading to misrepresent the position.

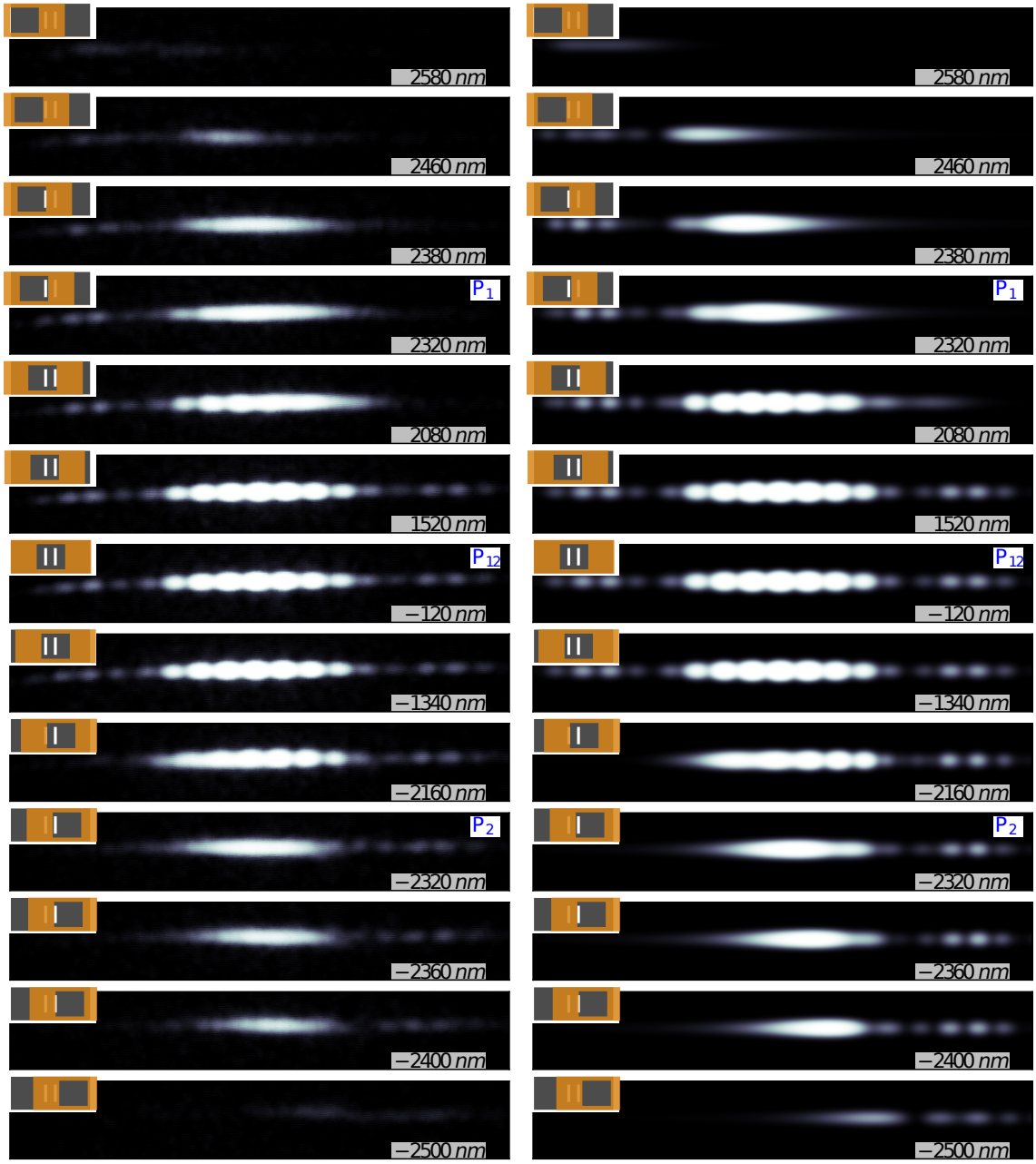

Figure 4.7. Mask movement for experiment and the quantum mechanical simulation are shown left and right respectively. A mask is moved over a double-slit (inset) and the resulting probability distributions are shown. The labeled dimensions are the positions of the center of the mask.

4.6 Conclusion

These results show a full realization of Feynman's thought experiment and illustrate key features of quantum mechanics: interference and the wave-particle duality

of matter. By controlling the transmission through the individual slits of a double-slit, the diffraction patterns from slit 1 (P_1), slit 2 (P_2), and both (P_{12}) were observed, thus observing the wave properties of electrons. Also, by recording single electron detection events diffracting through a double-slit a diffraction pattern was built, thus observing the particle properties of electrons.

Overall the path integral simulation represents the experimental data, which in turn is in agreement with quantum mechanics. Moving the mask to block one of the slits does not give anything unexpected.

Chapter 5

Talbot-Lau Interferometer

5.1 Introduction

In the past decades matter-wave interferometers have been used to demonstrate fundamental quantum phenomena and perform precision measurements. Applications include accelerometers,[70,71] gravitational measurements,[72,73] studies of decoherence,[43] and the measurement of fundamental constants.[73,74] A lot of work has been carried out with atomic, molecular, or neutron beam interferometry.[58,75,76] Electron beam interferometers have made use of the electron's charge to demonstrate the Aharonov-Bohm effect,[77] to visualize super-conducting vortices, and observe degeneracy in free space.[78] It is also well-known that electron interferometers share with their electron microscope counterparts the requirement that external electromagnetic fields need to be carefully shielded. In Tonomura's work, nearby commuter trains caused instability, while in the work at Tubingen a radio station reduced interference contrast. In view of this, it appears natural to investigate using this sensitivity to our advantage.

Several different interferometer designs exist. The present discussion is limited to free electron beam interferometers and does not include the exciting field

of mesoscopic or solid state electron interferometry. Far-field interferometers using gratings[34] and crystals[18] as well as biprism interferometers[79,80] have been demonstrated. Larger interferometers are usually more sensitive to fields, but also have to meet stringent mechanical demands. The recent observation of Talbot[81] and Lau[82] interference fringe patterns using two gratings, motivated the construction of a near-field three-grating Talbot-Lau interferometer (TLI). A near-field interferometer with crystals would require extremely small crystal separations. Biprism interferometers use small electron acceptance angles. The promise that a TLI offers is mechanical stability in a small design with a large electron beam acceptance angle.

The rest of this chapter covers, the construction and demonstration of a near-field three-grating TLI for electrons. A TLI consists of three identical gratings. The first two gratings produced fringes downstream utilizing the Lau effect.[58] The third grating was added and used as a mask to sample these fringes.

5.2 Setup

The experimental setup is illustrated in Figure 5.1 and explained in detail in Chapter 3. An electron beam was first collimated by a 5 μm wide by 100 μm tall slit. For further collimation, one of two collimation slits could be used. Either a 2 μm wide by 10 μm tall slit or a 30 μm wide by 10 μm tall could be used. The collimated beam then passed through the TLI. The total electron transmission through the interferometer was counted on a two dimensional microchannel plate (MCP) and phosphorus screen detector. An electrostatic quadrupole lens was used to spatially magnify the electron transmission to prevent saturation of the MCP detector.

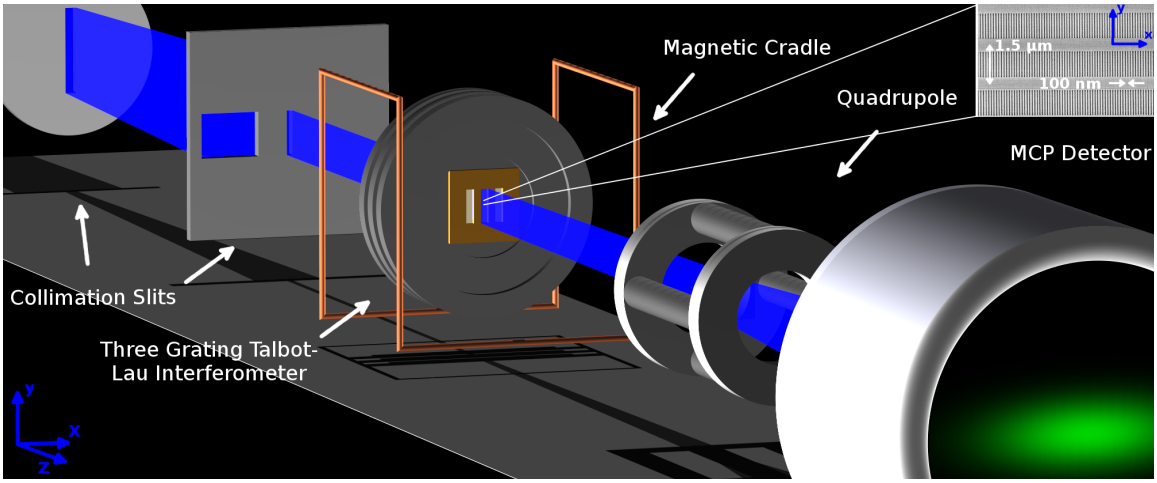

Figure 5.1. Illustration of the Talbot-Lau experiment. An electron beam is first collimated by two slits, then it is incident on the three grating Talbot-Lau interferometer. The throughput of the interferometer is counted by a microchannel plate detector. To apply magnetic and electric fields, the interferometer was placed in a cradle with current carrying wires and located between two charged plates (not shown)

5.3 Talbot-Lau Interferometer

5.3.1 Design

The TLI consists of three identical sections, see Figure 5.2. Each section consisted of a 30 mm diameter aluminum body with an 8 mm hole in the center, see Appendix D for a technical drawing. Attached to each section is a metal-coated silicon-nitride 100 nm period transmissive grating, see Figure 5.1 inset, which were made by Savas and Smith at the MIT NanoStructures laboratory using achromatic interferometric lithography.[83,84] The distance between adjacent gratings is 3.06 ± .01 mm.

5.3.2 Alignment

Rotational alignment between all gratings is necessary to observe contrast. If the third grating is rotated about the the z-axis, the top and bottom segments of the grating will sample different patterns. If the top and bottom are miss-aligned by 50

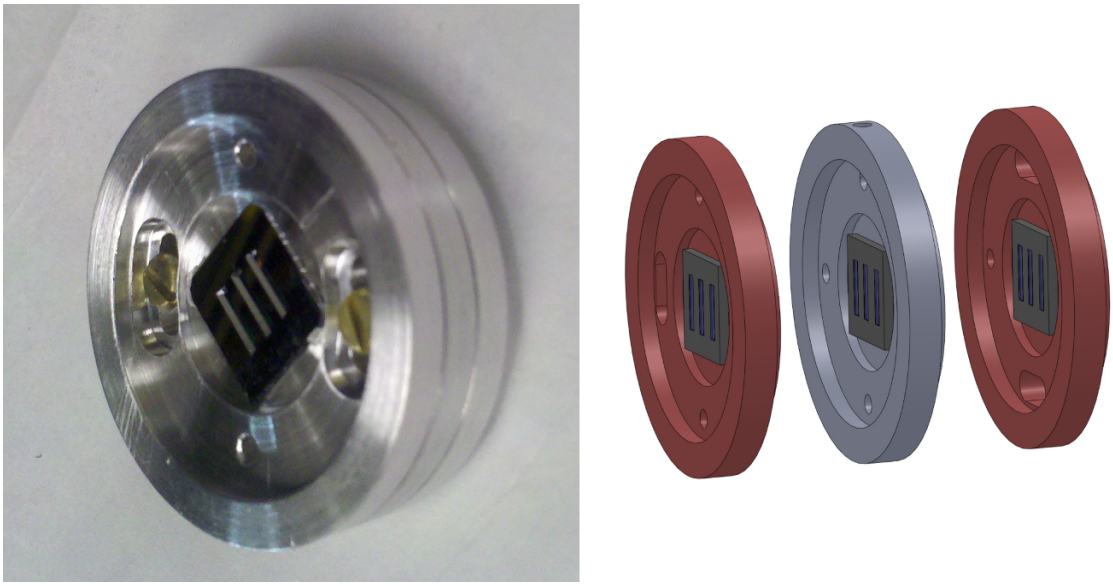

Figure 5.2. Shown above it the three grating Talbot-Lau Interferometer. It consists of three identical sections, each having a metal-coated silicon-nitride 100 nm period transmissive grating attached. Shown left is the assembled TLI, while shown right is an expanded CAD drawing of the TLI.

nm then they will cancel each other, resulting in diminished contrast of the signal.

A HeNe laser was sent through the interferometer in the opposite direction of the electron beam path, see Figure 5.3. The laser diffracted off of the 1.5 μm grating support structure, see Figure 5.1 inset. Due to the separation distances and the size of the gratings the $\pm 1^{st}$ orders of the first grating could not be used. Instead an alternate path was used to determine the rotational position of the first grating. The 13 resulting dots were allowed to propagate until the outer 4 were separated from the inner 5 by approximately 1 meter. Then they were aligned in a straight line to within approximately 1 mm. This gives a rotational alignment of 10^{-3} rad.

5.3.3 Mounting

The TLI was mounted from the top on the two-dimensional translation mount in the "sample region", see Section 3.2.6. The translation mount allowed for movement in the x and y directions. This allowed the TLI to be completely removed

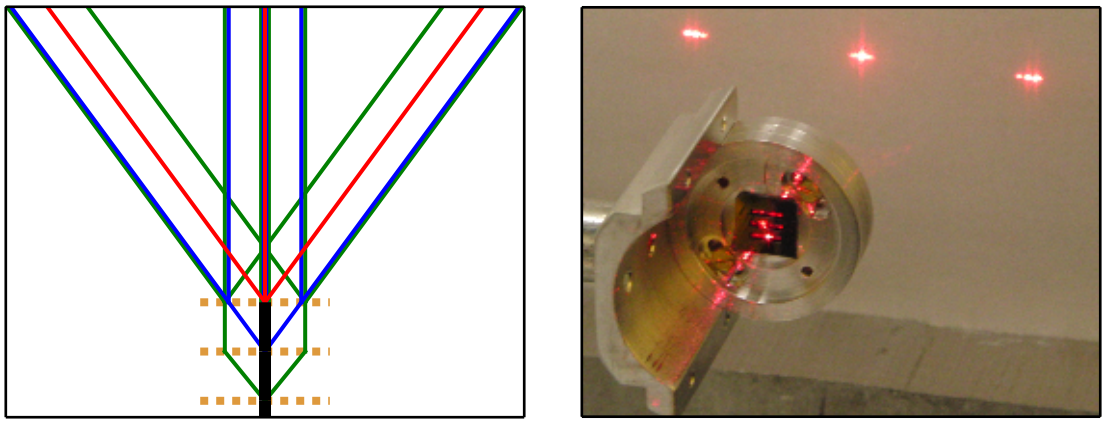

Figure 5.3. Rotational alignment was done by diffracting a HeNe laser beam off the grating support structure. The left figure shows the laser beam paths and from which grating they diffract from. The image on the right shows the resulting 13 spots that were used for alignment. Only 9 are visible, the rest are overlapping.

from the beam path, see Figure 5.4, and be positioned to test different portions of the gratings.

5.4 Magnetic and Electric Fields

To apply magnetic and electric fields the TLI was placed in a cradle, see Figure 5.5. The cradle had a wire arranged around a cube's edges as shown in Figure 5.1. This arrangement produces a maximum magnetic field,

$$B = \frac{2}{\sqrt{3}} \frac{\mu_0 I}{\pi w}, \tag{5.1}$$

at the center of the structure in the vertical direction with no field in the horizontal directions. Here μ_0 is the permeability of free space, I is the current through the wires, and w (54 mm) is the length of the cube's edges that the wires are arranged on. The cradle also had a pair of individually addressable deflection plates. The plates were 46 mm long by 28 mm tall and separated by 50.8 mm. The cradle was built in the University of Nebraska-Lincoln, Department of Physics, student

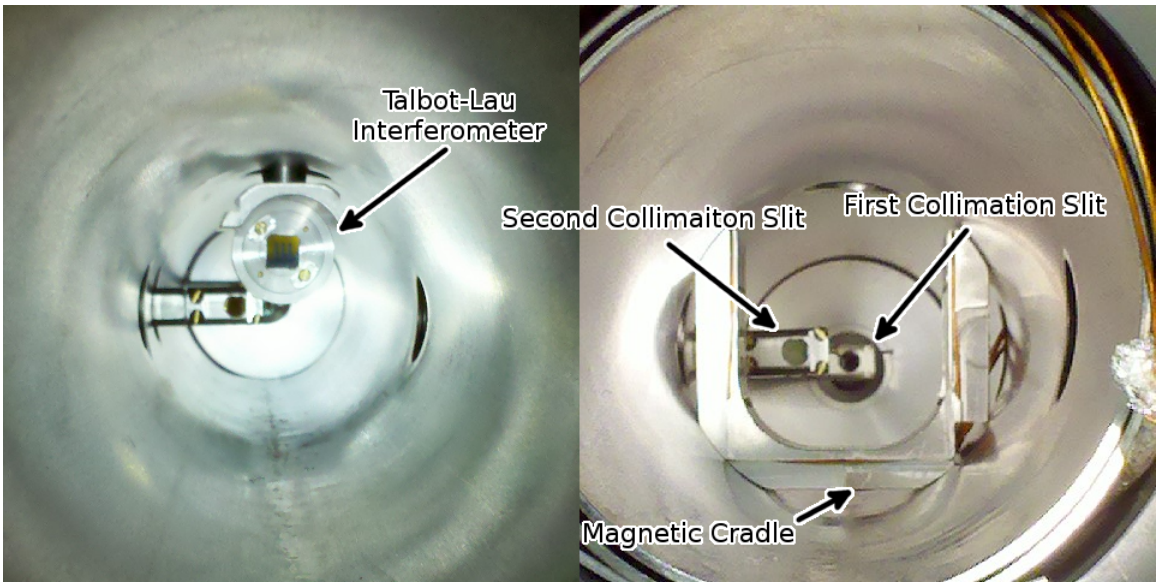

Figure 5.4. Show above left is the TLI mounted inside the vacuum system. The TLI was attached from above. The two dimensional translation mount allowed motion in the plane of the images. The first and second collimation slits can be seen behind the TLI. The Right image shows the magnetic cradle installed in the vacuum chamber. The translation mount allowed the TLI to be placed in the center of the magnetic cradle.

machine shop, see Appendix D for a design drawing.

5.5 Results

The total electron throughput of the TLI was recorded as a function of current, see Figure 5.6. The theoretical magnetic field at the center of the cradle, using Equation 5.1, is shown along the top axis, while the actual current through the wire is shown along the bottom. The electron counts were summed from multiple sweeps of the magnetic field. The Fourier transform of the data yields a period of 77 mA or 0.66 μT.

The classical deflection of a particle with charge q in a uniform magnetic field B, requiring that it pass through two aligned slits (along x) separated by L (along z), yields a transverse displacement s (along x) measured a distance L (along z)

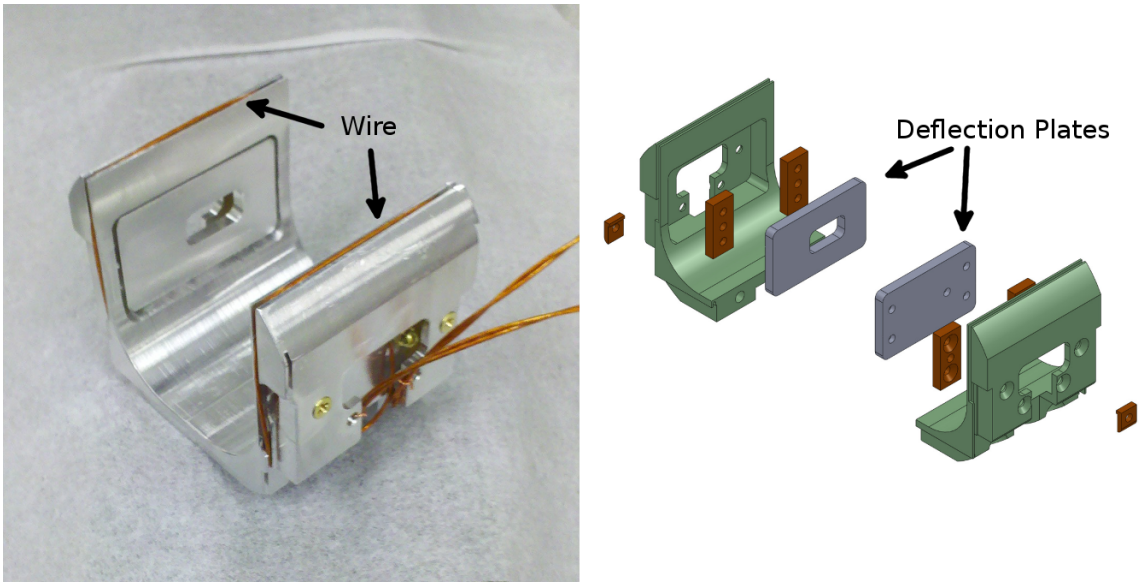

Figure 5.5. Shown above is the electric and magnetic cradle. The cradle had two addressable deflection plates and a coil of wire to run current through. The TLI was held in the center of cradle, where the electric and magnetic field were the largest. Shown left is the assembled and right is an expanded CAD drawing of the magnetic cradle.

from the second slit,

$$s = \frac{qBL^2}{mv}. \tag{5.2}$$

Here m is the mass of the particle and v is the velocity of the particle. Alternatively, from quantum mechanics, the phase difference between different paths can be given by[85]

$$\Delta\phi = \frac{q}{\hbar}\int \vec{B}\cdot d\vec{A} = \frac{q}{\hbar}BLnd, \tag{5.3}$$

where n is an integer representing the number of grating openings that the paths are separated by, and n also equals the multiple of half the Talbot length (L_T) the gratings are separated by ($L = nL_T/2$). Here, $L_T = 2d^2/\lambda_{dB}$, where d is the period of the grating and λ_{dB} is the de Broglie wavelength.[57] Both Equation 5.2 and 5.3

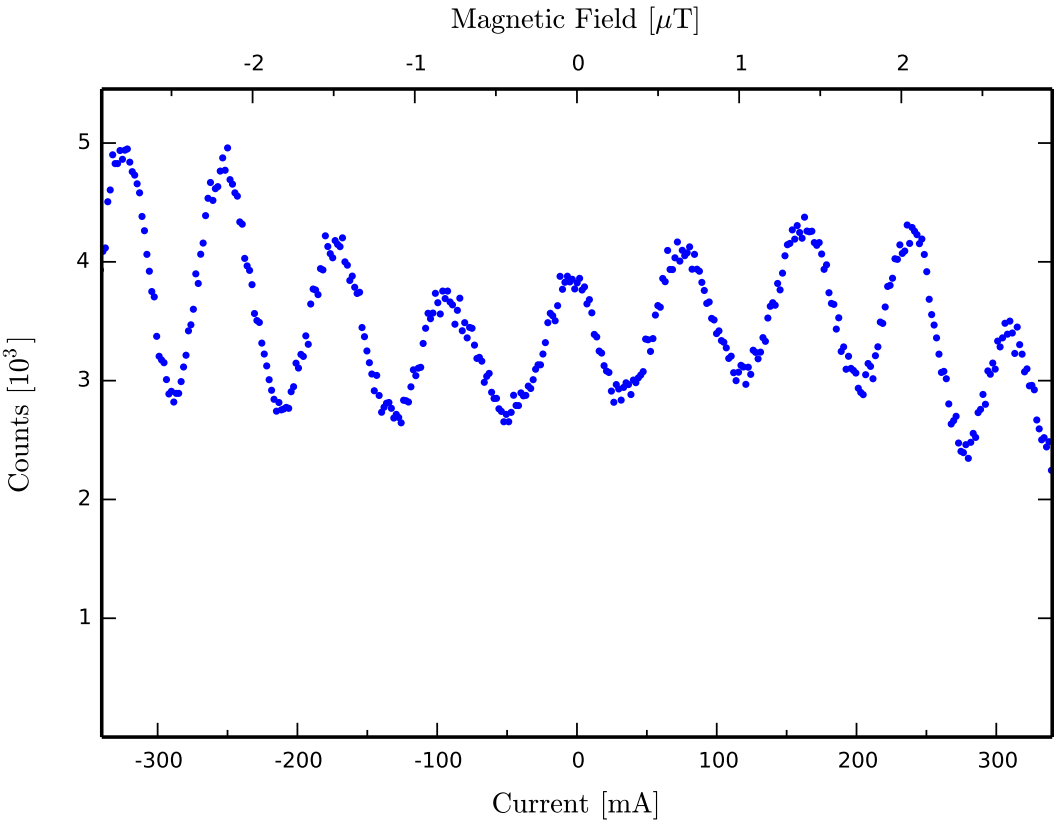

Figure 5.6. Electron throughput of the Talbot-Lau interferometer with varying magnetic field. The current through the magnetic cradle was scanned from a negative to positive value. The magnetic field is shown along the top axis.

can be solved for B with a displacement of d or a 2π phase difference, respectively, giving

$$B = \frac{2\pi\hbar}{q}\frac{1}{Lnd} = \frac{mvd}{qL^2}. \tag{5.4}$$

In Figure 5.6 the energy used was 10 keV. The magnetic field needed to produce successive maxima in the count rate according to Equation 5.4 is 3.6 μT. A direct measurement at the location of the TLI gave a field approximately 20% larger than the field calculated using Equation 5.1. This was caused by the placement of the TLI inside the cradle and the effect of the magnetic shielding of the vacuum chamber around the cradle. The origin of the large discrepancy of a factor of approxi-

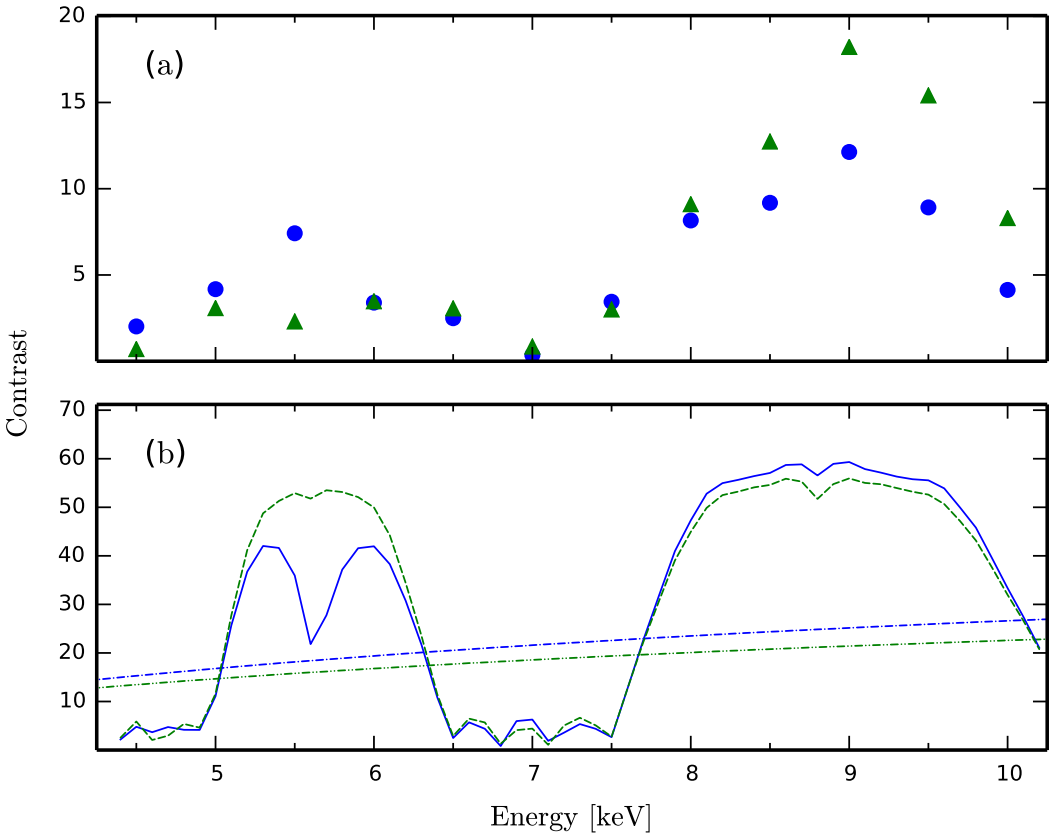

Figure 5.7. The experimental and theoretical contrasts of the Talbot-Lau interferometer are compared as a function of energy. **(a)** Experimental results using a 2 and 30 μm second collimation slit are shown using circles (blue) and triangles (green) respectively. **(b)** The solid and dashed line represent a Quantum mechanical simulation with 2 and 30 μm second collimation slit. Similarly classical theoretical contrasts are shown using dashed-dotted and dashed-dotted-dotted lines.

mately 5.5 from the theoretical period to the observed period is currently unknown.

One key difference between a TLI and a classical Moiré deflectometer[70] is the energy dependence. A Moiré deflectometer's contrast has little energy dependence, whereas in a TLI there is a strong contrast dependence on energy. For the current setup, the maximum contrast occurs at lengths around multiples of half the Talbot length.[58] The length was fixed at 3.06 mm and the electron gun could easily reach energies from 4.5 to 10 KeV. This allowed us to probe two different contrast maxima, at 8.8 and 5.6 keV or de Broglie wavelengths of 13.1 pm and 16.3 pm respectively. The contrast, $(S_{max} - S_{min})/(S_{max} + S_{min})$, is plotted as a function of

energy in Figure 5.7(a). The maxima are clearly seen in the experimental data.

Another feature of the TLI is that the contrast should be unaffected by the beam width. That is, a TLI can tolerate a large transverse momentum spread in the beam.[58] This prediction is explored by comparing data obtained with a 2 μm collimation slit and data with a 30 μm collimation slit, see Figure 5.7(a). Our data shows that the contrast is somewhat affected by the larger larger momentum spread, but still clearly shows the maxima. In theory the TLI could be used without collimation slits. This is not possible in our setup because the non-perfect rotational alignment of the three gratings would cause different vertical sections of the beam to be out of phase and diminish the contrast.

5.6 Quantum Mechanical Simulation

To determine if the observed contrast is consistent with quantum mechanics and to rule out a classical explanation, both quantum mechanical and classical numerical simulations were performed. The quantum mechanical theoretical description of the physical system is based on Feynman's path integral formalism, and is discussed in detail in Section 2.3 and 2.4. while the classical description is based on particle trajectories.

In the quantum mechanical description the wave function was propagated from the plane of the first collimation slit to the second collimation slit then to each grating (three in total). At the first collimation slit multiple incoherent sources were propagated through the system. The resulting probability distribution at the third grating was integrated in x, this was the throughput of the TLI.

At the collimation slits and gratings an image charge potential was added. Additionally at the gratings a random potential was added. The values describing the interaction were identical to the ones used by Barwick et al.,[33] see Table 4.2. In

fact the exact grating used to determine the values of the image charge and random potential was one of the three gratings used in the TLI.

In the classical description random electron trajectories were propagated from the first collimation slit through the rest of the system. At each plane an image charge force, determined by Equation 2.35, was applied that gave an impulse in the transverse direction.

To enable the simulations to be competed in a reasonable time, the magnetic field was left out. Instead the third grating was translated transversely to mimic the deflection from the magnetic field. The contrast was determined from the throughput as a function of the third grating position. This procedure was repeated for different energies. The experimental and theoretical results for both the classical and quantum mechanical simulations are shown in Figure 5.7(a) and (b) respectively.

The shape of the quantum simulation qualitatively matches the experimental data better than the classical, but the scale of the contrast is different. The simulations represent the best case scenario of a perfectly shielded environment and ideal rotational alignment. Estimating a beam height of 33 μm at the TLI and a misalignment of 10^{-3} rad, the contrast would be reduced by a factor of 2.4. This is beleved to be the dominant contribution to the discrepancy between the experiment and theory. The only fit parameter was the open fraction. An open fraction of 35% best represented the two contrast maxima, whereas the gratings were originally manufactured to be 50-60%.

The effect of the image charge and random potential was to generally lower the contrast and smooth out the energy dependence, see Figure 5.8. The effects were needed to simulate the double-slit diffraction, see Section 4.5, so they were included in the simulations to be complete, even thought they do not change the general features of the contrast. The classical Moire-Deflectometer's contrast increases to 56% and 49% (2 and 30 μm collimation slit respectively), with no image charge, and has

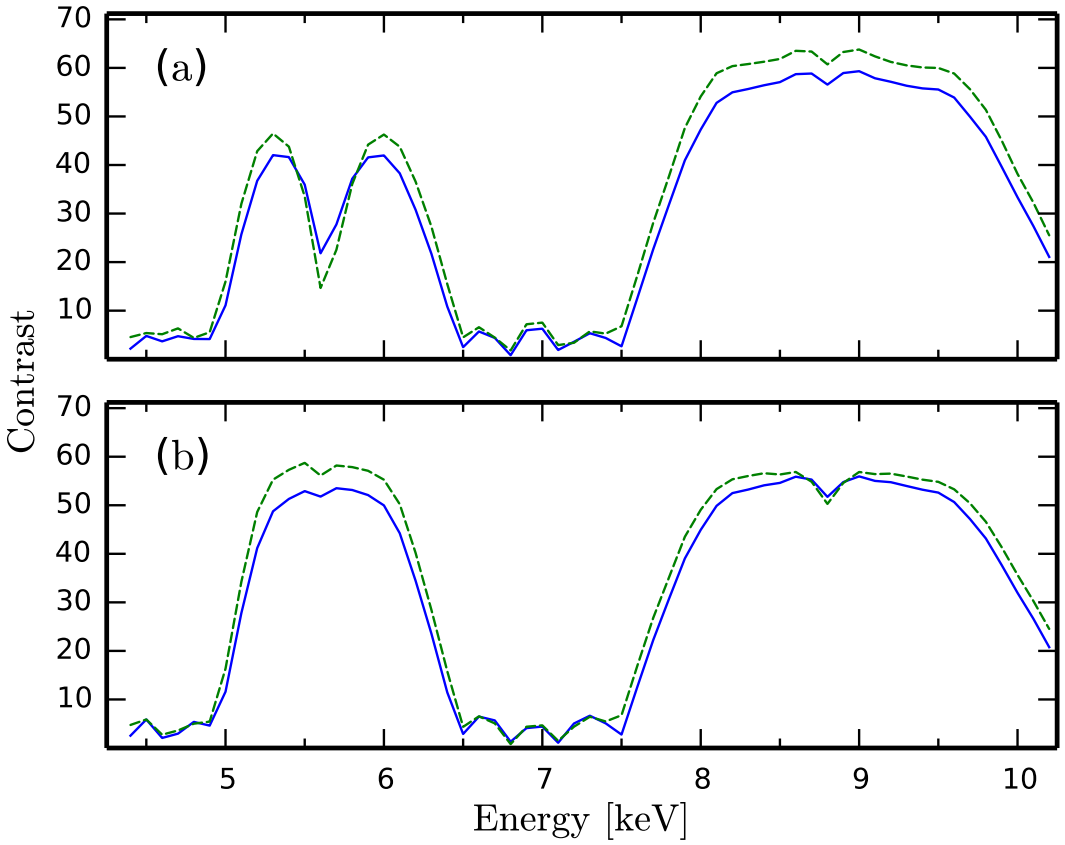

Figure 5.8. The quantum mechanical simulation can be run with the image charge effects and random potentials on, solid (blue) line, or off, dashed (green) line. The contrast as a function of energy is shown above for the 2 μm (a) and 30 μm second collimation slit.

no energy dependence.

5.7 Stability

The fringe pattern is stable over hours. Generally the contrast would vary only after more than 4 hours but could be regained by moving the beam to a different location on the interferometer. This may be due to some degradation of the gratings. Figure 5.9 shows two runs that were used in Figure 5.6. These runs were separated by 2 hours, the lower being taken after the upper. During this time the electron gun's energy was ramped down to 4.5 keV and then back up, so the incident inten-

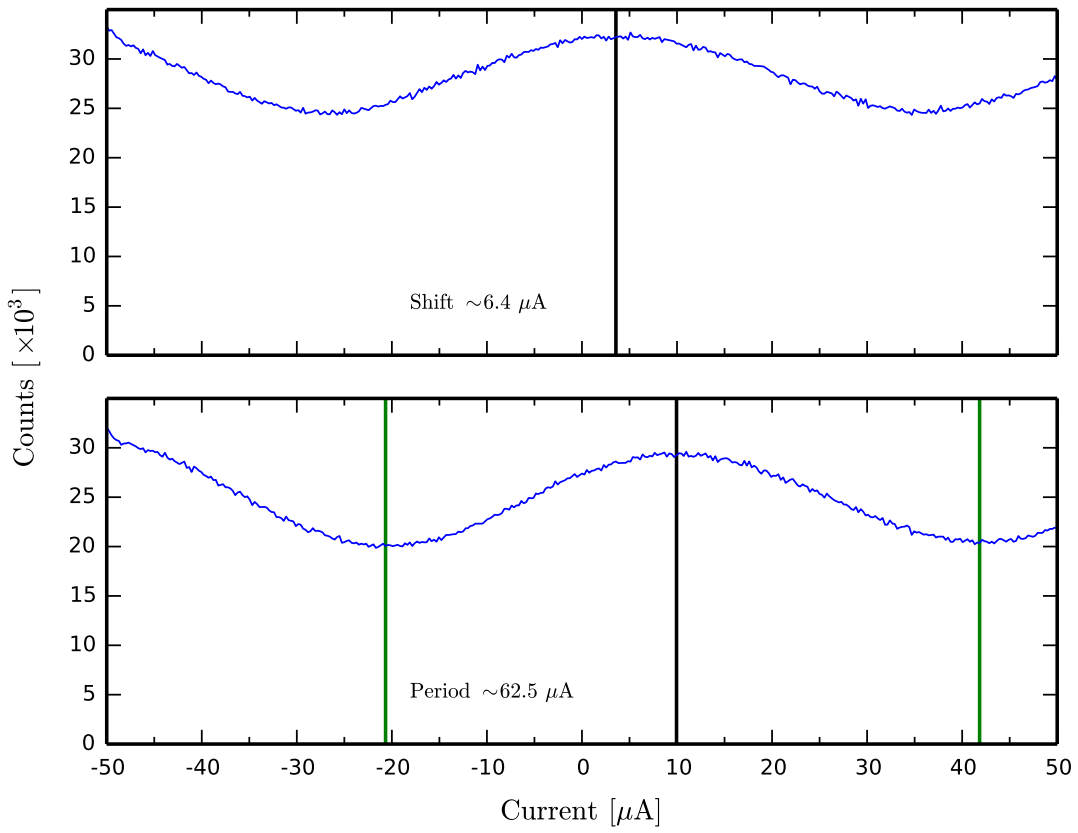

Figure 5.9. Shown above are two runs separated by 2 hours, the lower being taken after the upper. The horizontal shift corresponds to a magnetic field of approximately 55 nT or an equivalent electric field

sity was not held constant, due to having to slightly change the alignments of gun during ramping. The energy was 8.5 keV and the 30 μm collimation slit was used. There is an increase in the contrast (13% $\rightarrow$ 18%) and the horizontal shift corresponds to a magnetic field of approximately 55 nT or an equivalent electric field. This could possibly result from charging or some uncontrolled external magnetic field, since the system shielding only attenuated the magnetic field by a factor of 100.

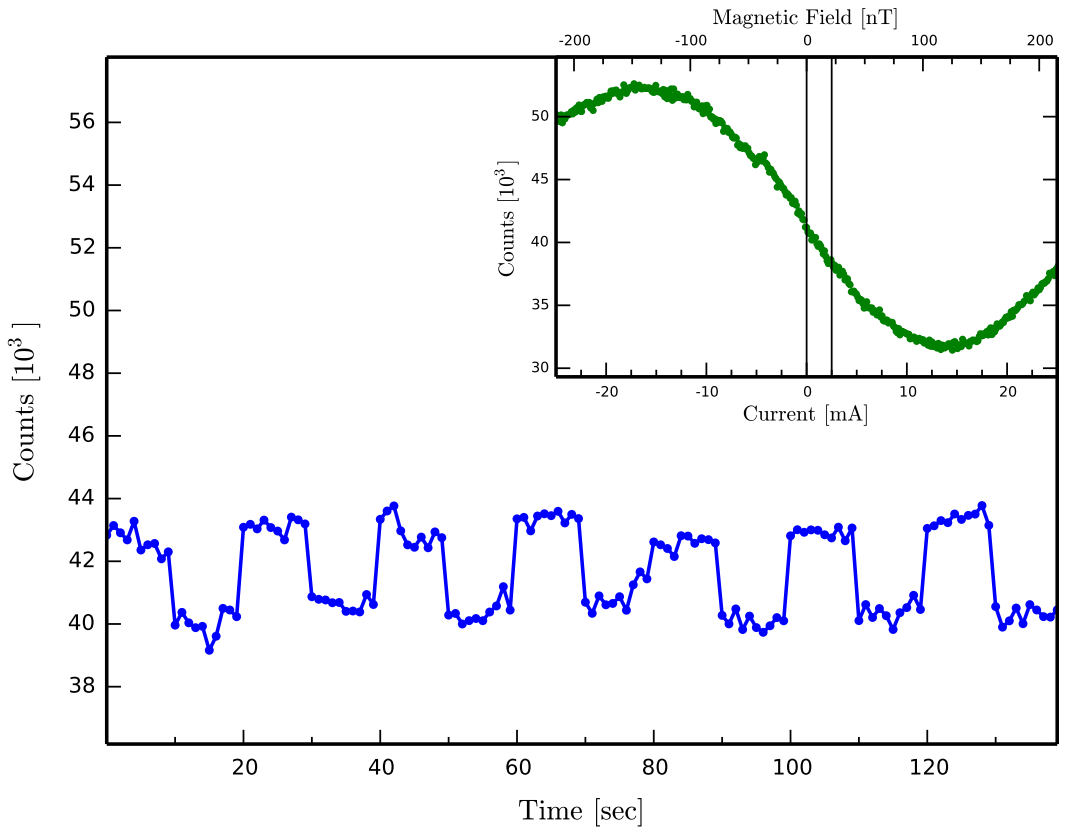

Figure 5.10. To demonstrate the measurement of a magnetic field, a small current was turned on then off repeatedly. The main graph shows the throughput of the Talbot-Lau interferometer. A current of 2.5 mA, which corresponds to a field of 22 nT, was tuned on for 10 s then left off for 10 s. The inset shows a larger scan of the current. The two vertical lines represent the currents used during the magnetic field measurement

5.8 Sensitivity

To determine the sensitivity of the TLI a small magnetic field was applied. A small voltage on the set of parallel plates placed the TLI in an electric field of approximately 200 V/m to shift the throughput to be most sensitive to a change in magnetic field (Figure 5.10 inset). A 2.5 mA current was turned on for 10 s and then left off for 10 s. The electron throughput is shown in Figure 5.10. Each point represents 1 sec of integration. The current corresponds to a field of 22 nT. The signal to noise in Figure 5.10 is approximately 4.5 for a measurement of 1 s duration. The

sensitivity is thus about 4.7 $\mathrm{nT\,Hz^{-1/2}}$.

This is a modest result as compared to what can be reached with conventional devices, e.g., fluxgate magnetometers,[14] atomic sensors,[86] or squids,[87] but is a proof of principle for the operation of the device. The scalability of the TLI magnetic sensor is discussed below.

5.9 Scalability

Several steps can be taken to scale the device. The electron beams become separated at a grating distance of 20 mm and changes from a near-field to a far-field Mach-Zehnder interferometer.[34] For a separation of approximately 9 mm, the device length L increases by a factor of 3 as compared to our present design, which would still be an integer multiple of half the Talbot length. For an improved rotational alignment, the full surface of the grating (1 mm $\times$ 3 mm) could be used at the same electron beam density to increase the throughput N by (1 mm $\times$ 10 mm)/(30 μm $\times$ 30 μm) $\approx$ 11000. Finally the magnetic flux can be improved by a factor C of 20 with a typical weak iron magnetic field concentrator.[88] The sensitivity scales with $L^2CN^{1/2}$ (using Equation 5.4 and assuming a shot noise limited signal). An expected performance of a scaled device would thus be 250 $\mathrm{fT\,Hz^{-1/2}}$. Additionally, the device works in modest bias fields (3 μT), while its frequency response remains to be explored.

5.10 Conclusion

In summary, a Talbot-Lau electron interferometer has been demonstrated. The device acts as a magnetometer with a modest sensitivity of 4.7 $\mathrm{nT\,Hz^{-1/2}}$, but appears to be scalable to higher sensitivity. The use of charged particle interferometry as an alternative means to magnetic field sensing as a proof of principle is clear and

appears interesting, because its parameter space remains largely unexplored.

Chapter 6

Conclusion

6.1 Talbot-Lau Interferometer

One main result of this work is the realization of a three grating Talbot-Lau interferometer for electrons. In fact this work it the first demonstration of this kind of interferometer for any charged particle. While, the current sensitivity of 4.7 nT $Hz^{-1/2}$ is modest compared to what can be reached with conventional devices, e.g., fluxgate magnetometers,[14] atomic sensors,[86] or squids,[87] the predicted scaling of 250 fT $Hz^{-1/2}$ could push the device into a competitive domain. In a commercial device, such as a magnetic anomaly detector, the mechanical stability, the ability to work in biased fields, and the frequency response all come into play. All of which have not been explored for this Talbot-Lau interferometer.

Using the current Talbot-Lau interferometer to probe fundamental physics or as a magnetic anomaly detector might prove challenging. But, based on the success of this device and other atomic or molecular interferometers[28,34,42,43,51,70,71,89,90] using gratings, it may be interesting to investigate electron grating interferometers further.

6.2 Double-Slit Diffraction

The double-slit diffraction experiment is a corner stone of quantum mechanics, and as such, has, and still is, receiving justifiably extreme scrutiny.[91–94] Even though the quantum mechanics we know now, has been around for over 85 years, some things are still uncertain about the double-slit. One major question is what happens between the source, the double-slit, and the detector.

There are many interpretations of what happens. The electron exists in many worlds and all possible detection outcomes are realized.[95,96] The electron exists at all times as a particle but is guided by a quantum wave to it's detected position.[97,98] Others say that it is wrong to speak of "what it is doing" between the source and the detector.[99] They say that the elementary quantum phenomenon is a "great smoky dragon." The beginning and end are sharp but about "what the dragon does or looks like in between we have no right to speak." Nevertheless, all interpretations predict the same measurable phenomenon.

A fascinating recent result is the observation of double-slit diffraction buildup for oil droplets.[100] This experiment is performed at macroscopic scales, where the physical system is well described by classical equations of motion, but can nevertheless produce a diffraction pattern from the build-up of individual droplets. In the experiment a bouncing oil droplet and an accompanying fluid wave excitation travel together, reminiscent of de Broglie-Bohm theory.[97,98] However, the guidance in this experiment is affected by a "real" fluid wave. This widely publicized result[101] has stimulated further discussion of the interpretations of quantum theory and speculation on quantum mechanics emergent from an unknown underlying theory.[102]

Such "emergent" quantum physical theories are not merely interpretations, but can make testable, differing predictions. For example, in the past decades, the theory of stochastic electrodynamics has been considered by some an alternative to quantum mechanics.[103,104] Claims in this research area include that double-slit

electron diffraction can be obtained with a full classical theory that includes the electromagnetic vacuum field.[105–111] These claims are based on the idea that the double-slit provides a boundary condition for the vacuum field. An electron interacting with the vacuum field can sense the presence of both slits even if the electron itself is localized to one slit. This idea led one group to suggest that electrons that are limited to move through one slit, while both slits are present, would still show a double-slit diffraction pattern,[110] in stark contrast to what quantum mechanics predicts. Our experiment shows that this suggestion is in general not correct, but a full calculation with stochastic electrodynamics for the double-slit scenario (with or without blocking one of the slits) has still not been performed.

Our experimental control also points towards, future quantum matter optics experiments with free electrons. Recently, a three slit buildup experiment with controllable slits was reported for photons investigating the Born rule.[92] It was shown that terms in the probability that are proportional to the third power of the wave function are negligible. Such control is now available for electrons and our experiment shows that a similar Born rule test for massive particles, i.e., electrons, is feasible.

In summary a full realization of Feynman's thought experiment was shown and the present results are an important milestone in the development of technology and methods relevant to testing the foundations of quantum mechanics.

Appendix A – Path Integral Calculation for the Harmonic Oscillator

The harmonic oscillator is a important system. Not only is it a system that can be exactly solved, but any potential with a stable equilibrium may be described by a oscillator near the equilibrium. The calculation of the propagator is a formidable task with the Schrodinger equation. The path integral formalism gives us a simpler method for calculating the propagator or kernel. The kernel in path integral formalism is

$$K(\vec{x},t;\vec{x}',t') = A(t;t')\exp\left[\frac{i}{\hbar}S(\vec{x},t;\vec{x}',t')\right], \tag{A.1}$$

where A is a normalization factor that only depends on time and S is the classical action of the path.

Starting with the Lagrangian for a one dimensional harmonic oscillator, which is $L = \frac{m}{2}\dot{x}^2 - \frac{m\omega^2}{2}x^2$, the classical paths can be found. Here m is the mass of the particle and ω is the classical frequency of the oscillator. The classical paths can be calculated by solving the Euler-Lagrange equation,

$$\frac{d}{dt}\frac{\partial L}{\partial \dot{x}} - \frac{\partial L}{\partial x} = 0. \tag{A.2}$$

This gives the differential equation $\ddot{x} + \omega^2 x = 0$. This has known solutions of the form:

$$\begin{aligned} x(t) &= A\cos(\omega t) + B\sin(\omega t), \\ \dot{x}(t) &= -A\omega\sin(\omega t) + B\omega\cos(\omega t), \\ \ddot{x}(t) &= -A\omega^2\cos(\omega t) - B\omega^2\sin(\omega t). \end{aligned} \tag{A.3}$$

Here A and B are unknown constants that can be solve for by using the boundary conditions $x(t_a) = x_a$ and $x(t_b) = x_b$.

There are two equations with two unknowns after using the boundary conditions:

$$x(t_a) = A\cos(\omega t_a) + B\sin(\omega t_a), \tag{A.4}$$

$$x(t_b) = A\cos(\omega t_b) + B\sin(\omega t_b). \tag{A.5}$$

Solving Equation A.4 for A and substituting into Equation A.5, the constant B can be determined. Similarly A can found, giving:

$$A = \frac{x_a \sin(\omega t_b) - x_b \sin(\omega t_a)}{\sin\left[\omega(t_b - t_a)\right]}, \tag{A.6}$$

$$B = \frac{x_b \sin(\omega t_a) - x_a \sin(\omega t_b)}{\sin\left[\omega(t_b - t_a)\right]}. \tag{A.7}$$

Substituting these back into Equation A.3 and using some trigonometric addition formulas, the classical paths are:

$$\begin{aligned}
x(t) &= \frac{1}{\sin\left[\omega(t_b - t_a)\right]} \left\{x_a \sin\left[\omega(t_b - t)\right] + x_b \sin\left[\omega(t - t_a)\right]\right\}, \\
\dot{x}(t) &= \frac{\omega}{\sin\left[\omega(t_b - t_a)\right]} \left\{-x_a \cos\left[\omega(t_b - t)\right] + x_b \cos\left[\omega(t - t_a)\right]\right\}, \\
\ddot{x}(t) &= \frac{-\omega^2}{\sin\left[\omega(t_b - t_a)\right]} \left\{x_a \sin\left[\omega(t_b - t)\right] + x_b \sin\left[\omega(t - t_a)\right]\right\}.
\end{aligned} \tag{A.8}$$

In the limit of $\omega = 0$ Equation A.8 reduces to the free particle solution, Equation 2.10,

$$\begin{aligned}
x(t) &= \frac{1}{t_b - t_a}\left[x_a(t_b - t) + x_b(t - t_a)\right] = \frac{1}{t_b - t_a}\left[x_a(t_b - t_a - t + t_a) + x_b(t - t_a)\right] \\
&= x_a + \frac{(t - t_a)(x_b - x_a)}{t_b - t_a}.
\end{aligned} \tag{A.9}$$

The next step in solving the propagator for the harmonic oscillator is to calculate the classical action. To do this, Equation A.8 is substituted into the Lagrangian,

$$L(x_b,t_b;x_a,t_a) = \frac{m\omega^2}{2}\frac{1}{\sin\left[\omega(t_b-t_a)\right]}\left\{x_a^2\left[\cos^2\left[\omega(t_b-t)\right]-\sin^2\left[\omega(t_b-t)\right]\right]\right.$$
$$+x_b^2\left[\cos^2\left[\omega(t-t_a)\right]-\sin^2\left[\omega(t-t_a)\right]\right]$$
$$\left.-2x_ax_b\cos\left[\omega(t_b-t)-\omega(t-t_a)\right]\right\}. \tag{A.10}$$

Then Equation A.10 need to be integrated in time from t_a to t_b to calculate the action,

$$S(x_b,t_b;x_a,t_a) = \frac{m\omega^2}{2\sin(\omega T)}\left\{\frac{x_a^2+x_b^2}{\omega}\int_0^{\omega T} du\ \left[\cos^2(u)-\sin^2(u)\right]\right.$$
$$\left.-\frac{x_ax_b}{\omega}\int_{-\omega T}^{\omega T} dv\ \cos(v)\right\}, \tag{A.11}$$

where substitutions were used: $u = \omega(t_b - t)$, $u = \omega(t - t_a)$, and $v = \omega(t_b - t) - \omega(t - t_a)$, in the first, second, and last terms in Equation A.10 respectively, and $T = t_a - t_b$. After evaluation the classical action becomes,

$$S(x_b,t_b;x_a,t_a) = m\omega\left\{\frac{(x_a^2+x_b^2)\cos\left[\omega(t_b-t_a)\right]-2x_ax_b}{2\sin\left[\omega(t_b-t_a)\right]}\right\}. \tag{A.12}$$

The normalization factor in Equation A.1 can be found using $K(0,t_b;0,t_a) =$

$A(t_b;t_a)$ and that for any time t_c between t_a and t_b,

$$\begin{aligned} K(0,t_b;0,t_a) &= \int_{-\infty}^{\infty} dx_c\, K(0,t_b;x_c,t_c)\, K(x_c,t_c;0,t_a) \\ &= A(t_b;t_c)A(t_c;t_a)\int_{-\infty}^{\infty} dx_c \exp\left[\frac{im\omega}{\hbar}\left\{\frac{x_c^2\cos\left[\omega(t_b-t_c)\right]}{2\sin\left[\omega(t_b-t_c)\right]}\right\}\right]\times \\ &\qquad \exp\left[\frac{im\omega}{\hbar}\left\{\frac{x_c^2\cos\left[\omega(t_c-t_a)\right]}{2\sin\left[\omega(t_c-t_a)\right]}\right\}\right] \\ &= A(t_b;t_c)A(t_c;t_a)\sqrt{\frac{2\pi i\hbar}{m\omega}}\left[\frac{\cos\left[\omega(t_c-t_a)\right]}{\sin\left[\omega(t_c-t_a)\right]}+\frac{\cos\left[\omega(t_b-t_c)\right]}{\cos\left[\omega(t_b-t_c)\right]}\right]^{-1/2}. \end{aligned} \tag{A.13}$$

After some trigonometric substitutions this equation simplifies down to,

$$\begin{aligned} A(t_b;t_a)\left\{\sin\left[\omega(t_b-t_a)\right]\right\}^{1/2} = \sqrt{\frac{2\pi i\hbar}{m\omega}}A(t_b;t_c)\left\{\sin\left[\omega(t_b-t_c)\right]\right\}^{1/2}\times \\ A(t_c;t_a)\left\{\sin\left[\omega(t_c-t_a)\right]\right\}^{1/2} \end{aligned} \tag{A.14}$$

The solution to the normalization constant is

$$A(t_b;t_a) = \sqrt{\frac{m\omega}{2\pi i\hbar\sin\left[\omega(t_b-t_a)\right]}}. \tag{A.15}$$

Substituting Equation A.15 and Equation A.12 into Equation A.1,tThe end result for the kernel is

$$\begin{aligned} K(x_b,t_b;x_a,t_a) = \left(\frac{m\omega}{2\pi i\hbar\sin[\omega(t_b-t_a)]}\right)^{1/2}\times \\ \exp\left\{\frac{im\omega}{\hbar}\left[\frac{(x_a^2+x_b^2)\cos[\omega(t_b-t_a)]-2x_ax_b}{2\sin[\omega(t_b-t_a)]}\right]\right\}. \end{aligned} \tag{A.16}$$

This is the propagator or kernel for the harmonic oscillator. It can also be easily seen that in the limit of $\omega \to 0$, Equation A.16 reduces to the free particle propaga-

tor in one dimension, Equation 2.21.

Appendix B – Image Aquisition Labview Code

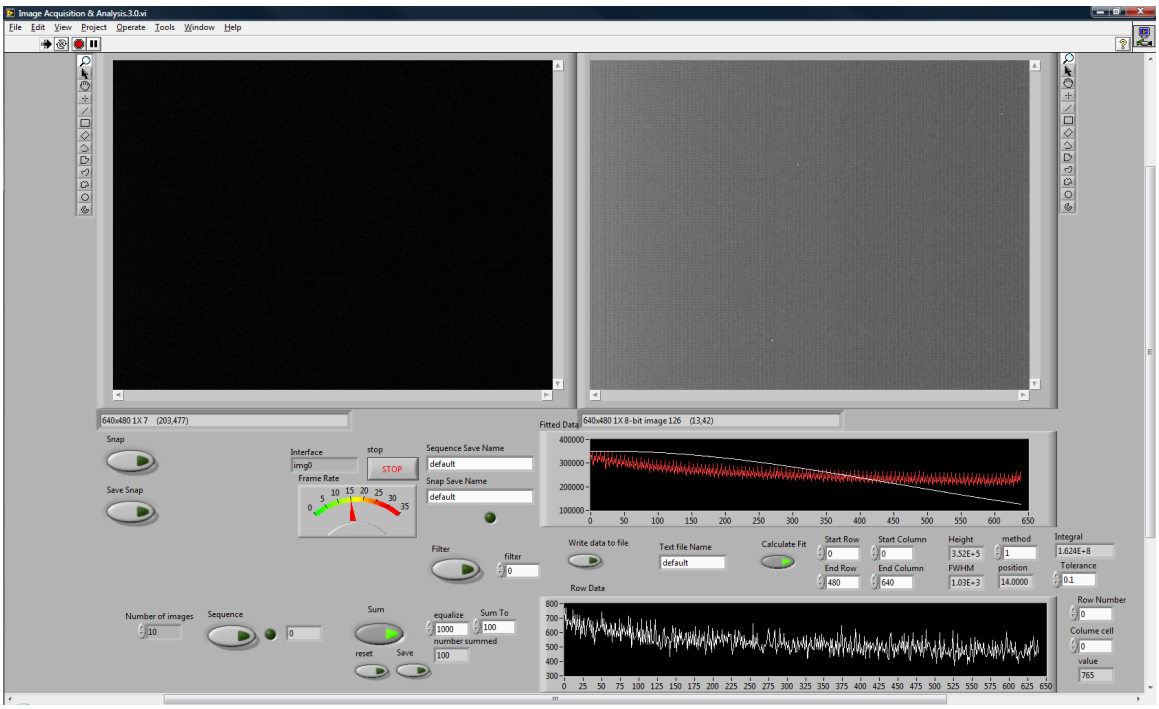

Front Panel

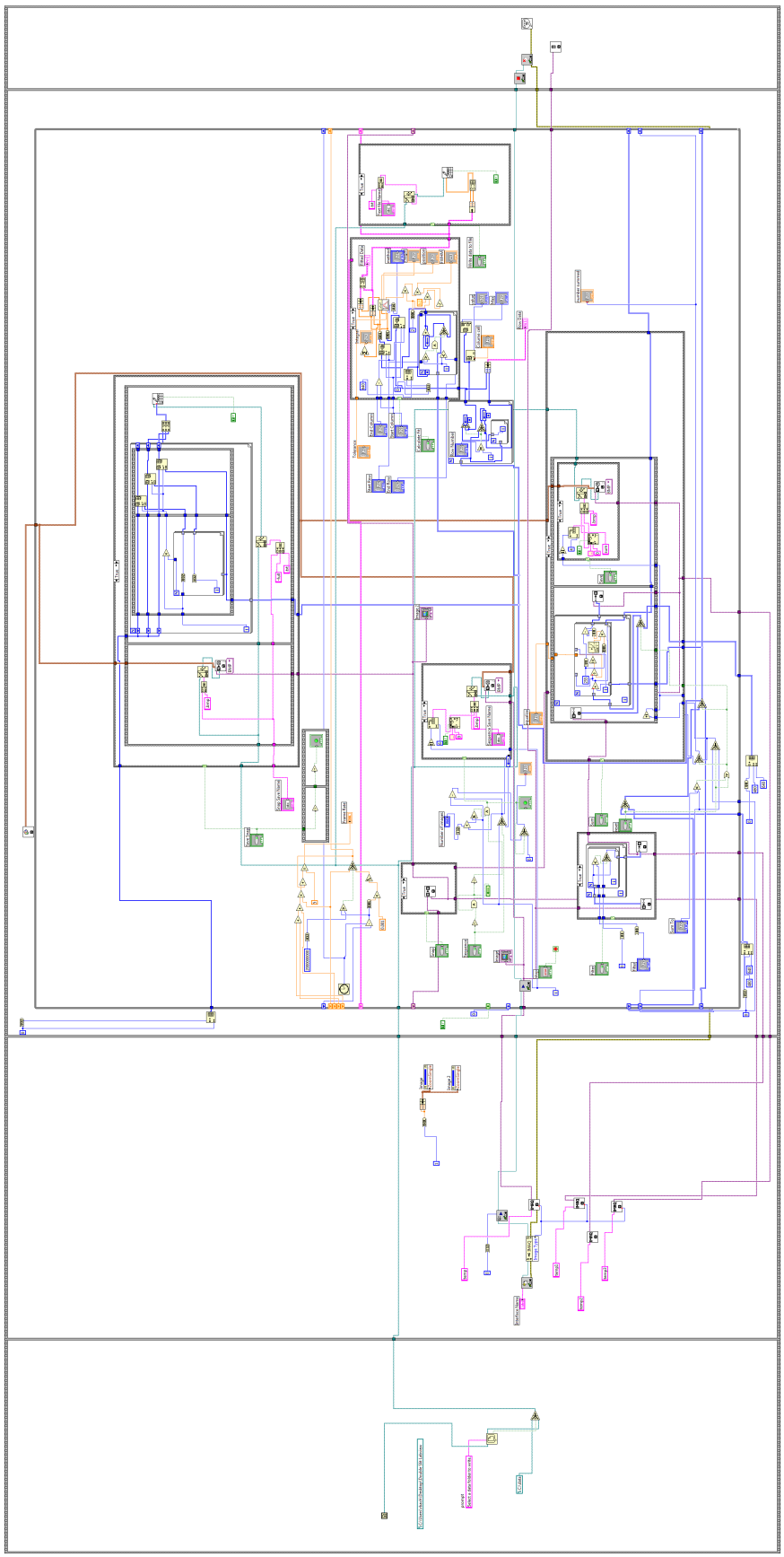

Back Panel

Appendix C – Computer Simulations and Analysis Programs

The simulation and analysis programs should be available online through the University of Nebraska-Lincoln's data repository. Searching for "Electron Double-Slit" or "Talbot-Lau Interferometer," will allow for the code and data to be found.

Double-Slit Image Analysis Programs

`bitmap_locations.cpp`

This program take a sequence of images and analyses each, looking for electron events. The program uses the four custom classes: `Blob_Detection`, `location_list`, `location_list_double`, and `bitmap8`. Using the `makefile` below, will generate an executable `blob_finder_<date>.out`. The first time this program is run it will generate a `specifications.txt` file, which can be edited to change the basename and sequence numbers of the images to be analyzed. After running again, the program will output a master list, `Master_list_<basename>.txt`, containing the electron event's locations. It will also generate an image, `Master_bitmap.bmp`, that represents the locations of the electron events.

`blob_placement.cpp`

This program takes a list of electron events and generates a stacked set of images. The program uses the four custom classes `Blob_Detection`, `location_list`, `location_list_double`, and `bitmap8`. Using the `makefile` below, will generate an executable `blob_placer_<date>.out`. This program requires the `Master_list_<basename>.txt` and `specifications.txt` files from `bitmap_locations.cpp` to run. The first time this program is run it will generate a

placement_specifications.txt file, which can be edited to change the zoom window and angle; progress bar, size of the mapped window, and whether to generate intermediate bitmaps. After running again, the program will read the master list, Master_list_<basename>.txt, and generate a stacked sequence of images showing the build-up of the images replacing the electron events with blobs of a specified size.

makefile

This is the makefile to compile blob_placement.cpp and bitmap_locations.cpp. It requires the files: header_files/bitmap8.cpp, header_files/location_list.cpp, and header_files/Blob_Detection.cpp, to compile and uses the gnu g++ compiler. It will generate the two executables: blob_finder_<date>.out and blob_placer_<date>.out, where <date> is the current date.

cpp_files/ and header_files/

These contain the header and .cpp files for the classes Blob_Detection, location_list, location_list_double, and bitmap8.

bitmap8

Custom class designed to handle reading and writing 8-bit bitmaps. The class can also do some basic functions. These include: assigning values to pixels, reading pixel values, getting the bitmap's width or length, getting the maximum value, and copying bitmaps.

location_list

Custom class designed to handle a list of (x, y) integer locations. The list can be expandable on demand. The class can also do some basic functions. These include: adding locations, changing locations, removing locations, reading locations, copying lists, and adding lists.

`location_list_double`

Custom class designed to handle a list of (x, y) double locations. This class is identical to `location_list` except that this list includes an error associated with each location.

`Blob_Detection`

Custom class designed to handle the search algorithm. It is given a bitmap file loaded into the `bitmap8` class. This class has several function to search an entire bitmap, an area of the bitmap, or search within a single pixel with more accuracy. Also this class has ways to adjust the parameters of the search.

Double-Slit Quantum Mechanical Simulation

`Double_Slit.F90`

This program propagates a quantum mechanical wave function through the experimental setup. The program is written in FORTRAN with support for shared-memory and distributed memory parallel computing through OpenMP and Open MPI. The code is 2129 lines long and required approximately 2.5 hours of run time on 24 processors on Tusker cluster at the Research Computing Facilities at the University of Nebraska-Lincoln. The code was compiled with the `makefile` listed below. The program outputs multiple text files that represent the probability distribution of the propagated wave function at different elements of the system.

`graph_cs.py`, `graph_ds.py`, `graph_ma.py`, `graph_sc.py`, and `graph_conv.py`

These programs take the outputted text files from `Double_Slit.F90` and generate graphs of the probability distributions. The programs graph the probability distributions at the: **c**ollimation **s**lit, **d**ouble-**s**lit, **ma**sk, detection **sc**reen, and the detection screen after being magnified and **conv**oluted.

`makefile`

This is the makefile used to compile `Double_Slit.F90` and generate graphs of the data. It uses Open MPI's wrapper compiler and defaults to compile with OpenMP. Running the default make is used to compile on the cluster, while running:

```
[shell]$ make laptop
```

will use the compiler `/opt/openmpi/bin/mpif90`, and will not compile with 64 bit support. A shortcut for generating all the graphs is:

```
[shell]$ make graph
```

Talbot-Lau Interferometer Classical Simulation

`Moire.F90`

This program propagates classical electrons through the experimental setup. The program is written in FORTRAN with support for shared-memory parallel computing through OpenMP. The code is 774 lines long and required approximately 6 hours of run time on 16 processors on Tusker cluster at the Research Computing Facilities at the University of Nebraska-Lincoln, for the optimal settings. The code was compiled with the `makefile`. The program outputs multiple text files that represent the electron's positions at different elements of the system.

`graph2.py`, `graph3.py`, `graph4.py`, `graph5.py`, and `graph6.py`, `graph7.py`

These programs take the outputted text files from `Moire.F90` and generates histograms of the electron's positions. The programs graph the histograms at the: second slit, first grating, second grating, third grating, throughput at the third grating, and the throughput with a magnetic field.

`makefile`

This is the makefile used to compile `Moire.F90` and generate graphs of the data. It defaults to compile with OpenMP. Running the default "make" will compile it with the gnu gfortran compiler. A shortcut for generating all the graphs is:

```
[shell]$ make graph
```

Talbot-Lau Interferometer Quantum Mechanical Simulation

`Talbot-Lau.F90`

This program propagates a quantum mechanical wave function through the experimental setup. The program is written in FORTRAN with support for shared-memory and distributed memory parallel computing through OpenMP and Open MPI. The code is 1957 lines long and required approximately 100 hours of run time on 32 processors on Tusker cluster at the Research Computing Facilities at the University of Nebraska-Lincoln, for the optimal settings. The code was compiled with the `makefile`. The program outputs multiple text files that represent the probability distribution of the propagated wave function at different elements of the system.

`graph1.py`, `graph2.py`, `graph3.py`, `graph3.py`, and `graph5.py`, `graph6.py`, `contrast.py`

These programs take the outputted text files from `Talbot-Lau.F90` and generate graphs of the probability distributions. The programs graph the probabil-

ity distributions at the: second grating, third grating, throughput at the third grating, first grating, first collimation slit, and second collimation slit

`makefile`

This is the makefile used to compile `Talbot-Lau.F90` and generate graphs of the data. It uses Open MPI's wrapper compiler and defaults to compile with OpenMP. Running the default "make" is used to compile on the cluster, while running:

```
[shell]$ make mpi_laptop
```

will use the compiler `/opt/openmpi/bin/mpif90`, and will not compile with 64 bit support. A shortcut for generating all the graphs is: `[shell]\$ make graph`

Appendix D – Computer-Aided Design Drawings

Talbot-Lau Interferometer

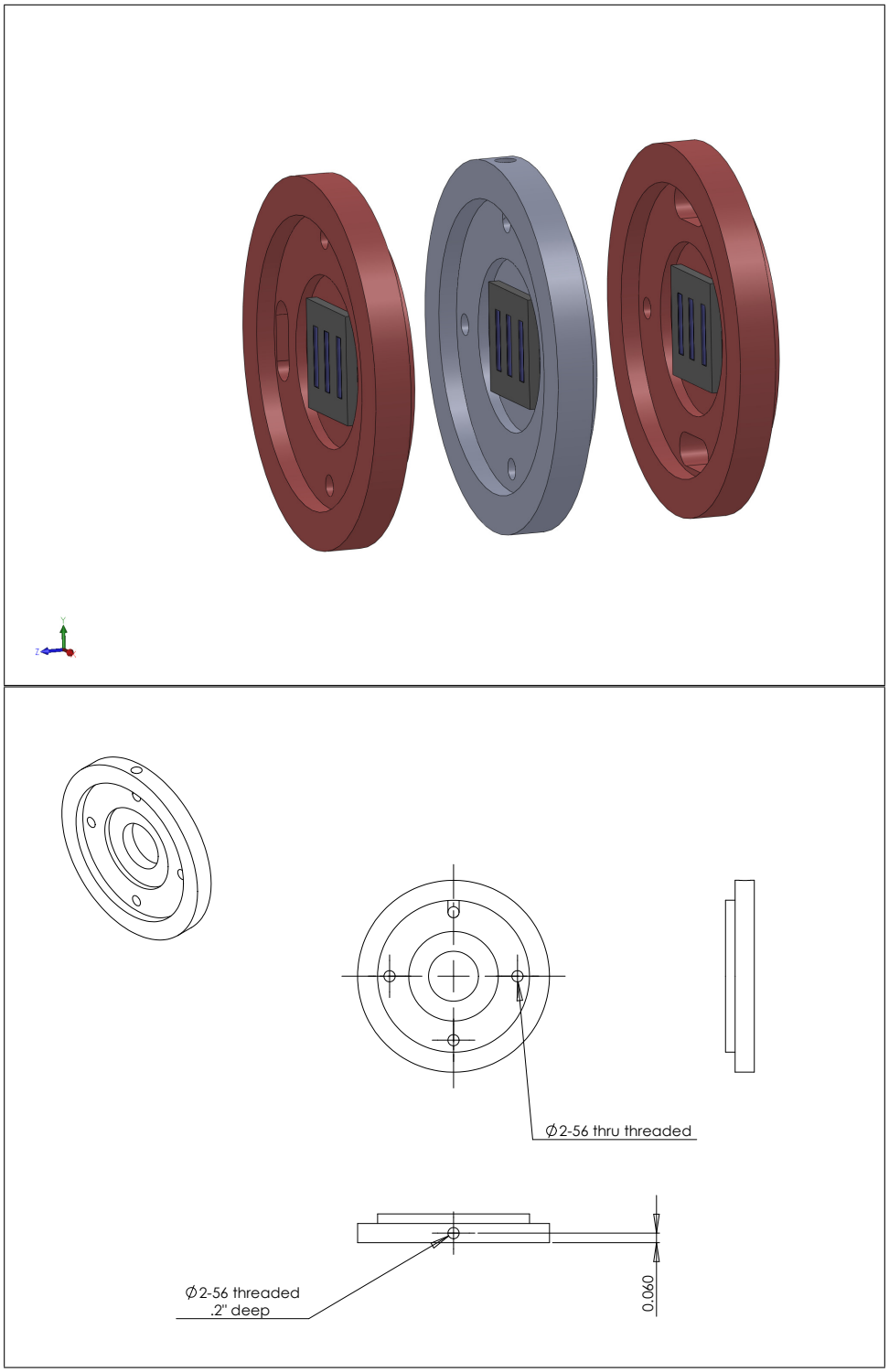

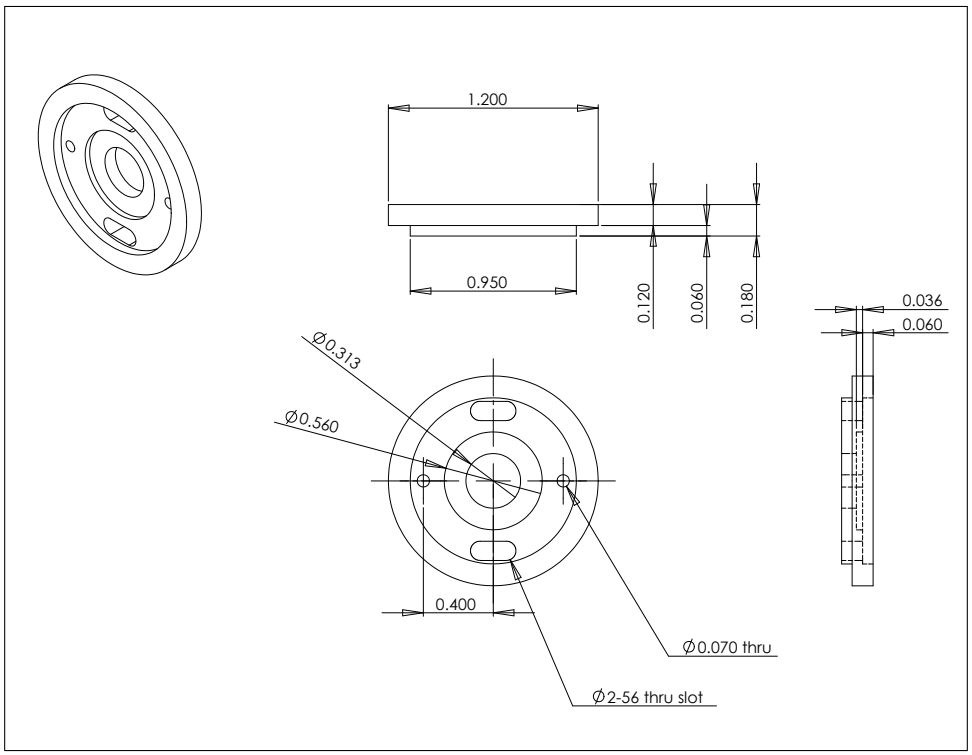

Magnetic Cradle

The design for the magnetic cradle was quite complicated. Multiple CAD drawing were made showing intermediate steps. To prevent unnecessary bloat of the dissertation the drawing were compacted. The images can be zoomed in on a digital copy of this dissertation and all dimension can be viewed.

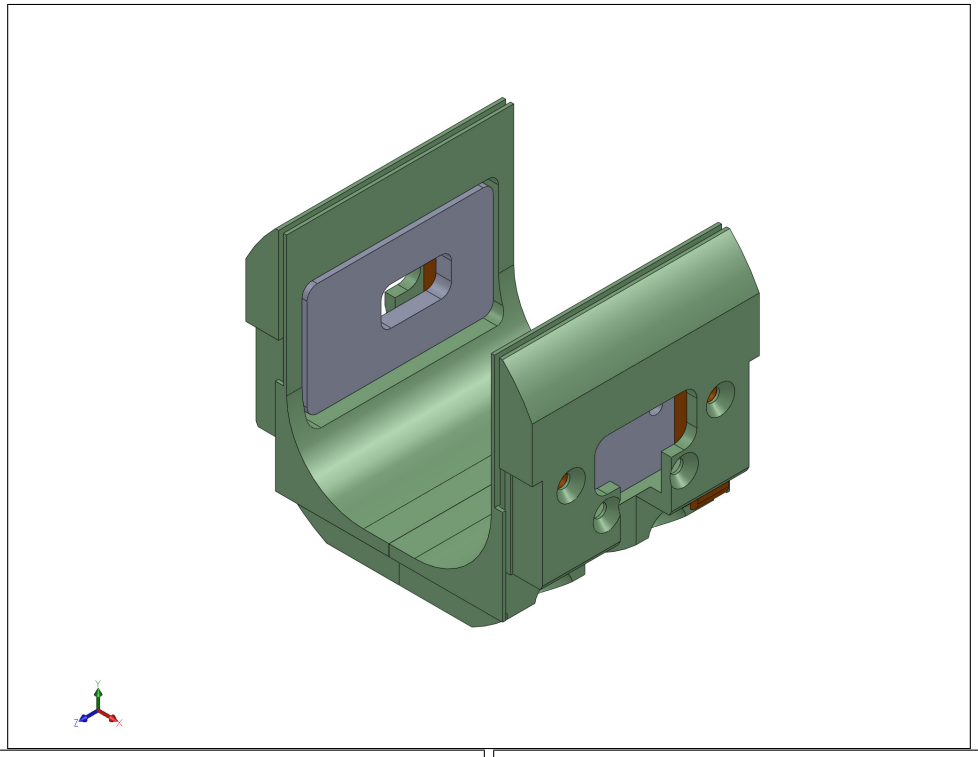

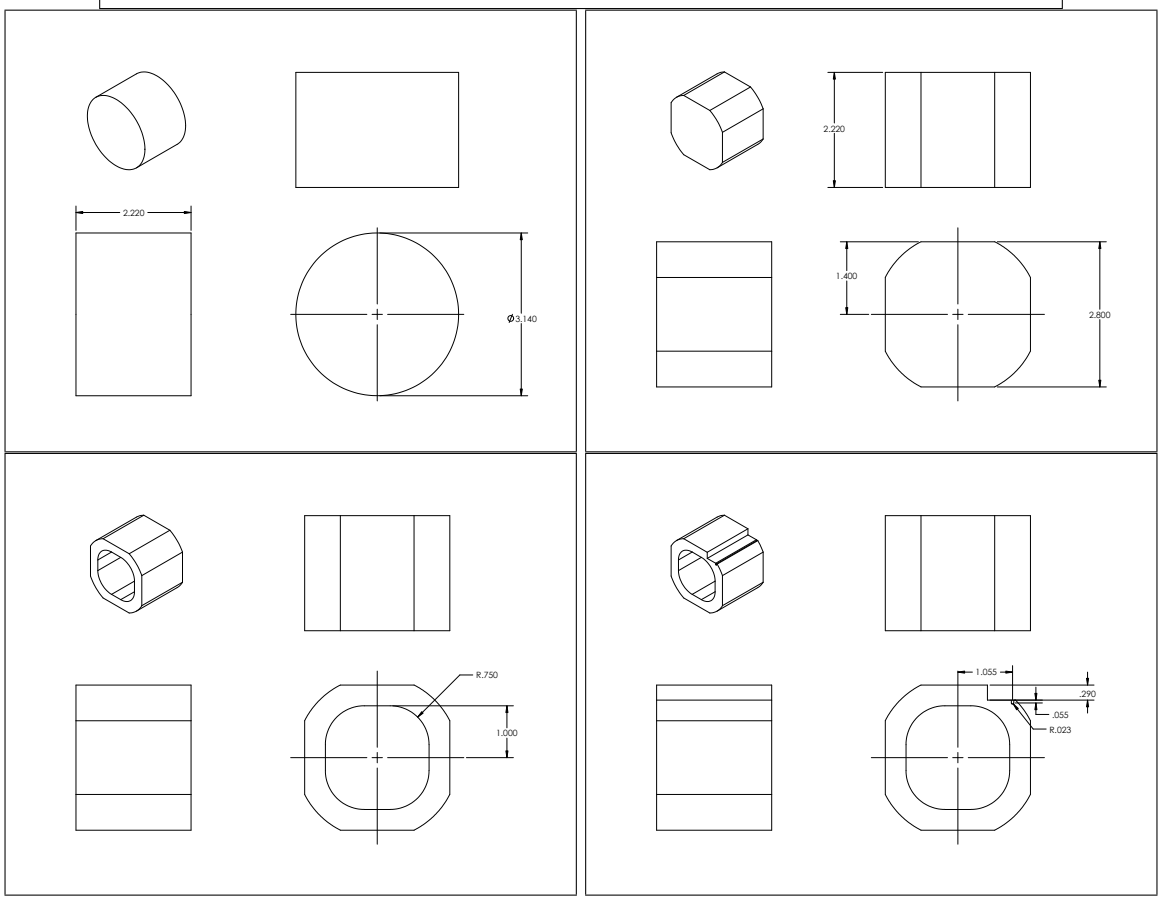
2.220
Ø3.140
2.220
1.400
2.800
R.750
1.000
1.055
.290
.055
R.023

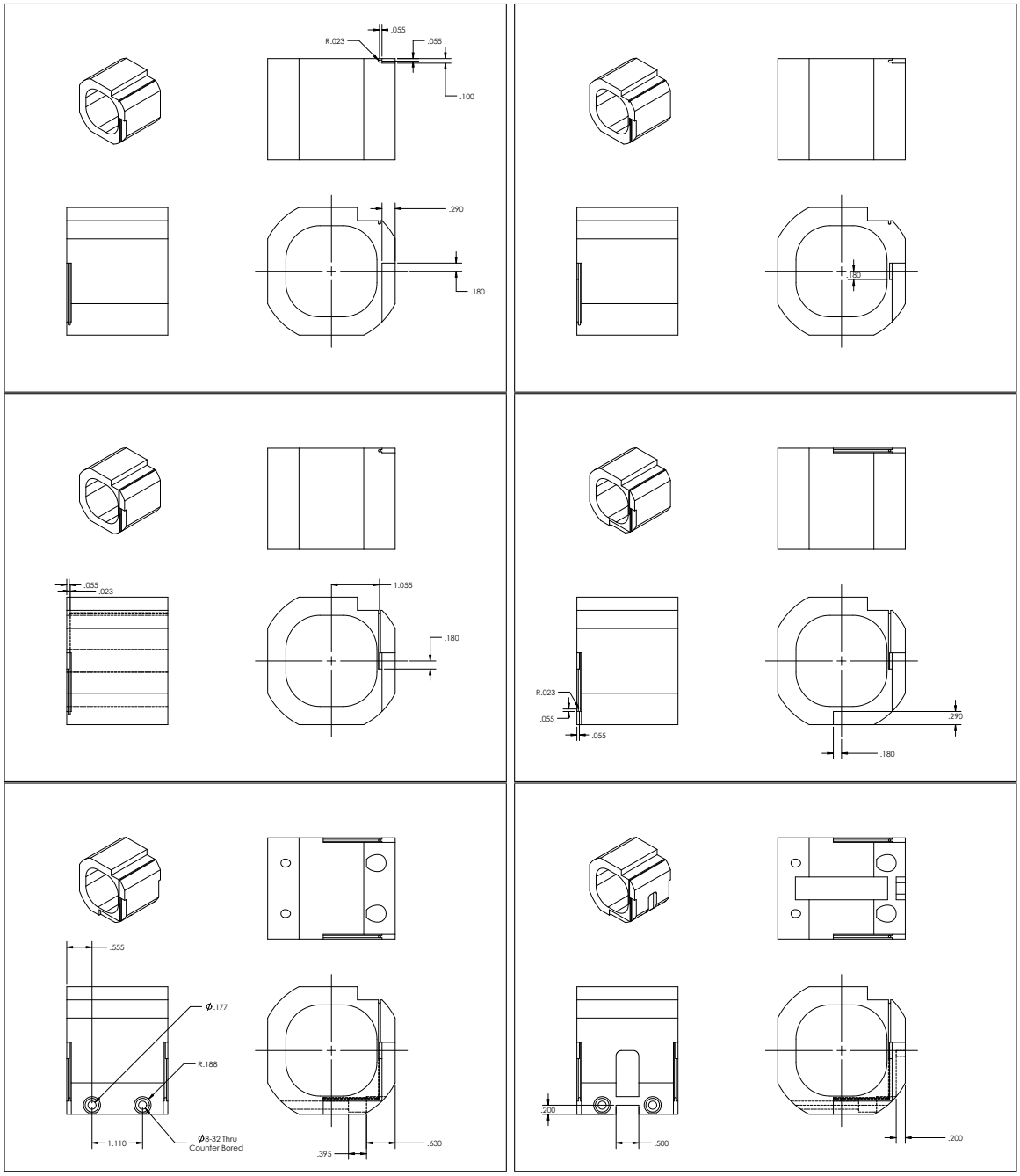
.055
R.023
.055
.100
.290
.180
.180
.055
.023
1.055
.180
R.023
.055
.055
.290
.180
.555
ϕ.177
R.188
1.110
ϕ8-32 Thru
Counter Bored
.395
.630
.200
.500
.200

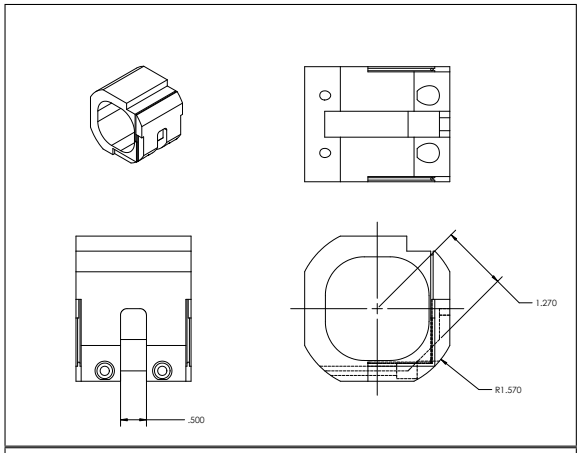
1.270
R1.570
.500

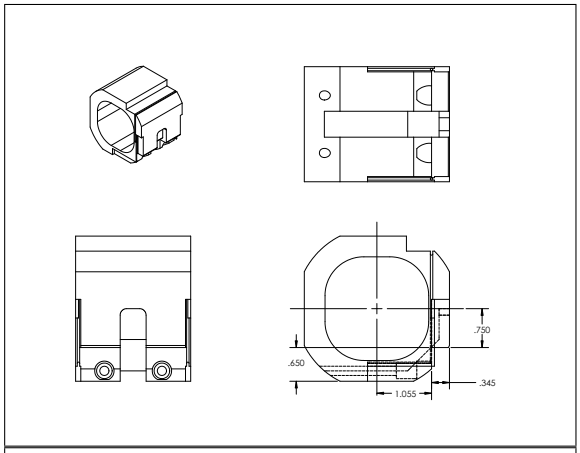
.750
.650
.345
1.055

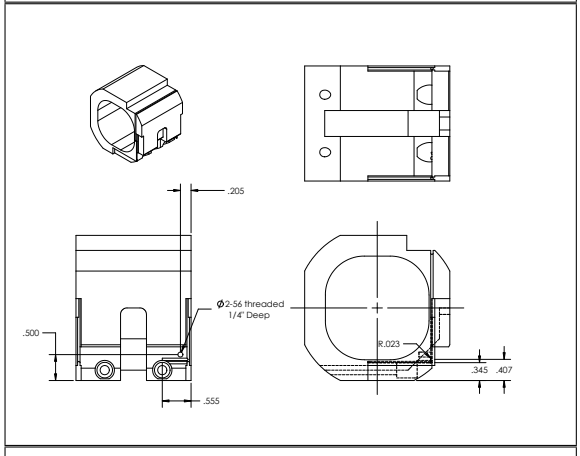
.205
Ø2-56 threaded
1/4" Deep
.500
.555
R.023
.345
.407

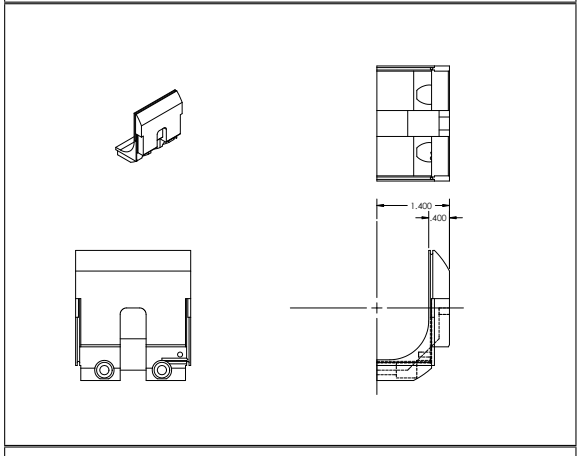
1.400
.400

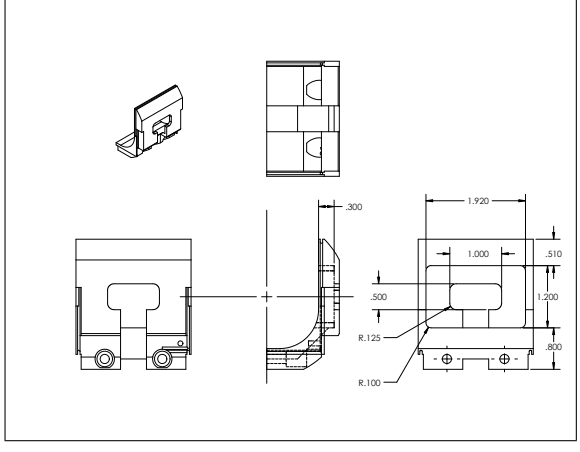
.300
1.920
1.000
.510
1.200
.500
R.125
.800
R.100

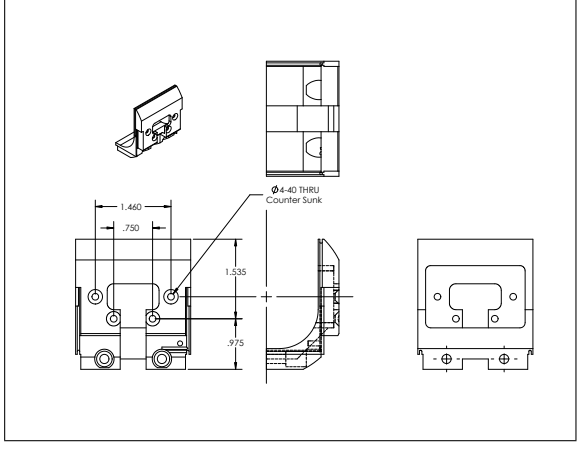
Ø4-40 THRU
Counter Sunk
1.460
.750
1.535
.975

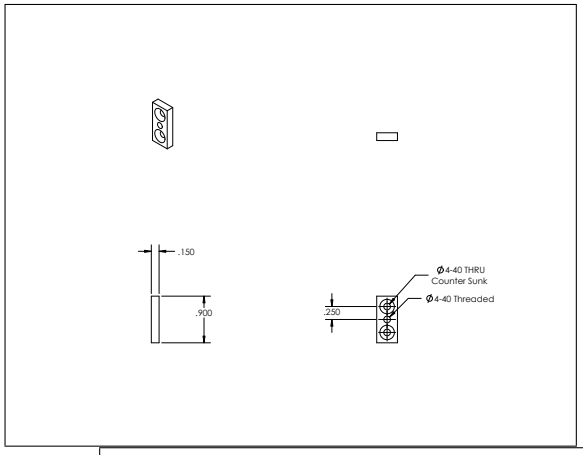
.150
.900
.250
Ø4-40 THRU
Counter Sunk
Ø4-40 Threaded

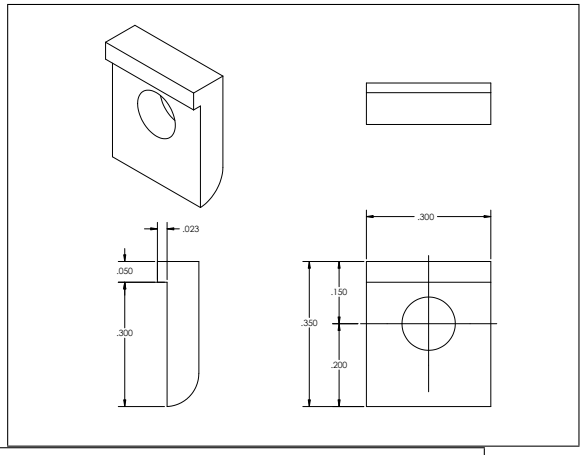
.023
.050
.300
.300
.150
.350
.200

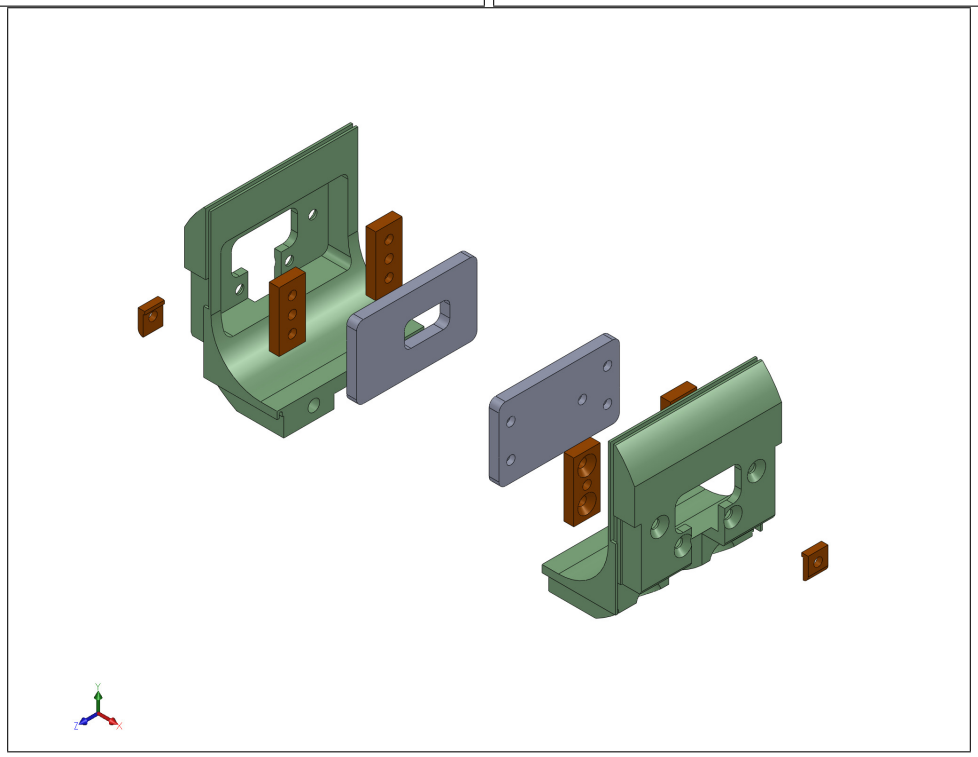

Appendix E – Online Articles

The publication of the electron double-slit diffraction experiment garnered attention from several online and print news agencies. Below are a few screen shots of the stories covering the publication.

Figure E.1. Physics World; `http://physicsworld.com/cws/article/news/2013/mar/14/feynmans-double-slit-experiment-gets-a-makeover`

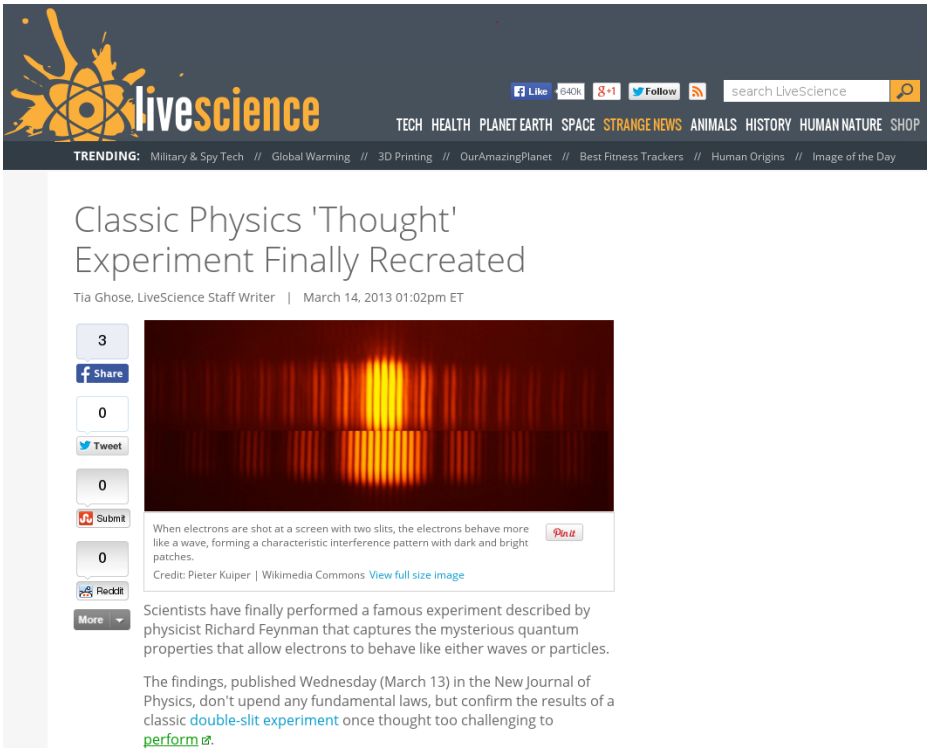

Figure E.2. Live Science; `http://www.livescience.com/27881-feynman-double-slit-experiment-performed.html`

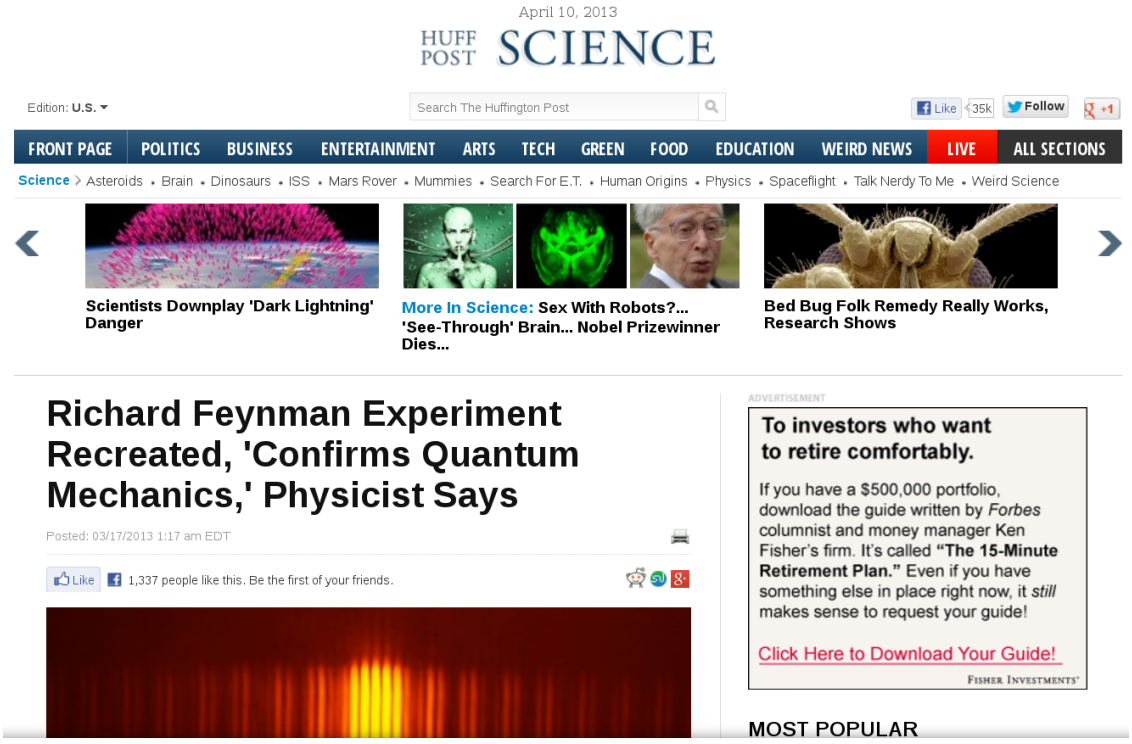

Figure E.3. The Huffington Post; `http://www.huffingtonpost.com/2013/03/17/physicist-richard-feynman-thought-experiment_n_2883913.html`

Figure E.4. R&D.com; `http://www.rdmag.com/news/2013/03/feynmans-double-slit-experiment-brought-life`

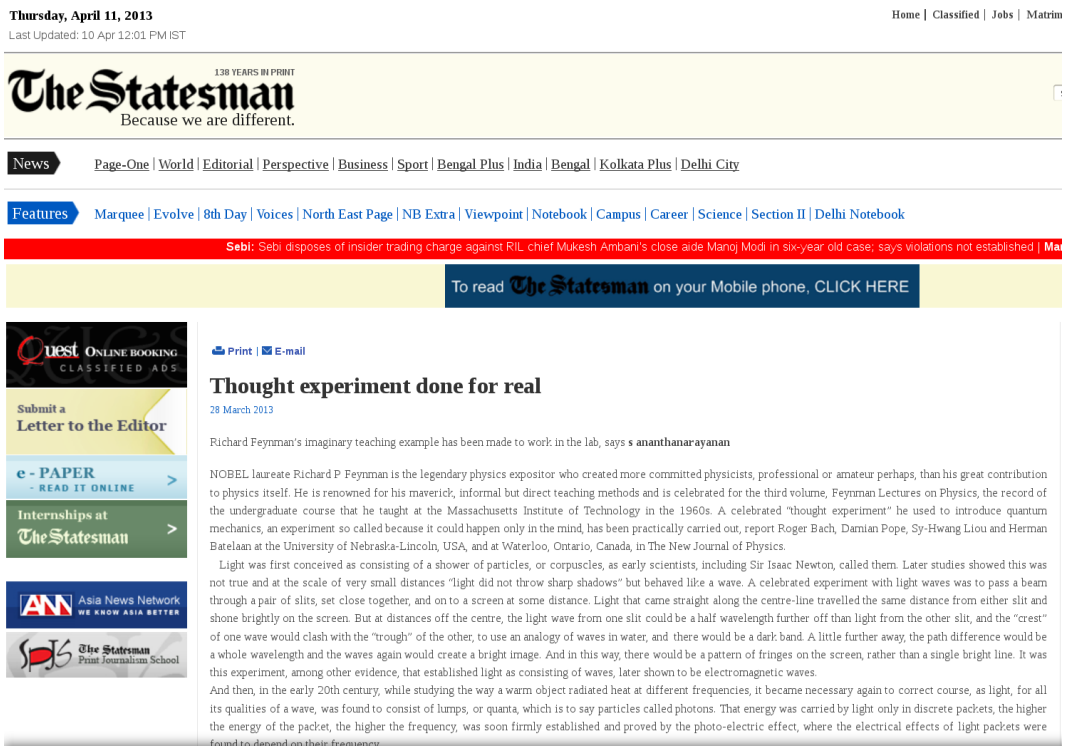

Figure E.5. The Statesman

References

1. Bach, R. A., Pope, D., Liou, S. H., and Batelaan, H. Controlled double-slit electron diffraction. *New J. Phys.* **15**, 033018 (2013).
2. Bach, R., Gronniger, G., and Batelaan, H. An electron Talbot-Lau interferometer and magnetic field sensing. *Appl. Phys. Lett.* **103**, 254102 (2013).
3. Caprez, A., Bach, R., McGregor, S., and Batelaan, H. A wide-angle electron grating biprism beam splitter. *J. Phys. B* **42**, 165503 (2009).
4. McGregor, S., Bach, R., and Batelaan, H. Transverse quantum Stern-Gerlach magnets for electrons. *New J. Phys.* **13**, 065018 (2011).
5. Huang, W. C.-W., Bach, R., Beierle, P., and Batelaan, H. A low-power optical electron switch. *J. Phys. D: Appl. Phys* **47**, 085102 (2014).
6. Bunch, B. H. and Hellemans, A. *The History of Science and Technolgy.* Houghton Mifflin, (2004).
7. Hariharan, P. *Basics of Interferometry.* Elsevier Inc., (2007).
8. The Ligo Scientific Collaboration & The Viro Collaboration. An upper limit on the estochastic gravitational-wave background of cosmological origin. *Nature* **460**, 990–994 (2009).
9. Dimopoulos, S., Graham, P. W., Hogan, J. M., and Kasevich, M. A. Testing gereral relativity with atom interferometry. *Phys. Rev. Lett.* **98**, 111102 (2007).
10. Dimopoulos, S., Graham, P. W., Hogan, J. M., and Kasevich, M. A. Gereral relativistic effects in atom interferometry. *Phys. Rev. D* **78**, 042003 (2008).
11. McFee, J. E. and Das, Y. Locating and identifying compact ferrous objects. *IEEE Trans. Geosci. Remote Sensing* **28**, 182–193 (1990).
12. Kamara, A. Review: Geophysical methods for kimberlite, prospecting. *Explor. Geophys.* **12**(3), 43–51 (1981).

13. Dunmore, S. *Lost Subs.* Chartwell Books, Edison NJ, (2007).

14. Ripka, P. Advances in fluxgate sensors. *Sens. Actuators, A* **106**, 8–14 (2003).

15. Davisson, C. and Germer, L. H. Diffraction of electrons by a crystal of nickel. *Phys. Rev.* **30**, 705 (1927).

16. Estermann, I. and Stern, O. Beugung von Molekularstrahlen. *Z. Phys.* **61**, 95–125 (1930).

17. Marton, L., Simpson, J. A., and Suddeth, J. A. An electron interferometer. *Phys. Rev* **90**, 490–491 (1953).

18. Marton, L., Simpson, J. A., and Suddeth, J. A. Electron beam interferometer. *Rev. Sci. Instrum.* **25**, 1099–1104 (1954).

19. Möllenstedt, G. and Düker, H. Fresnelscher Interferenzversuch mit einem Biprisma Für Elektronenwellen (Fresnel interference experiments with a biprism for electron waves). *Naturwissenshaften* **42**, 41 (1955).

20. Möllenstedt, G. and Düker, H. Beobachtungen und Messungen an Biprisma-Interferenzen mit Elektronenwellen (Observations and measurements on biprism interference with electron waves). *Z. Phys.* **145**, 377–397 (1956).

21. Faget, J. and Fert, C. Diffraction et interférences en optique électronique (Diffraction and interference in electron optics). *Cah. Phys.* **83**, 286–296 (1957).

22. Born, M. and Wolf, E. *Principles of Optics.* Pergamon Press, (1959).

23. Tonomura, A., Osakabe, N., Matsuda, T., Kawasaki, T., Endo, J., Yano, S., and Yamada, H. Evidence for Aharonov-Bohm effect with magnetic field completely shielded from electron wave. *Phys. Rev. Lett.* **56**, 792–795 (1986).

24. Sow, C., Harada, K., Tonomura, A., Crabtree, G., and Grier, D. G. Measuremento of the vortex pair interaction potential in a type-II superconductor. *Phys. Rev. Lett.* **80**, 2693–2696 (1998).

25. Tonomura, A., Matsuda, T., Kawasaki, T., Endo, J., and Osakabe, N.

Sensitivity-enhances electron-holographic interferometry and thickness measurement applications at atomic scale. *Phys. Rev. Lett.* **54**, 60–62 (1985).

26. Möllenstedt, G. and Bayh, W. Kontinuierliche Phasenschiebung von Elecktronenwellen im kraftfeldfreien Raum durch das magnetische Vektorpotential eines Solenoids (Continuous phase shift of electron waves in force-free space by the magnetic ventor potential of a solenoid). *Phys. Blätt.* **18**, 299–305 (1962).
27. Tonomura, A. *Electron Holography.: 2nd edition.* Springer Series in Optical Sciences. Springer, (1999).
28. Keith, D. W., Ekstrom, C. R., Turchette, Q. A., and Pritchard, D. E. An interferometer for atoms. *Phys. Rev. Lett.* **66**, 2693–2696 (1991).
29. Schöllkopf, W. and Toennies, J. P. The nondestructive detection of the helium dimer and trimer. *J. Chem. Phys.* **104**, 1155 (1996).
30. Arndt, M., Nairz, O., Vos-Andreae, J., Keller, C., van der Zouw, G., and Zeilinger, A. Wave-particle duality of C_{60} molecules. *Nature* **401**, 680–682 (1999).
31. Bronniger, G., Barwick, B., Batelaan, H., Savas, T., Pritchard, D., and Cronin, A. Electron diffraction from free-standing, metal-coated transmission gratings. *Appl. Phys. Lett.* **87**, 124104 (1995).
32. McMorran, B., Perreault, J. D., Savas, T., and Cronin, A. Diffraction of 0.5 kev electrons from free-standing transmission gratings. *Ultramicroscopy* **106**, 356–264 (2006).
33. Barwick, B., Gronniger, G., Lu, Y., Liou, S., and Batelaan, H. A measurement of electron-wall interaction using transmission diffraction from nanofabricated gratings. *J. Appl. Phys.* **100**, 074322 (2006).
34. Gronniger, G., Barwick, B., and Batelaan, H. A three grating electron interferometer. *New J. Phys.* **8**, 224 (2006).
35. Feynman, R., Leighton, R. B., and Sands, M. L. *Quantum Mechanics*, vol-

ume 3. Addison Wesley, (1965).

36. Tonomura, A., Endo, J., Matsuda, T., Kawasaki, T., and Ezawa, H. Demonstration of single-electron buildup of an interference pattern. *Am. J. Phys.* **57**(2), 117–120, February (1989).
37. Gasiorowicz, S. *Quantum Physics*. Wiley, 3 edition, (2003).
38. Feynman, R. P. Space-time approach to non-relativistic quantum mechanics. *Rev. Mod. Phys.* **20**, 367–387 (1948).
39. Adams, C. S., Sigel, M., and Mlynek, J. Atom optics. *Phys. Rep.* **240**, 143–210 (1994).
40. Hecht, E. *Optics*. Addison Wesley, 4 edition, (2002).
41. Pedrotti, F. L., Pedrotti, L. S., and Pedrotti, L. M. *Introduction to Optics*. Pearson Prentice Hall, 3 edition, (2007).
42. Hackermüller, L., Hornberger, K., Brezger, B., Zeilinger, A., and Arndt, M. Decoherence in a Talbot-Lau interferometer: the influence of molecular scattering. *Appl. Phys. B* **77**, 781–787 (2003).
43. Hackermüller, L., Hornberger, K., Brezger, B., Zeilinger, A., and Arndt, M. Decoherence of matter waves by thermal emmission of radiation. *Nature* **427**, 711–714 (2004).
44. Sonnentag, P. and Hasselbach, F. Measurement of decoherence of electron waves and visualization of the quantum-classical transition. *Phys. Rev. Lett.* **98**, 200402 (2007).
45. Goldstein, H. *Classical Mechanics*. Addison-Wesley, 3 edition, (2001).
46. Zinn-Justin, J. *Path Integrals in Quantum Mechanics*. Oxford University Press, (2005).
47. Shankar, R. *Principles of quantum mechanics*. Springer Science, (1994).
48. Griffiths, D. J. *Introduction to quantum mechanics*. Person Education, Inc., 2 edition, (2005).

49. Feynman, R. P. *Quantum Mechanics and Path Integrals.* McGraw-Hill Companies, Inc., (1965).

50. Turchette, Q. A. *Numerical Model of a Three Grating Interferometer for Atoms.* PhD thesis, Massachusetts Institute of Technology, (1991).

51. Brezger, B., Hackermüller, L., Uttenthaler, S., Petschinka, J., Arndt, M., and Zeilinger, A. Matter-wave interferometer for large molecules. *Phys. Rev. Lett.* **88**, 100404 (2002).

52. Griffiths, D. J. *Introduction to Electrodynamics.* Addison Wesley, 3 edition, (1999).

53. Grisenti, R. E., Schöllkopf, W., Toennies, J. P., Hegerfeldt, G. C., and Köhler, T. Determination of atom-surface van der Waals potential from transmission-grating diffraction intensities. *Phys. Rev. Lett.* **83**, 1755 (1999).

54. Perreault, J. D. and Cronin, A. D. Using atomic diffraction of Na from material gratings to measure atom-surface interactions. *Phys. Rev. A* **71**, 053612 (2005).

55. Rose, B. A. Measurement of contact potential difference between different faces of copper single crystals. *Phys. Rev.* **44**, 585 (1933).

56. Gradshteyn, I. S. and Ryzhik, I. M. *Table of Integrals, Series, and Products.* Academic Press, 7 edition, (2007).

57. Lord Rayleigh. On copying diffraction-gratings, and on some phenomenon connected therewith. *Philos. Mag.* **11**, 196–205 (1881).

58. Cronin, A. D., Schmiedmayer, J., and Pritchard, D. E. Optics and interferometry with atoms and molecules. *Rev. Mod. Phys.* **81**, 1051–1129 (2009).

59. Freimund, D. F., Aflatooni, K., and Batelaan, H. Observation of the kapitzaa-dirac effect. *Nature* **413**, 142 (2001).

60. Lindeberg, T. *Scale-Space Theory in Computer Vision.* Kluwer Academic Publishers, (1994).

61. Lindeberg, T. Feature detection with automatic scale selection. *IJCV* **30**, 79–116 (1998).

62. Lindeberg, T. Scale-space theory: A basic tool for analysing structures at different scales. *J Appl. Stat.* **21**, 224–270 (1994).

63. Jönsson, C. Elektroneninterferenzen an mehreren künstlich hergestellten Feinspalten. *Z. Phys* **161**(2), 454–474 (1961).

64. Merli, P. G., Missiroli, G. F., and Pozzi, G. On the statistical aspect of electron interference phenomena. *Am. J. Phy.* **44**(3), 306–307, May (1976).

65. Crease, R. P. The double-slit experiment. *Phys. World* **15**, 15 (2002).

66. Crease, R. P. The most beatiful experiment. *Phys. World* **15**, 19–20 (2002).

67. Frabboni, S., Gazzai, G. C., and Pozzi, G. Young's double-slit interference experiment with electrons. *Am. J. Phy.* **75**, 1053–1055, November (2007).

68. Frabboni, S., Gazzai, G. C., and Pozzi, G. Nanofabrication and the realization of Feynman's two-slit experiment. *Appl. Phys. Lett* **93**, 073108 (2008).

69. Frabboni, S., Gabrielli, A., Gazzadi, G. C., Giorgi, F., Matteucci, G., Pozzi, G., Cesari, N. S., Villa, M., and Zoccoli, A. The young-feynman two-slits experiment with single electrons: Build-up of the interference pattern and arrival-time distribution using a fast-readout pixel detector. *Ultramicroscopy* **116**, 73 – 76 (2012).

70. Oberthaler, M. K., Bernet, S., Rasel, E. M., Schmiedmayer, J., and Zeilinger, A. Inertial sensing with classical atomic beams. *Phys. Rev. A* **54**(4), 3165–3176 (1996).

71. Lenef, A., Hammond, T. D., Smith, E. T., Chapman, M. S., Rubenstein, R. A., and Pritchard, D. E. Rotation sensing with an atom interferometer. *Phys. Rev. Lett.* **78**, 760–763 (1997).

72. Colella, R., Overhauser, A. W., and Werner, S. A. Observation of gravitaionally induced quantum interference. *Phys. Rev. Lett.* **34**, 1472 (1975).

73. Fixier, J. B., Foster, F. T., McGuirk, J. M., and Kasevich, M. A. Atom interferometer measurement of the newtonian constant of gravity. *Science* **315**, 74–77 (2007).

74. Gupta, S., Dieckmann, K., Hadzibabic, Z., and Pritchard, D. E. Contrast interferometry using Bose-Einstein condensates to measure h/m and α. *Phys. Rev. Lett.* **89**, 140401 (2002).

75. Rauch, H. and Werner, S. A. *Neutron Interferometry: Lessons in Experimental Quantum Mechanics*. Oxford University Press, Oxford, (2000).

76. Hornberger, K., Gerlich, S., Haslinger, P., Nimmrichter, S., and Arndt, M. Colloquium: Quantum interference of clusters and molecules. *Rev. Mod. Phys.* **84**, 157–173 (2012).

77. Tonomura, A. *The Quantuum World Unveiled by Electron Waves*. World Scientific Publishing Co., Singapore, (1998).

78. Kiesel, H., Renz, A., and Hasselbach, F. Observation of hanbury brown-twiss anticorrelations for free electrons. *Nature* **418**, 392–394 (2002).

79. Möllenstedt, G. and Lichte, H. Electron interferometry. In Neutron Interferometry, Bonse, U. and Rauch, H., editors, 363–388. Clarendon Press, Oxford (1979).

80. Hasselbach, F. and Niklaus, M. Wien filter: A wave-packet shifting device for restoring longitudinal coherence in charged-matter-wave interferometers. *Phys. Rev. A* **48**, 152 (1993).

81. McMorran, B. J. and Cronin, A. An electron Talbot interferometer. *New J. Phys* **11**, 033021 (2009).

82. Cronin, A. D. and McMorran, B. Electron interferometry with nanogratings. *Phys. Rev. A* **74**, 061602 (2006).

83. Savas, T. A., Shah, S. N., Schattenburg, M. L., Carter, J. M., and Smith, H. I. Achromatic interferometric lithography for 100-nm-period grating and grids.

J. Vac. Sci. Technol. B **13**(6), 2732–2736 (1995).

84. Savas, T. A., Schattenburg, M. L., Carter, J. M., and Smith, H. I. Large-area achromatic interferometric lithography for 100 nm period gratings and grids. *J. Vac. Sci. Technol. B* **14**(6), 4167–4170 (1996).
85. Aharonov, Y. and Bohm, D. Significance of electromagnetic potentials in the quantum theory. *Phys. Rev.* **115**, 485–491 (1959).
86. Lens, J. and Edelstein, A. S. Magnetic sensors and their applications. *IEEE Sens. J.* **6**, 631–649 (2006).
87. Clark, J. Squid fundamentals. In SQUID Sensors: Fundamentals, Fabrication and Applicaitons, Weinstock, H., editor. Kluwer Academics, Dordrecht (1996).
88. Griffith, W. C., Jimenez-Martinez, R., Shah, V., Knappe, S., and Kitching, J. Miniature atomic magnetometer integrated with flux concentrators. *Appl. Phys. Lett.* **94**, 023502 (2009).
89. Badurek, G., Weinfurter, H., Gahler, R., Kollmar, A., Wehinger, S., and Zeilinger, A. Nondispersive phase of the Aharonov-Bohm effect. *Phys. Rev. Lett.* **71**, 307–311 (1993).
90. Clauser, J. F. and Li, S. Talbot-vonLau atom interferometry with cold slow potassium. *Phys. Rev.* **49**, R2213–R2216 (1994).
91. Jacques, V., Wu, E., Grosshans, F., Treussart, F., Grangier, P., Aspect, A., and Roch, J.-F. Experimental realization of Wheeler's delayed-choice gedanken experiment. *Science* **315**, 966–968, FEb (2007).
92. Sinha, U., Couteau, C., Jennewein, T., Laflamme, R., and Weihs, G. Ruling out multi-order interference in quantum mechanics. *Science* **329**, 419–421, July (2010).
93. Kocsis, S., Braverman, B., Ravets, S., Stevens, M. J., Mirin, R. P., Shalm, L. K., and Steinberg, A. M. Observing the average trajectories of single photons in a two-slit interferomenter. *Science* **332**, 1170–1173, June (2011).

94. Menzel, R., Puhlmann, D., Heuer, A., and Schleich, W. P. Wave-particle dualism and complementarity unraveled by a different mode. *PNAS* **109**, 9314–9319, June (2012).

95. Everett, H. "Relative State" Formulation of Quantum Mechanics. *Rev. Mod. Phys.* **29**, 454–462, Jul (1957).

96. DeWitt, B. S. The many-universes interpretation of quantum mechanics. In *Proceedings of the International School of Physics "Enrico Fermi" Course IL: Foundations of Quantum Mechanics*, 211–262. Acedemic Press (1972).

97. Bohm, D. A suggested interpretation of the quantum theory in terms of "hidden" variables. I. *Phys. Rev.* **85**, 166–179, Jan (1952).

98. Bohm, D. A suggested interpretation of the quantum theory in terms of "hidden" variables. II. *Phys. Rev.* **85**, 180–193, Jan (1952).

99. Miller, W. A. and Wheeler, J. A. Delayed-choice experiments and Bohr's elementary quantum phenomenon. In *Proceedings of the International Symposium on Foundations of Quantum Mechanics in the Light of New Technology*, 140–152. Physics Society of Japan (1983).

100. Couder, Y. and Fort, E. Single-particle diffraction and interference at a macroscopic scale. *Phys. Rev. Lett.* **97**, 154101, Oct (2006).

101. "How Does the Universe Work". *Through the Wormhole, With Morgan Freeman*. Science Channel, (2011). Television.

102. EmerQuM 11. Emergent Quantum Mechanics 2011. *J. Phys.: Conf. Ser.* **361**(1), 011001 (2012).

103. Nelson, E. Derivation of the Schrödinger equation from newtonian mechanics. *Phys. Rev.* **150**, 1079–1085, Oct (1966).

104. de la Peña, L. and Cetto, A. M. *The Quantum Dice: An Introduction to Stochastic Electrodynamics*. Springer, (1995).

105. Boyer, T. H. Random electrodynamics: the theory of classical electrodynamics

with classical electromagnetic zero-point radiation. *Phys. Rev. D* **11**, 790–808, Feb (1975).

106. Nelson, E. *Quantum Fluctuations*. Princeton University Press, (1985).

107. Hestenes, D. Zitterbewegung in radiative processes. In *The Electron*, 21–36. Kluwer Academic Publishers (1991).

108. Kracklauer, A. F. Pilot wave steerage: A mechanism and test. *Found. Phys. Lett.* **12**, 441–453 (1999).

109. de la Peña, L. and Cetto, A. M. Contribution from stochastic electrodynamics to the understanding of quantum mechanics. *eprint arXiv:quant-ph/0501011* **1** (2005).

110. Cavalleri, G., Barbero, F., Bertazzi, G., Cesaroni, E., Tonni, E., Bosi, L., Spavieri, G., and Gillies, G. A quantitative assessment of stochastic electrodynamics with spin (SEDS): Physical principles and novel applications. *Front. Phys. China* **5**, 107–122 (2010).

111. Grössing, G., Fussy, S., Mesa Pascasio, J., and Schwabl, H. An explanation of interference effects in the double slit experiment: Classical trajectories plus ballistic diffusion caused by zero-point fluctuations. *Ann. Phys* **327**(2), 421 – 437 (2012).